Utrecht University

Master Thesis

Stability and Promoter Effects of Carbon-Supported, Copper-Based Catalysts in Methanol Synthesis

Daily supervisor: C. E. (Lisette) Pompe, MSc
Project supervisor: prof. dr. P. E. (Petra) de Jongh
Second examiner: dr. J. (Jovana) Zečević

Group of Inorganic Chemistry and Catalysis
Debye Institute for Nanomaterials Science
Utrecht University

R. (Remco) Dalebout, BSc

February 15, 2016

Abstract

Nowadays, the chemical industry makes use of the $Cu/ZnO/Al_2O_3$ catalyst to convert CO_2-enriched synthesis gas (CO/H_2) to methanol. Within this Cu catalyst the ZnO promoter is needed to enhance the activity, but simultaneously influences the stability negatively. In this thesis the influence of Zn, Mn, and Cr promoters is investigated on the copper particle size and catalytic performance of carbon-supported, model catalysts. These model catalysts are synthesized via incipient wetness (co)-impregnation (IWI) of metal nitrates on pristine carbon nanotubes (CNTs), oxidized carbon nanotubes (oxCNTs), and high surface area graphite (HSAG). According to titrations the supports differ in Brønsted acidity by the following trend: oxCNT $\gg$ HSAG > CNTs. Upon oxidation of CNTs a smaller, mean Cu particle size is acquired (2.5 nm). Due to the irregular morphology of HSAG-supported catalysts this size increases to 12 nm. Addition of promoters only affect the initial mean Cu particle size of HSAG-supported catalysts: compared to the non-promoted catalyst MnO facilitates Cu particle growth, whereas Cr_2O_3 hampers this process. All promoters enhance the initial activity significantly during catalytic tests of 250 h: ZnO $\gg$ MnO > Cr_2O_3 $\gg$ non-promoted. However, addition of Cr_2O_3 results in the most stable catalyst. For most catalysts the methanol selectivity was $\geq$ 92 % for the entire run. Clustering is observed for the MnO-Cu/oxCNT and Cr_2O_3-Cu/oxCNT catalysts with high-angle, annular, dark-field scanning-transmission electron microscopy by energy-dispersive X-ray detectors (HAADF-STEM-EDX). Fundamentally the most promising catalyst is the Cr_2O_3-promoted, HSAG-supported catalyst, which exhibit an initially small, mean Cu particle size, initially enhanced activity, and high catalyst stability.

List of Abbreviations

The units given in square brackets are based on IUPAC conventions. Throughout this thesis different units are used.

β	peak line broadening or full-width at half-maximum (FWHM) value [rad]
$\Delta_r H^\ominus$	standard enthalpy of reaction [J]
2θ	Bragg angle [°]
λ	wavelength (of X-rays) [nm]
ρ	density [$kg \cdot m^{-3}$]
Φ_{CO_x}	CO or CO_2 flux [$mol \cdot s^{-1}$]
ϕ_V	volumetric flow [$m^3 \cdot s^{-1}$]
χ	conversion [%]
BET surface area	Brunauer-Emmett-Teller surface area [$m^2 \cdot kg^{-1}$]
BJH analysis	Barrett-Joyner-Halenda analysis
c	concentration [$mol \cdot m^{-3}$]
CNT	pristine carbon nanotube
CTY	copper time yield [$mol_{CO+CO_2} \cdot g_{Cu}^{-1} \cdot s^{-1}$]
DME	dimethyl ether
d_{cryst}	crystallite size [nm]
d_i	i-th geometric particle diameter [nm]
d_N	number-averaged particle diameter [nm]
d_S	surface-averaged particle diameter [nm]
d_V	volume-averaged particle diameter [nm]
D_{Cu}	copper dispersion [–]
EXAFS	extended X-ray absorption fine structure
FID	flame ionization detector
FWHM	full-width at half-maximum value or peak line broadening β [rad]
GC	gas chromatography
GHSV	gas hourly space velocity ($= \phi_V / V_{pellet}$) [h^{-1}]
H_2-TPR	temperature-programmed reduction with hydrogen
HAADF-STEM-EDX	high-angle, annular, dark-field scanning-transmission electron microscopy with energy-dispersive X-ray detectors
HSAG	high surface area graphite

ICP-MS	inductively coupled plasma mass spectrometry
IWI	incipient wetness impregnation
$K^{\ominus}$	standard equilibrium constant [–]
K_{sf}	shape factor (in Scherrer equation) [–]
LPO	liquid phase oxidation
m	mass [kg]
M	molar mass [$g \cdot mol^{-1}$]
m/z **ratio**	dimensionless mass-to-charge ratio [–]
MS	mass spectrometry
MTO process	methanol-to-olefins process
N	number of particles [–]
NA	normalized methanol activity [%]
oxCNT	oxidized carbon nanotube
p	pressure [Pa]
p/p_0	relative pressure (in N_2 physisorption) [–]
pK_a	acid dissociation constant [–]
p.a.	pro analysis or analytic purity grade
r	radius [m]
R	gas constant [$J \cdot mol^{-1} \cdot K^{-1}$]
RA	relative methanol activity [%]
RF	response factor [–]
s	sample standard deviation [nm]
S	carbon atom-based product selectivity [%]
STP	standard temperature and pressure conditions of 273.15 K and 1 bar, respectively
t	time [s] or statistical thickness [nm]
T	temperature [K]
TCD	thermal conductivity detector
TEM	transmission electron microscopy
TGA-MS	mass spectrometry-coupled thermogravimetric analysis
TOF	turn over frequency [s^{-1}]
TPO	temperature-programmed oxidation
TSE	tensile strength effect
V	volume [m^3]
wt	weight loading [wt%]
XAS	X-ray absorption spectroscopy
XPS	X-ray photoelectron spectroscopy
XRD	X-ray diffraction
z_{CO+CO_2}	catalyst mass-based activity [$mol_{CO+CO_2} \cdot kg_{cat}^{-1} \cdot h^{-1}$]

Contents

1 Introduction

1.1 General Background

The chemical industry is always on the move and to improve itself it has to increase its economical strength, while taking care of energy-related and environmental issues. The methanol industry, for example, is still reliant on the use of fossil-fuel reserves, which thus have to be used in a most efficient manner. To illustrate, methane is one of the used carbonaceous resources for the production of methanol. From this feedstock large reserves became available in the form of shale gas and is being extracted in, for instance, the U.S.A. ($16 \times 10^{12}\,m^3$ of technically recoverable shale gas in 2013) [1]. Furthermore, methanol is a compound, which is produced in large quantities: the worldwide supply and demand in 2013 was $65 \times 10^9\,g$, which is ever growing [2, 3]. This means that a little improvement in its production process might have a significant impact on the effectiveness. For that reason, there is a money-driven motivation towards the optimization of this process.

Methanol is a chemical building block used for a wide variety of compounds, ranging from primarily acetic acid, formaldehyde, and chloromethane, which could in turn act as building blocks for polyvinyl alcohol, rubber, and chloroform, respectively [4, 5]. In addition, it is directly used as a fuel additive, for fuel cells, and as an intermediate for light olefins in the methanol-to-olefins (MTO) process [6]. Alternatively, a diversity of short-chain hydrocarbons could be synthesized from methanol. Another advantageous property of methanol is its facile transportability, natural occurrence, and biodegradability [7], making it a favored intermediate for the chemical industry [6]. However, methanol has to be treated carefully, as it can affect the central nervous system and vision of humans [8].

Different synthesis routes are applicable towards the production of methanol. Already from the 1920s methanol is produced on an industrial scale from natural gas [9, 10]. From this resource methanol can be produced directly, as shown in equation (1.3), and indirectly via synthesis gas, commonly known as syngas or alternatively watergas (H_2/CO) [11, 12]. As the partial methane oxidation still suffers of selectivity issues [12, 13] the route via syngas conversion (molar ratio of H_2:CO of 2:1) is nowadays commercialized [14]. During the direct methanol synthesis harsh conditions have to used to activate the methane C–H bond and under these conditions the more reactive, produced methanol is prone to full oxidation towards CO and CO_2, as depicted in equation (1.7). At the other hand, selectivities towards methanol via the indirect route of $\geq 99\,\%$ are not uncommon.

In reaction equation (1.1) the energy-intensive steam reforming of methane, the main component of natural gas, is displayed. Via this route syngas is obtained as an intermediate, although the exothermic, partial oxidation, as depicted in reaction equation (1.2), is also frequently encountered in industry [11, 12]. Methanol can also be produced from carbon dioxide, following equations (1.5). The introduction of 25 vol% of the CO_2 in the syngas feed enhances the activity towards methanol. The motivation for this CO_2 introduction is further

explained in section 1.2. To summarize, the most important reactions present during the indirect methanol production from methane are as follows [11, 12, 14, 15]:

$$CH_4 + H_2O \rightleftharpoons CO + 3H_2 \quad (\Delta_r H^\ominus = 206\,\text{kJ/mol}, \quad H_2/CO = 3) \tag{1.1}$$

$$CH_4 + 0.5O_2 \rightleftharpoons CO + 2H_2 \quad (\Delta_r H^\ominus = -35\,\text{kJ/mol}, \quad H_2/CO = 2) \tag{1.2}$$

$$CH_4 + 0.5O_2 \rightleftharpoons CH_3OH \quad (\Delta_r H^\ominus = -126\,\text{kJ/mol}, \quad K^\ominus = 4.1 \cdot 10^{21}) \tag{1.3}$$

$$CO + 2H_2 \rightleftharpoons CH_3OH \quad (\Delta_r H^\ominus = -89\,\text{kJ/mol}, \quad K^\ominus = 7.0 \cdot 10^{5}) \tag{1.4}$$

$$CO_2 + 3H_2 \rightleftharpoons CH_3OH + H_2O \quad (\Delta_r H^\ominus = -48\,\text{kJ/mol}, \quad K^\ominus = 1.5) \tag{1.5}$$

$$CO_2 + H_2 \rightleftharpoons CO + H_2O \quad (\Delta_r H^\ominus = 41\,\text{kJ/mol}, \quad K^\ominus = 2.1 \cdot 10^{-6}) \tag{1.6}$$

$$CH_4 + 2O_2 \rightleftharpoons CO_2 + 2H_2O \quad (\Delta_r H^\ominus = -803\,\text{kJ/mol}, \quad K^\ominus = 1.6 \cdot 10^{153}) \tag{1.7}$$

in which $\Delta_r H^\ominus$ and $K^\ominus$ represent the standard enthalpy of reaction and equilibrium constant, respectively.

Reaction equations (1.4) and (1.5) describe the complete, exothermic reactions towards methanol from a CO_2-depleted and CO_2-enriched syngas feed, respectively. Furthermore, the reverse watergas-shift reaction, displayed in equation (1.6), establishes an interconversion between the CO_2-enriched syngas and H_2O formed during methanol synthesis. As less molecules are produced than consumed, regarding to equations (1.4) and (1.5), the entropy is lowered and hence a maximum syngas conversion could be achieved at high pressures. Despite the reactions are exothermal, also under working conditions, an elevated temperature is needed to enhance the kinetics of the reaction, or equivalently the methanol production rate. Indeed, in industry a temperature of approximately 260 °C and a syngas pressure of 100 bar are used [14]. The effects of pressure and temperature on the equilibrium product distributions with a 25:8:67 mol% $CO:CO_2:H_2$ feedstock were calculated using HSC Chemistry v7.14 and are plotted in figure 1.1. Figure 1.1b shows indeed that at a constant pressure of 100 bar a lower temperature would result in a higher thermodynamic methanol production.

However, for laboratory use it is challenging to achieve such high pressures. Therefore, a pressure around 40 bar is more feasible. From figure 1.1a and c it could noticed that the equilibrium production of methanol at 260 °C and 40 bar is approximately 13.6 mol%, whereas this equilibrium shifts towards approximately 30.9 mol% at the industrial 100 bar, depicted in figure 1.1b. In addition, the thermodynamical, combined CO + CO_2 conversion at 260 °C are 32.1 % and 57.3 % at 40 bar and 100 bar, respectively. These numbers were calculated from the following equation: $\chi_{260\,°C}$ = mol% MeOH / 30 mol% · 100 %.

The heterogeneous catalyst used in industry for the methanol production is the $Cu/ZnO/Al_2O_3$ catalyst in the molar ratio of 55:30:15 [10, 16]. In industry and laboratories, this catalyst is prepared by an accessible coprecipitation method [16–18]. For that reason, an aqueous solution of copper, zinc, and aluminum nitrate in their corresponding molar ratio and one aqueous solution of sodium carbonate are added simultaneously in a dropwise manner to demineralized water at approximately 80 °C under vigorous stirring. The addition of sodium carbonate controls the pH value around 7 to obtain a high catalytic performance [19]. Finally, after aging of approximately 2 h the catalyst is filtrated, dried, and calcined prior to use.

However, there is much debate about the exact roles of each component of the $Cu/ZnO/Al_2O_3$ catalyst, but most agree with the fact that the metallic copper is the most active component of syngas conversion to methanol [10, 19]. Zinc oxide is mainly added for two reasons: 1) it acts as a promoter for metallic copper [20] and 2) it is believed to be the most preferred support [10]. How these two fundamentally different roles of zinc oxide within the catalyst exactly perform with respect to each other is still not fully understood. For example, zinc oxide only is also to some extent active towards methanol production [10]. Furthermore, it is

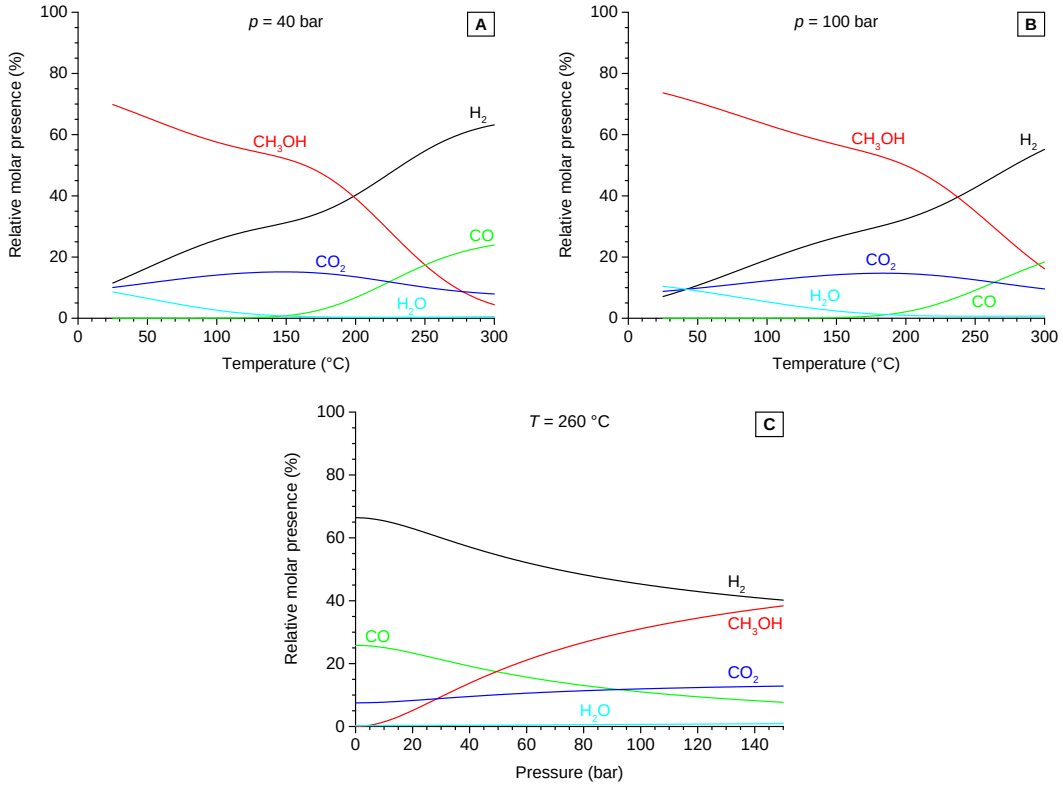

Figure 1.1 Calculated, thermodynamic product distributions over various pressure and temperature ranges with $CO:CO_2:H_2$ = 25:8:67 mol% as feedstock. **a** Constant pressure at 40 bar; **b** constant pressure at 100 bar; **c** constant temperature at 260 °C. In general, at lower temperatures and higher pressures a higher thermodynamic equilibrium towards methanol is obtained. At 260 °C and 40 bar the equilibrium methanol production and CO + CO_2 conversion are 13.6 % and 32.1 %, respectively, whereas at 100 bar these numbers are 30.9 % and 57.3 %, respectively. Calculated with HSC Chemistry v7.14 software [15].

believed that the addition of zinc oxide increases the copper dispersion, and thereby would increase the active copper surface area. In addition, the dissolution of small amounts of Cu^{2+} species in the zinc oxide particles would further enhance the copper dispersion [19]. These promoter effects of zinc oxide are only apparent under reducing conditions, such as in a H_2 and CO-rich feedstream. However, in the presence of large quantities of water this effect is lost [20]. Despite the formation of H_2O during the methanol synthesis, the amount present is negligible under industrially relevant conditions, which could be derived from figure 1.1. Indeed, only a minor amount of CO_2 is added in the feedstream.

The effects of the Al_2O_3 addition are also under debate: at one hand it is added to enhance the thermal stability and poisoning resistance of the catalyst [10], as other authors ascribe the stability enhancement to its separation properties towards the copper and zinc oxide species, thereby diminishing their particle growth [21, 22]. This higher stability was in general induced by the addition of M^{3+} ions, which increased the roughness of the catalyst.

1.2 Reaction Mechanism of Methanol Synthesis

To understand the reason why CO_2 is added in the syngas feed stream, the mechanism of methanol production from syngas over a copper surface has to be understood. This has already been investigated intensively on metal surfaces by, among other authors, Waugh [23] and Bowker *et al.* [24] in the late 80s and early 90s, although there is still a lot of debate going

on. Briefly, they have reported that there is no considerable synergy between the copper nanoparticles and a metal oxide support, due to the fact that the specific copper activity is independent of the nature of the oxide support. Furthermore, it is stated that a high metallic copper surface area is key for a high methanol synthesis activity per mass of catalyst. Alternatively, small metallic copper nanoparticles are needed for a high methanol production. In general, a large amount of a specific, crystallographic surface leads to a higher catalytic activity per mass of active phase. These relationships will also be assumed to be valid for copper nanoparticles supported by carbon.

Waugh [23] and Bowker *et al.* [24] described two different reaction mechanisms in their papers: one with CO_2 present in the reactant feed and one without this addition. In figure 1.2 a schematic representation for these mechanism routes are presented as route a (with CO_2) and route b (without CO_2). In the following paragraphs both mechanism will be explained.

During the conversion of CO_2-enriched syngas towards methanol (route a), CO_2 and H_2 firstly adsorb dissociatively on a copper surface to form individual carbon, oxygen, and hydrogen atoms. Some of these oxygen adatoms may incorporate into the copper surface, although this is still under debate. Secondly, stoichiometrically one oxygen atom is extracted or desorbed, depending if the oxygen atom is an adatom or is incorporated into the copper lattice, by CO to form gaseous CO_2. This *in situ* generation of CO_2 keeps the copper surface only partially oxidized. Under the specific reaction conditions the oxygen atom removal is better performed by CO than by H_2, which would lead to the production of H_2O. Therefore, the actual reactant in the CO_2-enriched feed is CO_2 itself, although normally more CO is initially present in the reactant mixture. At third, another CO_2 molecule binds to the partially

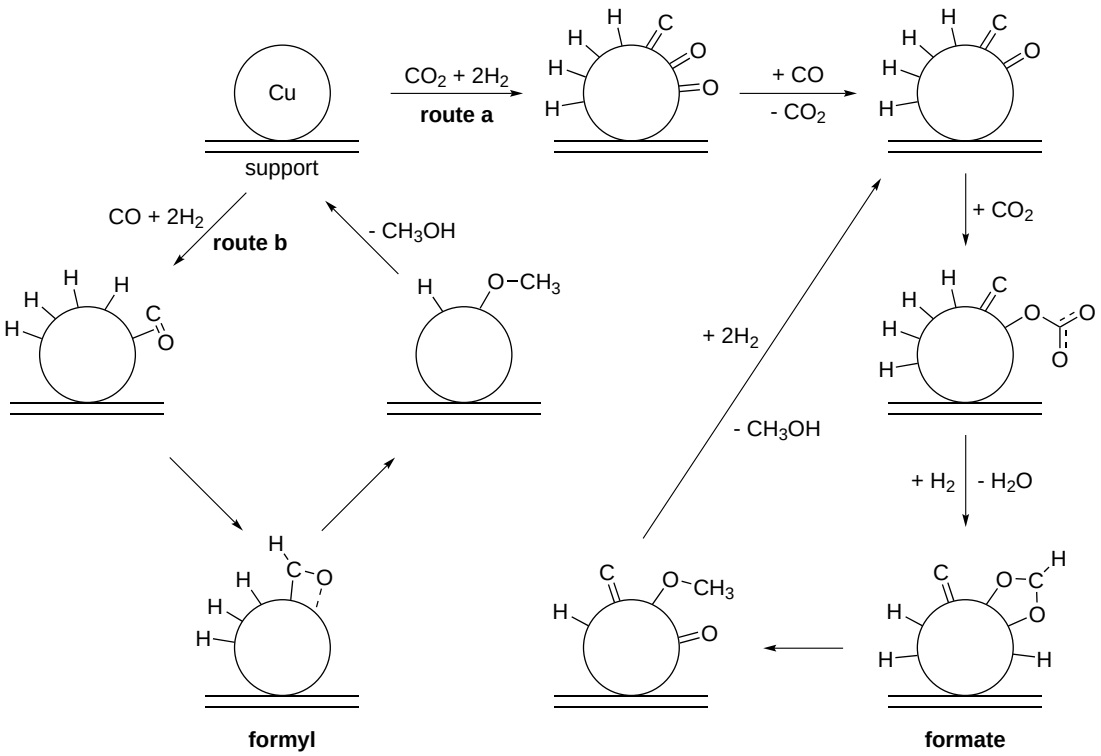

Figure 1.2 Schematic representation of a possible mechanism of the methanol synthesis via **a** a CO_2-enriched syngas feed and **b** a CO_2-depleted syngas feed. Via route **a** bidentately bound formate species are formed, whereas via route **b** monodentately bound formyl species are the most common intermediate. Drawn from mechanism description in [23, 24].

oxidized copper surface or oxidic support in an associateve manner, or equivalently, as a symmetric carbonate. This species is then hydrogenated by the hydrogen adatoms on the copper surface to form a bidentately bound formate ($HC(OR)_2$). Finally, this formate is further hydrogenated via an adsorbed methoxy group (CH_3O–R) to methanol (CH_3OH), which is readily desorbed from the surface [23, 24].

In the reaction mechanism for the CO_2-enriched syngas feed (route a) the hydrogenation of formate is the rate-determining step of the methanol synthesis, which means that the formate species is the longest-living intermediate in the methanol synthesis. This also prevents excessive, dissociative adsorption of CO_2 onto the copper surface (overoxidation), keeping the metallic copper in its most reduced state. It is believed that this is the most active state for copper to perform the methanol synthesis, although at this point a debate is still going on.

The second mechanistic route in figure 1.2 (route b) prevails if no CO_2 is present in the reaction feed. The main difference is that CO adsorbs associatively onto the copper surface, compared to the dissociative adsorption behavior of CO_2. The direct result of this is that no formate is formed, but most likely an adsorbed formyl species instead. This monodentately bound formyl intermediate is less strongly adsorbed than its bidentately bound formate counterpart. As a result, the surface coverage of the most important intermediate during the methanol synthesis is lower. Therefore, this could eventually lead to a lower methanol production activity in the order of 10^2 [23, 24].

The addition of zinc oxide in the industrial catalyst increases the methanol production considerably, but surprisingly also changes the reaction mechanism. Studt *et al.* [25] have shown that stepped and ZnO_x-decorated copper surfaces possess the highest turn over frequencies (TOFs) in a CO_2-rich syngas feed towards methanol production. The addition of zinc oxide in the methanol catalyst in the presence of CO_2-enriched syngas feed stream increases the formate coverage on the copper nanoparticles, but more significantly increases the binding of oxygen-bound intermediates and hence accelerates CO_2 hydrogenation. However, when no CO_2 is added in the feed stream, zinc oxide did not have its promoting effect anymore. It even becomes a poison, as it decreases the binding of carbon-bound intermediate, thereby blocking CO hydrogenation sites [25]. To conclude, Studt *et al.* showed that in the absence of CO_2 the copper nanoparticles are most active without the addition of zinc oxide. Figure 1.3 further summarizes these findings.

During the conversion of CO_2-enriched syngas to methanol, water is formed as a byproduct. This is due to 1) the reduction of oxygen atoms, which are coming from the dissociatively adsorbed CO_2, by hydrogen and due to 2) the reverse watergas-shift reaction (1.6). The first phenomenon occurs at relatively low temperatures, whereas the second one occurs mainly at higher temperatures. Figure 1.4 displays a proposed mechanism for this endothermic reaction on an oxidic support. The first step is the hydrogenation of the metallic copper to form a copper hydride. Next, a CO_2 molecule binds to the partially oxidized support surface near an anion vacancy, which acts as an active site, and is stabilized by the copper hydride. Subsequent hydrogenation of the bound CO_2 molecule activates it to release a CO molecule. The anion vacancy is regenerated by the desorption of water [11].

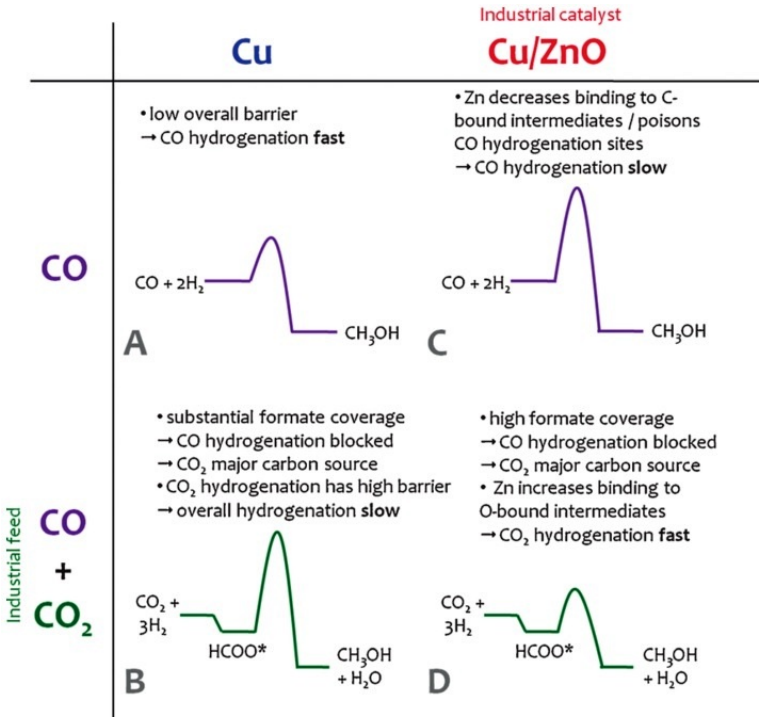

Figure 1.3 Schematic representation of the kinetics of the methanol synthesis for (**a**, **b**) non-promoted and (**c**, **d**) ZnO-promoted copper catalysts under a (**a**, **c**) CO_2-poor and (**b**, **d**) CO_2-rich syngas feed. Case **d** refers to industrial conditions. The most active catalysts for the methanol synthesis comprise cases **a** and **d**. Adapted from [25].

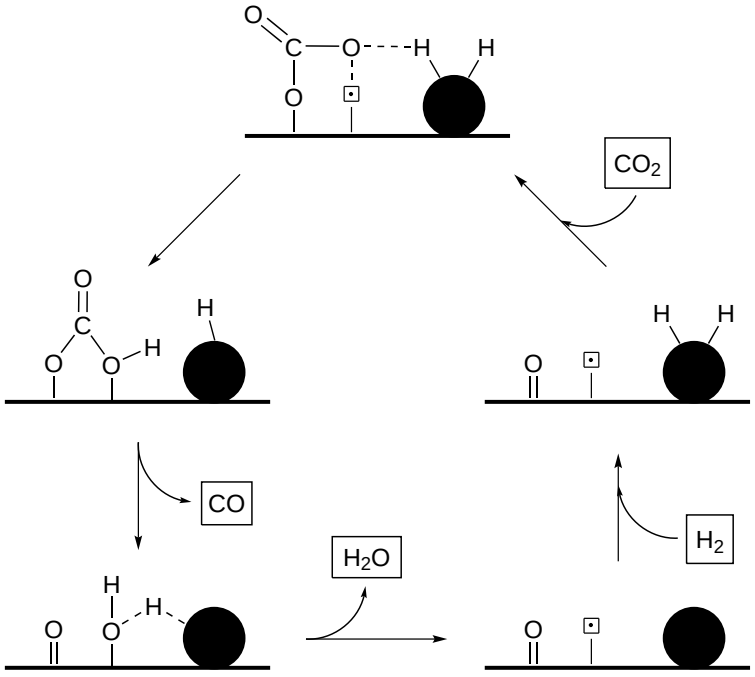

Figure 1.4 Schematic representation of the mechanism of the reverse watergas-shift reaction. The filled, black circles represent copper nanoparticles, the bold line the support, and the dotted, empty square an empty active site. The total reaction equation is depicted in equation (1.6). Redrawn from [11].

1.3 Catalyst Deactivation

During all (industrial) catalytic reactions the catalytic activity and/or selectivity decay over time. Due to this catalyst deactivation the catalyst inside the reactors must be replaced and sometimes factories must even be temporarily shut down. This is a costly process for the industry and therefore research towards stable catalysts at the chemical level but also at the macroscale in the form of pellets of the active catalysts, is highly influenced by this catalyst deactivation [26].

Catalyst deactivation can occur in different ways: for example, by particle growth of the active phase (or equivalently, by the decrease of active metal surface area), metal leaching, loss of promoter effect (if promoters are present), carbon deposition (coke formation), poisoning, chemical support degradation, and physical damage of the catalyst pellets [27]. Coke consists of polymerized, heavy hydrocarbons, obtained by decomposition and condensation of hydrocarbons or CO on catalyst surfaces [28]. Moreover, poisoning concerns the presence of undesirable metals or other molecules. For example, the presence of iron in a copper-based catalyst aimed for the methanol synthesis might induce olefin production.

In the case of copper-based catalysts coke formation is an uncommon deactivation mode, as copper only is insufficient to catalyze the formation of C-C bonds [27]. It is also for this reason that the selectivity towards methanol is considerably high: selectivities $\geq 99\%$ are not uncommon [14].

Although carbon-based catalysts cannot be poisoned by sulfur [29], copper-based catalysts are very sensitive to very low levels of sulfur poisoning [4, 27, 30, 31]. To illustrate, a decline of 20% of methanol activity is observed for a sulfur impurity of only 0.2% [4, 27]. Furthermore, chlorine could act as a poison for these catalysts [27, 31]. Despite the poisoning effect, the presence of zinc oxide as a promoter in a typical methanol catalyst enhances to the tolerance towards sulfur to some extent: a similar decline of methanol activity is observed in the presence of 2% of sulfur in the reaction feed. The reason for this tolerance increase is the fact that zinc oxide can effectively remove hydrogen sulfide, forming the thermodynamically stable zinc sulfide under industrial reaction conditions. In addition, sulfur-related contaminants are normally removed from the syngas feeds before methanol synthesis, especially for laboratory use. Therefore, poisoning by sulfur and chlorine are not the main deactivation modes for methanol catalysts. As mentioned before, coke deposition is also not the main reason for a lowering in the catalytic performance.

For this reason, particle growth and the loss of promoter effect are the most pronounced deactivation modes for methanol catalysts. Particle growth can occur via two different mechanisms [26]: 1) Ostwald ripening, which is the diffusion of atoms or small clusters from one nanoparticle to another, and 2) sintering, which is particle diffusion and subsequent coalescence. These two deactivation modes are displayed in figure 1.5. Ostwald ripening is induced by the difference in nanoparticle sizes, or equivalently the polydispersity of the catalytic system or the differences in the individual surface-to-volume ratios of the nanoparticles. As a result, during Ostwald ripening the rate of atom or small cluster diffusion is relatively larger for the smaller nanoparticles compared to the larger ones, noticing that the average diffusion speed per surface area of same-like sized clusters is similar. This results in a particle growth of the larger nanoparticles at the expense of the smaller ones. Therefore, during this mode of particle growth the polydispersity temporarily increases over time, but ultimately decreases due to the disappearance of the smallest nanoparticles. Furthermore, the sintering rate depends on the initial nanoparticle sizes, as smaller nanoparticles are able to diffuse easier over the support compared to the large ones. However, for this deactivation mode it is expected that none of the nanoparticles shrink during catalysis.

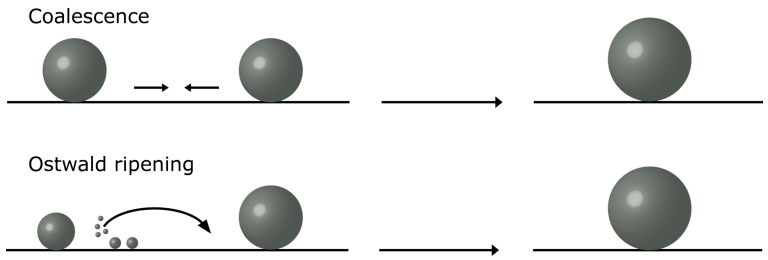

Figure 1.5 Schematic representation of the two modes of particle growth: sintering (alternatively coalescence) and Ostwald ripening. During sintering the nanoparticles itself diffuse over the support surface and coalesce to larger nanoparticles, whereas during Ostwald ripening metal ions or clusters from the smaller nanoparticles diffuse and coalesce towards the larger ones.

Both particle growth processes could occur simultaneously and with a different rate. Furthermore, even as only one particle growth mode would play a role during particle growth the microenvironment of the individual nanoparticles, such as for tube-like supports the particles inside or outside the tubes, could induce different rates of particle growth. Therefore, the assignment of the prevailing particle growth mode during catalyst deactivation could be quite challenging [26].

Fundamentally, nanoparticles grow due to the fact that larger nanoparticles have a lower surface/volume ratio compared to smaller ones, which correspond to a lower Gibbs free energy. Alternatively, the chemical potential decreases upon particle growth, caused by the fact that the radius of curvature for larger particles is smaller [26].

The rate of particle growth depends on various parameters [28]. In the first place, the particle growth of the active phase is accelerated exponentially with temperature. The rational reason for this is that at higher temperatures enough kinetic energy has been build up to overcome the activation energy for particle growth processes, which is in the range of 30 to 150 kJ/mol [28]. These activation energies could differ substantially, and therefore also the particle growth rates, as the chemical nature and/or morphology of the support alters the interaction of the nanoparticles with the support and the ease of nanoparticle diffusion. The rate could also be influenced by a high metal loading: the relatively high-energy atoms or clusters in the case of Ostwald ripening and the small nanoparticles in the case of sintering do not have to diffuse a large distance over the support surface to coalesce with a metal nanoparticle. This effect of interparticle distance could also be influenced by other factors than metal loading, as described by Prieto *et al.* [16].

Finally, the stability of the support might have a substantial effect on the catalyst deactivation. However, various forms of for example carbon generally have a high thermal [32] and hydrothermal stability [33]. Therefore, the generation of water vapor during the reverse watergas-shift reaction, as depicted in equation (1.6), would not have a significant impact on the deactivation or degradation of the support. Moreover, the thermodynamically amount of water produced is considerably low under industrially relevant conditions, as depicted in figure 1.1.

1.4 Project Aims

The main disadvantage of the methanol catalyst used in industry, $Cu/ZnO/Al_2O_3$, is the rapid deactivation by copper particle growth, or alternatively, a catalytic surface area decline. Many studies are focused on the enhancement of the thermal stability of the methanol catalyst [9, 16, 20, 34]. However, little is known about the effect of 1) initial copper particle size monodispersity and 2) the addition of manganese and chromium promoters on the catalyst stability and methanol activity and selectivity. Explicitly, to investigate the monodispersity effect the research aims are as follows:

1. Is it possible to obtain an active methanol synthesis catalyst by depositing sterically stabilized copper colloids onto carbon nanotubes and subsequent removal of surfactants?
2. What are the effects on the catalytic performance of differently-sized, monodisperse copper colloids, deposited onto carbon nanotubes for the methanol synthesis?
3. How are the catalyst stability and methanol production activity affected by carbon nanotube-supported, colloidal copper nanoparticles compared to conventional methanol synthesis catalysts?
4. What is the influence of the individual copper nanoparticle spacing (the 2D copper surface loadings) on the stability of carbon nanotube-supported, colloidal copper-based catalysts?

The project aims for the promoter effect-based part are as following:

1. What are the effects of acidity and support morphology of carbon-based supports on the copper nanoparticle size after catalyst synthesis?
2. How does the addition of zinc, manganese, and chromium promoters affect the copper nanoparticle size?
3. How is the catalytic activity, methanol selectivity, and stability of carbon-supported, copper catalysts influenced by the addition of zinc, manganese, and chromium as promoters?

In this thesis the focus has been laid on the promoter effect-based research goals. From these aims it follows that zinc, manganese, and chromium are investigated as methanol catalyst promoters. Furthermore, three types of carbon supports were used: pristine carbon nanotubes (CNTs), oxidized carbon nanotubes (oxCNTs), and high surface area graphite (HSAG).

1.4.1 Colloidal Approach on Carbon Nanotube-Supported Methanol Catalysts

The advantage of using colloids over other preparation methods is the capability of achieving a narrow particle size distribution, which might limit Ostwald ripening, as described in section 1.3. In contrast, catalysts synthesized via impregnation may have relatively large nanoparticle size distributions. Copper-based colloids can be synthesized in various ways. One method is to use charge-stabilized colloids [35, 36]. However, these particles might be less suitable to immobilize onto a support since aggregation of these colloids can be a problem. Another way is to stabilize colloids by steric stabilization. For example, Yin *et al.* [37] have developed a procedure to obtain Cu_2O colloids with oleic acid ligands on the surfaces in a highly uniform and monodisperse way, which would be appreciable for this research. These colloids could be deposited on carbon nanotubes via a procedure described by Casavola *et al.* [38].

To investigate this initial copper nanoparticle monodispersity effect on the methanol catalyst stability CNTs were chosen as the preferred support for several reasons. At first, it is hydrophobic and hence compatible with ligand-stabilized colloids. Furthermore, the point of zero charge (PZC) of the support could be easily tuned by surface modification [39] to 1) adjust the adsorption strength of these colloids and 2) the ease of nanoparticle diffusion over the support surface, which ultimately leads to growth by coalescence. In addition, copper species do not form stable metal carbides, whereas metal species supported on silica and alumina supports give rise to silicates and aluminates, respectively. Hence, it separates the copper particle growth from support effects: it allows an investigation towards the intrinsic activity of copper. Finally, CNTs have a high enough thermal stability under industrial methanol synthesis conditions, a large specific surface area, and a low mass density [32].

1.4.2 Promoter Effects of Carbon-Supported Methanol Catalysts

Addition of promoters to existing catalysts can alter one or more of the three main performance features of a catalyst either positively or negatively: its stability under reaction conditions, the activity of reactant conversion, and the selectivity towards the desired product(s). The goal of these promoter additions is to enhance one or more of these characteristics without considerable diminishing other advantageous effects. Moreover, the effects of specific promoters on the catalytic performance have to be investigated to design further improved catalysts.

In literature copper-based catalysts for the methanol synthesis are promoted by various promoters and are supported on different supports, which all lead to different promoting effects. The most important promoter for these catalysts is zinc oxide, whose effects are already described in section 1.2. Additionally, chromium and manganese promoters were investigated, although a debate is still going on about their precise effects. Some results are described in the following paragraphs.

Brands *et al.* [40] reported that zinc and manganese are promising promoters for methanol catalysts, as they both have a moderate metal-oxygen bond strength. This parameter is important as one of the steps in the methanol reaction mechanism involves the formation of bidentately bound formate, the longest-living intermediate, as described in section 1.2. As the corresponding bond strength is either too high or too low a decrease in methanol production could be expected. Kilo *et al.* [41] have observed that promotion by chromium oxide (and also to some extent by manganese oxide) to a copper-based, zirconia-supported catalyst diminished the particle growth of the copper particles and hence increased the thermal stability of the catalyst. For these zirconia-supported copper catalysts with additional zinc oxide Lachowska and Skrzypek [42] and Słoczyński *et al.* [43] found that manganese oxide promotion increased the activity due to a higher copper dispersion in the corresponding reduced catalyst, although no effect on the stability was reported.

According to Ma *et al.* [44], addition of chromium oxide to a copper-based catalyst could partially diminish the rearrangement of copper particles in the support structure. Furthermore, they reported that if chromium oxide is part of the support structure the bulk activity and methanol selectivity is enhanced. In addition, Cr-promotion lowers the reduction temperature of copper oxide species [44]. Fujitani *et al.* reported that Cr-addition improves the activity for copper- and zinc-containing catalysts [45], whereas Yurieva *et al.* state that this promotion also enhanced the thermal stability [46].

From this acquisition it becomes clear that the interactions between the promoters, copper species, and the support are complex. As already described in section 1.4.1 the copper nanoparticles barely have any interaction with carbon-based supports. To diminish the metal-support interactions intrinsic promoter effects could be distinguished. Therefore, in this thesis the promoter effects of zinc, chromium, and manganese as promoters on the catalyst stability and methanol activity and stability are investigated using carbon-based supports.

1.5 Project Approach

As described in section 1.4 the focus of this thesis is upon the promoter effect-based research objectives. According to Van der Wal's bachelor's thesis [47] the stability of several carbon-supported, copper catalysts for the methanol synthesis prepared by incipient wetness impregnation are reported. Based on this report three different support types are used: pristine carbon nanotubes (CNTs), oxidized carbon nanotubes (oxCNTs), and high surface area graphite (HSAG). The catalyst synthesis used in this thesis is adapted from this reference. In the following section the incipient wetness impregnation procedure with its subsequent operations are described.

1.5.1 Catalyst Preparation

Academically one of the most favored methods to prepare supported catalysts is via a general method called impregnation [48, 49]. The reasons for this are the facts that 1) the technique is practically easy to perform, 2) there is no need for advanced instrumentation, 3) the synthesis is rather rapid, and 4) it is inexpensive due to the use of, mostly, aqueous solutions and due to the high deposition ratio of the precursor molecules onto the support. Additionally, impregnation is a widely used technique in the chemical industry due to the low amount of waste produced.

The impregnation methods can be broadly divided into two different versions: incipient wetness impregnation (IWI) and wet impregnation. As the first preparation method is the more utilized technique compared to the second one, only IWI will be shortly discussed. During this IWI a pre-dried, porous solid is subjected to a metal precursor solution, mostly consisting of metal nitrates, with a volume equal to the total pore volume of the support. The pH value of this aqueous salt solution is adjusted on basis of the PZC of the support material. Next, the solution penetrates the pores of the support by capillary suction. After the IWI the support still appears to be a dry solid. It is mostly performed under vacuum conditions to enhance the capillary suction of the solution into the air- and water-free pores and to prevent external air bubbles for disrupting the impregnation process [48, 49].

IWI could be performed with a solvent only. However, if it is aimed to deposit metal nanoparticles with a considerable metal loading, the solubility of the metal precursors in the impregnation solution must be substantial. Furthermore, to obtain a homogeneous distribution of the metal precursor over the support it is key that the adsorption and diffusion of the metal precursor is balanced. To achieve this, the pH value of the impregnation must be chosen with respect to the ionic charge of the metal precursor and the PZC of the support [50]. To illustrate, if a metal nitrate solution is impregnated on a carbon support containing oxygen surface groups, the pH of the impregnation solution must be considerably low to protonate each surface group. Hence, the strong electrostatic adsorption of the cationic metal atoms and anionic surface groups will be diminished. As a result, a considerably more homogeneous distribution of the metal precursors over the carbon support surface is obtained. Next, the diffusion is enhanced with a higher precursor concentration, although this gives also rise to a higher viscosity of the solution, which in turn hampers the diffusion. Furthermore, a substantial equilibration time after impregnation and a decrease in the

macroscopic particle size by using powders, could enhance the diffusion. On the other hand, the adsorption of the metal precursor is more difficult to tune, as it is based on the adsorption equilibrium constant and the number of adsorption sites on the support, which both are unique support properties [48, 49].

Additional acidification of the impregnation solution is attributed to aqua acids, formed during the dissolving of the metal salts into an aqueous solution. The general equilibrium is shown in equation (1.8). The equilibrium lays to the right-hand side for small and highly charged metal ions within a solvation complex, as they repel acidic protons the most [51]. Furthermore, the amount of additional acidification depends on the specific metal and its corresponding concentration.

$$[M(OH_2)_6]^{n+} + H_2O \rightleftharpoons [M(OH_2)_5(OH)]^{(n-1)+} + H_3O^+ \tag{1.8}$$

After IWI the catalyst has to be dried and activated prior to catalytic use. During drying the solvent evaporates under reduced pressure and/or elevated temperatures, whereby the precursor concentration increases, until small clusters are formed onto the support. For example, in the case of an aqueous copper(II) nitrate solution impregnated on a silica support a solid trihydrate phase would be formed [52]. If the drying temperature is exceeding 90 °C, the copper nitrate species or dehydrated derivatives supported on silica become more mobile and prone to coalescence, resulting in large hydroxynitrate crystals in stagnant air [53]. To obtain a homogeneous metal distribution over the support this event must be avoided, however on carbon-based supports these events might differ. The pH value of the impregnation solution is also important during the drying of the impregnated supports, especially in the case of a co-impregnation of different metal precursors. The point of metal deposition during the drying procedure namely depends on the solubility of the corresponding metal precursors and, therefore, also on the pH of the impregnation solution. As each different metal precursor has a different effect on the pH value of the impregnation solution, due to their different aqua acid properties as just described, the pH value has to be carefully adjusted for each impregnation solution. Inevitably, solubility differences could also appear between the different metal nitrates, so these solubility effects could only be diminished.

Next, a calcination (a thermal treatment, mostly under a flow of air or nitrogen) is usually performed to eventually obtain a solid/gas interface and to subject the metal precursor to several chemical reactions. In the similar case of an aqueous copper(II) nitrate solution copper(II) oxide will then be formed, while nitric or nitrous oxide gas escapes the sample. For silica-supported catalysts this is likely to occur between 180 and 300 °C [52]. Finally, a

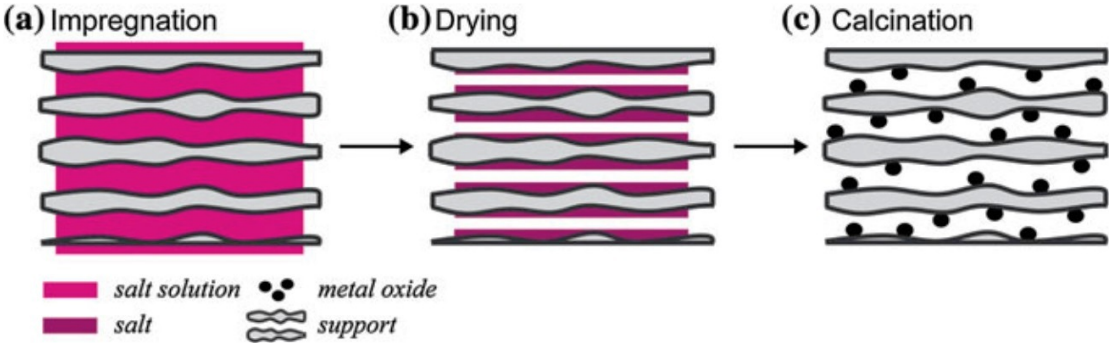

Figure 1.6 Schematic representation of the preparation of supported nanoparticles. **a** Impregnation by a metal precursor solution fills the porous support, **b** solvent removal by drying results in the deposition of the metal salt inside the pores, and **c** calcination leads the formation of metal oxide nanoparticles. Subsequent reduction (not displayed) is sometimes needed to obtain catalytically active nanoparticles. Adapted from [50].

reduction of the metal species on the support is sometimes needed to obtain catalytically active, reduced metal nanoparticles. For example, copper oxides have to be reduced to metallic copper to become catalytically active in the methanol synthesis. Figure 1.6 summarizes the preparation procedure of supported nanoparticles via impregnation.

2 Experimental Procedures

2.1 Syntheses

2.1.1 Colloidal Copper Synthesis

Synthesis of colloidal copper particles was typically performed in a 50 mL, three-necked round-bottom flask (flask 1), equipped with two glass plugs, a rubber septum and a magnetic stirrer. This flask was filled with a certain amount of copper(I) acetate (CuOAc, Sigma Aldrich 97 % purity) inside a water- and oxygen-free glove box. Prior to filling of copper(I) acetate the glassware was in most cases heat-treated at approximately 300 °C under vacuum to ensure a dry environment. Another same-like flask (flask 2) was filled in air with a certain amount of the solvent trioctylamine (TOA, Sigma Aldrich, 98 % purity) or the solvent oleylamine (OAm, Sigma Aldrich, 70 % purity) and the surfactant oleic acid (OA, Sigma Aldrich, 90 % purity, or, Fischer Chemical, 70 % purity). This flask was connected to a connection tube and a T-split gas adapter. A thermocouple was placed between the heating mantle and flask 2 and the solvent/reagent mixture was degassed under vacuum for 30 min at 120 °C while stirring vigorously. During degassing the mixture was flushed with N_2 several times. Figure 2.1 shows a typical reaction set-up for the synthesis of colloid copper particles.

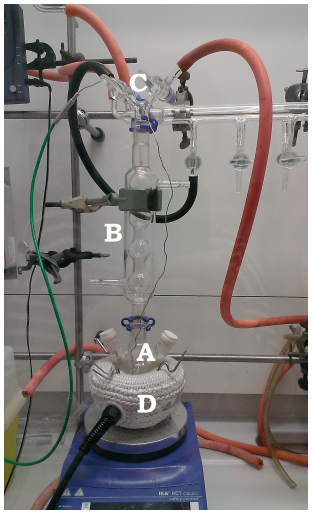

Figure 2.1 Typical reaction set-up during colloidal synthesis. **a** A 50 mL round-bottom flask was connected with a rubber septum and a glass plug (here: with two rubber septums) and a **b** connection tube (here: reflux cooler). The rubber septum was used to ensure air-free transferring of liquids. The flask was position in **d** a heating mantle. The connection tube was linked to a **c** T-split adapter, which was connected to a vacuum by a Schlenk line. The other tap of the adapter was linked to a washing bottle (not displayed) to check if a flow was present during colloid synthesis.

After cooling down of the solvent/oleic acid mixture to room temperature the flasks were switched in a most inert way. A certain amount of the solvent/oleic acid mixture was transferred by a with N_2 flushed syringe through the rubber septum to flask 1, while applying a N_2 flow through flask 2 to prevent vacuum suction. The thermocouple was placed between the heating mantle and flask 1 and the mixture was heated to 180 °C for 20 or 60 min and, next, to 270 °C for 1 h. The variable ramp was either high (36-64 °C · min^{-1}) or low (15-27 °C · min^{-1}). Prior to reaction the reaction mixture was held at 80 °C for approximately 60 min to ensure a complete dissolution of copper(I) acetate. The general procedure was adapted from [37].

The reaction parameters are given in table 2.1. For entries 1-7 the glassware appeared to be broken and was therefore not air-tight. This issue was fixed for entries 8-14. For entry 1 the solvent and reagent were not degassed prior to use, for entries 1-2 the thermocouple was held inside the reaction solution, for entry 4 a NMR tube through a rubber septum was used to make a better contact between the thermocouple and the reaction solution, and for entry 14 an oil bath was used, which could not reach the desired temperature.

Table 2.1 Experimental details of each colloidal copper synthesis, which consisted of two temperature plateaus. Entries 1-7 suffered of broken glassware. CuOAc = copper(I) acetate; TOA = trioctylamine; OA = oleic acid. **a** A new bottle of CuOAc was used. **b** Oleylamine was used instead of trioctylamine. **c** Lower purity (90 %) of oleic acid was used. **d** A slow heating rate (15-27 °C · min^{-1}) was applied.

entry	reagents			first plateau		second plateau	
	CuOAc (g; mmol)	TOA (mL; mmol)	OA (mL; mmol)	t (min)	T (°C)	t (min)	T (°C)
1	0.6; 5.0	18.3; 42	2.7; 8.6	60	180	60	270
2	0.5; 4.1	15.0; 34	2.2; 7.0	60	180	60	270
3	0.5; 4.0	14.9; 34	4.0; 12.6	60	180	60	270
4[c,d]	0.5; 4.1	15.3; 35	4.1; 12.8	60	180	60	270
5[c]	0.5; 4.1	15.3; 35	4.1; 12.9	20	195	60	295
6[b,c]	0.1; 1.0	3.2; 12	0.9; 3.3	20	180	60	270
7[b,d]	0.1; 1.0	3.8; 12	1.0; 3.3	20	195	60	285
8	0.5; 4.0	15.0; 34	4.0; 12.6	60	195	60	285
9[d]	0.1; 1.0	3.8; 9	1.0; 3.1	72	180	10	200
10	0.1; 1.0	3.8; 9	1.0; 3.1	20	100	150	180
11[b,d]	0.1; 1.0	3.9; 12	1.0; 3.3	20	180	68	260
12[a,c,d]	0.5; 4.0	15.0; 34	4.0; 12.6	35	80	60	180
13[a]	0.5; 4.0	17.0; 39	2.3; 7.3	70	80	60	195
14[a,c,d]	0.5; 4.0	17.0; 39	2.0; 6.3	80	180	–	–

2.1.2 Liquid Phase Oxidation of Carbon Nanotubes

To introduce oxygen and/or acidic groups on the pristine carbon nanotubes (CNTs, Baytubes® C 150 HP from Bayer MaterialScience) as anchoring sites, the CNTs were oxidized by liquid phase oxidation. Prior to this oxidation a grain size of > 425 µm of the CNTs was obtained. Next, 10.8 g of the sieved CNTs and 200 mL 65 % HNO_3 were poured into a 1000 mL round-bottom flask, producing immediately orange-brown colored NO_2. After connecting the flask to

a reflux cooler and two washing bottles containing H_2O, the suspension was refluxed for 1.5 h (at circa 121 °C [54]). After cooling to room temperature the solution was washed 8 times with 500 mL demiwater until a pH of 7 was reached. Finally, the product was dried for 48 h at 120 °C obtaining 10.1 g of oxidized CNTs (oxCNTs) with an approximate density ρ of $0.3\,\mathrm{g}\cdot\mathrm{mL}^{-1}$. No further sieving was applied prior to impregnations. This procedure was adapted from reference [47].

2.1.3 Incipient Wetness Impregnation and Drying

Three catalyst series were synthesized via incipient wetness impregnation (IWI), each on a different support: CNTs, oxCNTs, and HSAG (TIMREX E-HSAG500 AF-246 B78 from TIMCAL Graphite & Carbon). Each copper series consisted of the following five samples: a non-promoted copper catalyst, promoted catalysts by zinc, manganese, and chromium, and a blank impregnated 'catalyst'. The impregnation solutions were made in volumetric flasks of 25 mL in which a particular amount of $Cu(NO_3)_2{\cdot}3\,H_2O$ was added. For the promoted catalysts the corresponding metal nitrate was added on top of the copper nitrate to the impregnation solution. These chemicals and amounts are specified in table 2.2. Furthermore, to each flask 172 µL 65 % HNO_3 (Merck, pro analysis purity) was added and the flasks were filled to a total volume of 25 mL with demiwater, yielding a 0.1 M solution of HNO_3. The acidification was needed to protonate every oxygen-containing surface group of the carbon supports to diminish the strong electrostatic adsorption between the metal cations and the surface groups, leading to a more homogeneous distribution of the metal precursors. The impregnation solution for the blank impregnated 'catalysts' consisted of 0.1 M HNO_3 only.

Table 2.2 Amounts of chemicals added for each catalyst series. To each sample the corresponding amount of copper was added. For the impregnation solutions with a promoter only the corresponding promoter was additionally added.

chemical	supplier	purity (%)	amount for catalyst series (g)		
			CNT	oxCNT	HSAG
$Cu(NO_3)_2{\cdot}3\,H_2O$	Acros Organics	99	1.6	3.0	11.1
$Zn(NO_3)_2{\cdot}6\,H_2O$	Sigma Aldrich	≥ 99.0	1.1	2.0	7.4
$Mn(NO_3)_2{\cdot}4\,H_2O$	Sigma Aldrich	≥ 97.0	0.9	1.7	6.2
$Cr(NO_3)_3{\cdot}9\,H_2O$	Sigma Aldrich	99	1.4	2.7	9.9

For each IWI circa 1 g of non-dried CNTs (sieve fraction of 425-630 µm) or oxCNTs, or circa 2.5 g of 'wet' HSAG (not sieved, powder) was loaded into an under vacuum pre-weighed, 100 mL two-necked round-bottom flask. This flask was filled with a magnetic stirrer and equipped with a with quartz wool filled vacuum adapter and a septum. The support was dried for circa 1.5 h under vacuum and an elevated temperature using a heating mantle. The flask was covered with tin foil for isolation. After cooling down to room temperature the mass of the to be impregnated, dry support was determined via a mass comparison with the under vacuum pre-weighed glassware. The volume of impregnated solution V_{imp} was obtained via equation (2.1), which illustrates the dependence on the with N_2 physisorption-obtained total pore volume (PV), as described in section 2.2.1:

$$V_{\mathrm{imp}} = \mathrm{PV} \cdot m_{\mathrm{sup,dry}} \tag{2.1}$$

in which $m_{\mathrm{sup,dry}}$ is the mass of the dry support in g and PV the total pore volume in $\mathrm{cm}^3 \cdot \mathrm{g}^{-1}$.

During IWI an impregnation solution with a volume equal to V_{imp} was added with a syringe and a bent needle through the septum in a dropwise manner to the dried support. The IWI was performed while heavily stirring and while the glassware was under a vacuum. The impregnated support was dried overnight under vacuum at room temperature without prior exposure of the impregnated sample to atmospheric pressure . For the CNT- and oxCNT-supported catalysts this drying procedure was performed without stirring to maintain the sieve fractions. As the catalysts supported on HSAG existed of a fine powder stirring was applied to these impregnated carbon supports.

2.1.4 Catalyst Preparation by Direct Reduction

To prepare active catalysts for the methanol synthesis the powders of impregnated support with metal nitrate species obtained after IWI and drying, as described in section 2.1.3, were reduced without prior calcination. The dry, impregnated supports were loaded into a glass tube reactor (diameter = 24 mm). The pellet heights were measured to calculate the gas hourly space velocity (GHSV).

The reactor was installed in a low-pressure heat treatment set-up with the lines connected in such a way a fluidized bed reactor was obtained. A H_2 leak test was performed at room temperature for circa 2 min. Via a mass-flow controller with a flow maximum of $100\,mL \cdot min^{-1}$ the direct reduction was performed via the parameters specified in table 2.3 (steps 1-4). This set of parameters was adapted from Van der Wal's bachelor's thesis [47], in which valuable catalytic results were reported for this type of catalysts. Within this procedure the initial GHSVs were not kept constant between the differently supported catalysts, but the volumetric flow was constant.

After the direct reduction the reactor was thoroughly flushed with N_2 for 300 min at room temperature (step 5 in table 2.3) to eliminate the presence of H_2 before the *in situ* oxidation took place (steps 6-9). This oxidation was performed to oxidize/passivate the copper metal to Cu_2O/CuO in a reproducible and controlled way as copper metal is not stable in air. After this treatment the catalysts were called as-synthesized or fresh catalysts.

Table 2.3 Program for direct reduction under 20 vol% H_2/N_2 at 230 °C and *in situ* oxidation under 15 vol% O_2/N_2 at 200 °C. A thorough flushing step (step 5) was applied to avoid gaseous contact of H_2 and O_2. **a** A heating rate of $1\,°C \cdot min^{-1}$ indicated an isothermal step. **b** For catalyst Cr_2O_3-Cu/HSAG step 5 was shortened to 150 min due to time restrictions.

step	t (min)	T (°C)	rate[a] ($°C \cdot min^{-1}$)	volumetric flow ϕ_V ($mL \cdot min^{-1}$)		
				N_2	H_2	O_2
1	9	38	2	80	20	–
2	96	230	2	80	20	–
3	150	230	1	80	20	–
4	120	20	20	80	20	–
5[b]	300	20	1	100	–	–
6	60	20	1	95	–	5
7	180	200	1	95	–	5
8	60	200	1	85	–	15
9	∞	20	20	100	–	–

2.1.5 Second Catalyst Reduction for Titration Analysis

To investigate the effect of the direct reduction procedure during the catalyst preparation, as described in section 2.1.4, on the amount of oxygen-containing groups in the oxCNTs, titrations were performed. In fact, this direct reduction could in principle reduce the surface groups in the oxCNT support next to the copper oxide species. As the reduction of these surface group could be incomplete after the direct reduction at 230 °C a second reduction towards a higher temperature (350 °C) was applied to investigate the oxCNT support reduction. Titrations, as described in section 2.2.2, were eventually performed to probe acidity changes between these catalysts.

Therefore, two as-synthesized catalysts, ZnO-Cu/oxCNT and Cr_2O_3-Cu/oxCNT, of which the preparation is described in section 2.1.4, underwent a post-reduction under 5 vol% H_2/N_2 and subsequent mild, *in situ* oxidation. Next, circa 75 mg of treated or non-treated catalyst (sieve fraction of 425-630 µm) was loaded into a small, glass tube reactor (diameter = 13 mm) and installed in the low-pressure heat treatment set-up. A fluidized bed reactor was obtained by flowing the gas bottom-up through the pellet. A H_2 leak test was performed at room temperature for circa 2 min.

The reduction program is given in table 2.4. The temperature, gas feed, gas flow, and heating rate were adapted from the temperature-programmed reduction with hydrogen (H_2-TPR) parameters, as described in section 2.2.5. The *in situ* oxidation was milder compared to oxidation applied after the direct reduction during the catalyst synthesis, described in section 2.1.4, because there was no need for a full copper oxidation during the titrations.

Table 2.4 Program for reduction of the ZnO-Cu/oxCNT and Cr_2O_3-Cu/oxCNT catalysts as a post-treatment under 5 vol% H_2/N_2 at 350 °C and mild, *in situ* oxidation towards ambient conditions. **a** A heating rate of 1 °C· min^{-1} indicated an isothermal step.

step	***t* (min)**	***T* (°C)**	**rate**[a] **(°C · min^{-1})**	**volumetric flow ϕ_V (mL · min^{-1})**		
				N_2	H_2	O_2
1	1	22	1	50	–	–
2	65.6	350	5	47.5	2.5	–
3	15	350	1	47.5	2.5	–
4	90	20	20	47.5	2.5	–
5	60	20	1	50	–	–
6	30	20	1	47.5	–	2.5
7	30	20	1	45	–	5
8	30	20	1	42.5	–	7.5

2.2 Characterization Techniques

2.2.1 Nitrogen Physisorption

To characterize the supports on their porosity nitrogen physisorption experiments were carried out at 77.35 K on a Micromeritics® TriStar 3000 V6.08 A Surface Area and Porosity Analyzer apparatus. After every pressure change an equilibration time of 10 s was applied. On the resulting adsorption and desorption isotherms a couple of analyses were performed. Brunauer-Emmett-Teller (BET) analysis was carried out for $0.05 \leq p/p_0 \leq 0.25$ to obtain the BET surface area. Furthermore, a t-plot analysis based on a Harkins and Jura reference

isotherm, as displayed in equation (2.2), was performed to track micro- and mesoporosity. This reference isotherm is based on general oxidic supports and was hence applicable to the oxCNT support, although less for pristine CNTs and HSAG. Moreover, a Barrett-Joyner-Halenda (BJH) analysis was applied to estimate the pore size and cumulative pore volume of the supports. Adsorbed volumes were given in standard temperature and pressure (STP) of 273.15 K and 1 bar, respectively. For the total pore volume the single point adsorption at the highest measured p/p_0 value was used and for the average pore diameter the BJH method was applied to the desorption branch of the isotherms [55, 56].

$$t = \sqrt{\frac{13.99}{0.034 - \log \frac{p}{p_0}}} \tag{2.2}$$

2.2.2 Acid and Base Titration

To determine the amount of acidic and basic surface groups of the supports titrations were performed. Therefore, a TitraLab® TIM880 V05.1 Titration Manager was used. Typically, 65.00 mL 0.1 M KCl (Acros Organics, ≥ 99 % purity) was added to circa 25 mg bare support (CNTs, oxCNTs, and HSAG) to create a stable environment for the pH electrode. Next, the heavily stirred suspension was degassed with N_2 for 5 min to eliminate dissolved CO_2. Acid titrations (titrations of the acidic groups) were carried out with a titrant, consisting of 0.01 M NaOH (Merck, pellets, ≥ 99 % purity) and 0.1 M KCl. Sodium hydroxide was used, because it was a strong enough base to neutralize all different kinds of oxygen-containing, Brønsted-acidic groups [57]. Figure 2.2 summarizes these typical oxygen-containing surface groups together with several Brønsted-basic groups. The addition of titrant automatically stopped as a pH of 9 (for support titrations) or 10 (for catalyst titrations) was reached. The reason for this was that the supports of the catalysts appeared to be relatively basic. Base titrations (titrations of the basic groups) were carried out with 0.01 M HCl (Merck, pro analysis) and 0.1 M KCl as titrant and stopped automatically as the pH of 4 was reached or 5 mL titrant was added. To demonstrate the reproducibility of the titrations each support-only measurement was carried out in duplo.

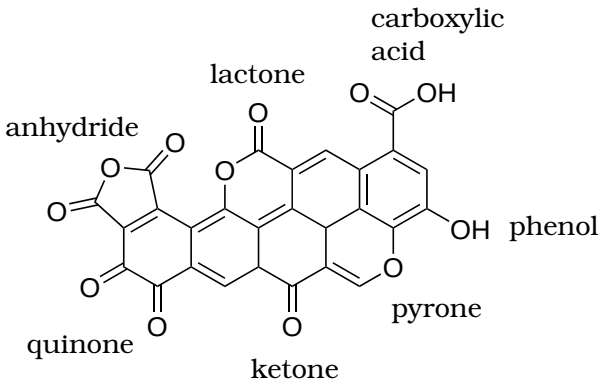

Figure 2.2 Typical oxygen functionalities, which could be present after liquid phase oxidation (LPO) of carbon nanotubes (CNTs). Phenols, lactonic groups, and carboxylic acids represent Brønsted-acidic groups, whereas the other groups are mainly basic [57]. Redrawn from [39].

For the calculation of the amount of acidic or basic groups on the support surface a cubic equation was fitted through the region of the first derivative $\left(d\,(pH)/dV\right)$ of the titration curve, in which a maximum was expected to be found. This is further clarified in figure 2.3. The acidic group density per gram of support was calculated from this maximum (the equivalence point), the concentration of the titrant, and the mass of the sample. The surface group density in

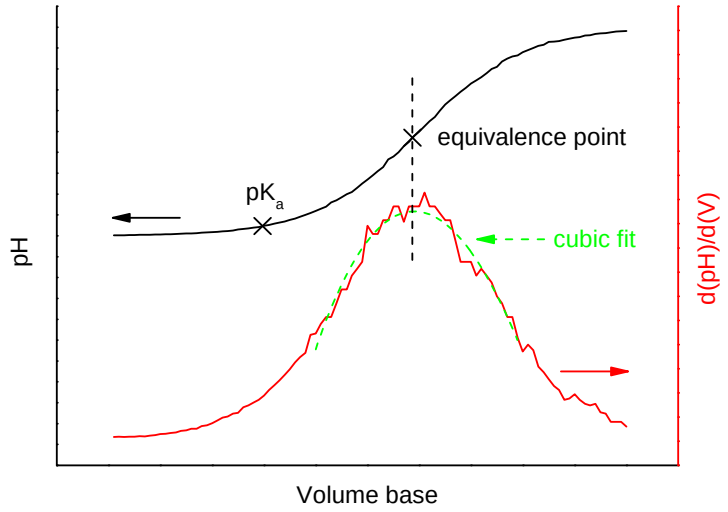

Figure 2.3 Schematic pH curve and corresponding first derivative $\left(d\,(pH)/dV\right)$ of a typical acid titration. The cubic fit (dashed green) was only applied on the region of the first derivative in which the peak maximum was expected to be found. The corresponding pH in the titration curve for this maximum is the equivalence point. The pK_a value is the pH of the titration curve corresponding to the half of the titrant volume used to reach the equivalence point.

nm^{-2} was calculated from the surface group density per gram of support and the BET surface area, obtained from N_2 physisorption. For the pK_a value the pH corresponding to the volume at the half-equivalence point was used. For each titration of a catalyst the titrated sample mass was adjusted to the amount of corresponding support present, while assuming all metal nanoparticles in the catalyst were present in their most stable oxidized form.

2.2.3 Electron Microscopy

Copper particle sizes were determined from bright-field (BF) and dark-field (DF) transmission electron microscopy (TEM) images. These images were taken from bare supports, as-synthesized catalysts and spent catalysts on a FEI™ Tecnai 12 at 120 kV. The spent catalysts were stored in a water- and oxygen-free glove box prior to specimen preparation for electron microscopy. Each sample, which consisted of an oxCNT-supported catalyst, was ground in a mortar, the powder was suspended in ethanol and sonicated for 1 min, and was dropcasted on a holey/carbon-coated Cu-grid (300 mesh). For the other samples the same procedure was performed, but the ground sample was then dropcasted on a formvar/carbon-coated Cu-grid (300 mesh). For each sample at least 100 particles were counted, where possible, and measured using iTEM® software from Olympus.

Histograms were made of the geometric particle sizes with a bin size of 0.5 nm for CNT- and oxCNT-supported catalysts and 1.0 nm for HSAG-supported catalysts to visualize the particle size distribution. In each histogram the number-averaged particle diameter d_N, the sample standard deviation s and the number of particles counted N are shown. The surface-averaged and volume-averaged particle sizes were calculated via the following equations, respectively:

$$d_S = \sqrt{\frac{1}{N}\sum_{i=1}^{N} d_i^2} \tag{2.3}$$

$$d_V = \sqrt[3]{\frac{1}{N}\sum_{i=1}^{N} d_i^3} \tag{2.4}$$

in which d_i was the i-th geometric particle diameter. These formulas originated from the following arithmetic operations: 1) the surface areas $\left(S_i = \pi d_i^2\right)$ or volumes $\left(V_i = \frac{\pi}{6} d_i^3\right)$ of each geometrical particle diameter was calculated, 2) an average particle surface area or volume was obtained, and 3) this surface area or volume was recalculated to an average particle diameter, respectively. Within these equations it is assumed all particles are spherical [58].

A FEI Talos™ F200X, a scanning-transmission electron microscope equipped with a high-angle, annular, dark-field detector and an energy-dispersive X-ray detector (HAADF-STEM-EDX), was used at 200 kV to obtain detailed chemical maps to visualize the distribution of copper and promoter species on oxCNT-supported catalysts. No particle size determination was performed with this technique. The samples were made in a similar fashion as for the TEM analysis. However, instead of ethanol isopropanol (pro analysis) was used to prevent contamination. Furthermore, holey/carbon-coated Ni-grids (300 mesh) and a low-background sample holder were used to minimize the copper signal from anything else than copper from the catalysts.

2.2.4 X-Ray Diffraction

To investigate the mean copper and promoter crystallite sizes and the oxidation state of the corresponding metals powder X-ray diffraction (XRD) measurements were performed. A Bruker AXS® D2 Phaser (2^{nd} generation) diffractometer was used with a fixed slit and an X-ray source of 30 kV and 10 mA at room temperature. All catalysts (as-synthesized and spent) and their corresponding blanks were ground prior to use and were irradiated with Cu K$\alpha_{1,2}$ radiation (λ = 1.541 84 Å) or Co K$\alpha_{1,2}$ radiation (λ = 1.790 26 Å). The step sizes (between 0.1° and 0.2°) and scan ranges were adjusted per individual measurement to provide sufficient data points per diffraction peak and hence a significant resolution.

Crystallite sizes d_{cryst} in nm were determined via the Scherrer equation, as displayed in equation (2.5), with a shape factor K_{sf} of 0.89 for spherical particles and an instrumental line broadening of 0.1 rad [59, 60]:

$$d_{\text{cryst}} = \frac{K_{\text{sf}} \cdot \lambda}{\beta \cdot \cos 2\theta} \tag{2.5}$$

in which λ is the wavelength of X-ray source in nm, β the full-width at half-maximum value of the diffraction peak in rad, and 2θ the Bragg angle of the peak maximum in rad. The β value was corrected for the instrumental line broadening.

2.2.5 Temperature-Programmed Reduction and Oxidation

The redox behavior of as-prepared catalysts was investigated on a Micromeritics® AutoChem II 2920 V4.03 Chemisorption Analyzer via temperature-programmed reduction with hydrogen (H_2-TPR) and oxidation with O_2 (TPO) measurements. The TPO measurements were only performed in a reduction-oxidation-reduction sequence to investigate the extent of copper nanoparticle oxidation after the *in situ* oxidation during the catalyst preparation. A thermal conductivity detector (TCD) was used to determine the gas uptake during the experiment. Typically, 50-100 mg of a catalyst was brought into a glass tube reactor in which the catalyst powder was enclosed by quartz wool to obtain a fixed catalyst bed.

Prior to H_2-TPR measurements the catalyst was heated to 120 °C at a rate of 10 °C · min^{-1} and was held at that temperature for 15 min under a volumetric flow of 50 cm^3 STP · min^{-1} of argon to dry the catalyst. After cooling down to room temperature the gas atmosphere was switched to a 5 % H_2/Ar stream. Under the same flow the reduction was carried out towards 500 °C with

a heating rate of $5\,°C \cdot min^{-1}$ and the temperature was held at that temperature for 10 min. During the TPO measurements the same procedure was applied with a 5 % O_2/He feedstream and pure helium for the drying of the catalyst. Helium was used as a diluent/inert gas in the TPO measurements to ensure a large difference in conductivity between these gases.
A dry ice/isopropanol cold trap was situated downstream the reactor to capture H_2O formed during the H_2-TPR. All plots were mass-corrected and a background was subtracted, which consisted of the measurement of a corresponding blank impregnated catalyst. The reduction peak between 100 and 275 °C was exclusively assigned to copper species, because the reduction of zinc [61], manganese [62], and chromium species [63, 64] appear to be at higher temperatures. Copper weight loadings wt_{Cu} in % were calculated following formula 2.6 and the stoichiometric reaction $CuO + H_2 \longrightarrow Cu + H_2O$:

$$wt_{Cu} = \frac{V_{ads} \cdot \rho_{H_2,STP} \cdot M_{Cu}}{M_{H_2} \cdot m_{sup,dry}} \cdot 100\% \tag{2.6}$$

in which V_{ads} is the volume of adsorbed H_2 in $mL_{H_2}\,STP \cdot g_{cat}^{-1}$, derived from the blank-corrected peak area, $\rho_{H_2,STP}$ the density of H_2 at STP conditions in $g \cdot mL^{-1}$, M the molar mass in $g \cdot mol^{-1}$, and $m_{sup,dry}$ the mass of dried support in g.

2.2.6 Mass Spectrometry-Coupled Thermogravimetric Analysis

To investigate the stability of the bare supports and the catalysts under reducing and oxidizing atmospheres to check if the support did not decompose during catalysis, mass spectrometry-coupled thermogravimetric analysis (TGA-MS) measurements were performed. A PerkinElmer Pyris 1 TGA apparatus, coupled to a mass spectrometer of OmniStar™ Pfeiffer Vacuum, was used for the TGA-MS measurements. Prior to the temperature increase the apparatus was flushed with N_2 at a volumetric flow ϕ_V of $20\,mL \cdot min^{-1}$ for 30 min at 30 °C or 50 °C for oxidizing and reducing atmospheres, respectively. Next, the gas atmosphere was respectively switched to a H_2 or O_2 flow at $10\,mL \cdot min^{-1}$ and the sample was immediately heated to a temperature of 800 °C with a rate of $5\,°C \cdot min^{-1}$. Finally, the temperature was kept at 800 °C for 30 min.

Each experiment was followed by a blank run, directly after the measurement. It was assumed no further decomposition occurred during these blank experiments and therefore they act as a correction for the buoyancy effect of the gas atmosphere. The correction has been applied according to equation (2.7):

$$m_{rel,i} = \frac{m_{i,a} - m_{i,b} + m_b(t=0)}{m_a(t=0)} \cdot 100\% \tag{2.7}$$

in which $m_{rel,i}$ is the i-th relative mass in %, $m_{i,a}$ and $m_{i,b}$ the i-th actual and blank mass in g, respectively, and $m_a(t=0)$ and $m_b(t=0)$ the actual and blank mass at $t = 0$ in g, respectively. The time was set to zero when H_2 or O_2 flows were introduced.

For catalysts Cu/CNT and Cu/HSAG the copper weight loading was calculated after the TGA measurement under an oxidizing atmosphere by equation (2.8):

$$wt_{Cu} = \left(m_{rel,Cu} - m_{rel,sup}\right) \frac{M_{Cu}}{M_{CuO}} \tag{2.8}$$

in which $m_{rel,Cu}$ and $m_{rel,sup}$ are the relative mass of Cu-containing catalyst and bare support in %, respectively, and M the molar mass in $g \cdot mol^{-1}$. For these calculations it is assumed that the support was fully decomposed after the measurement and that all copper was present as copper(II) oxide.

For the MS data analysis different mass-to-charge (m/z) ratios have been tracked to follow the expected decomposition products. The most intense m/z ratios of each possibly present decomposition product are summarized in table 2.5 [65]. All ion currents were normalized between 0 and 1 for visualization purposes via equation (2.9) in which I_i is the i-th ion current and I_{min} and I_{max} the minimum and maximum ion current density, respectively.

Table 2.5 m/z ratios of different compounds at which peaks in the MS pattern were expected. The italic numbers in parentheses indicate minor peaks of a compound and were not tracked. Values adapted from reference MS spectra [65].

compound	***m/z* ratio**
CO	12, 28, *(16)*, *(29)*
CO_2	12, 16, 28, 44, *(22)*, *(29)*, *(45)*, *(46)*
H_2O	17, 18, *(16)*, *(19)*, *(20)*
CH_4	12, 13, 14, 15, 16, *(17)*
H_2	2, *(1)*
O_2	16, 32
N_2	14, 28, *(29)*

$$I_{\text{rel}} = \frac{I_i - I_{\text{min}}}{I_{\text{max}} - I_{\text{min}}} \tag{2.9}$$

2.3 Stability Tests

The stability of the copper-based catalysts was tested under methanol synthesis conditions. The performance of the catalysts was tested for 250 h in a stainless steel plug-flow reactor of Autoclave Engineers®, of which the parallel reactors inside an oven are depicted in figure 2.4. The catalysts (0.45 g or 0.40 g for non-promoted or promoted catalysts, respectively, sieve fraction of 425-630 µm) were diluted with 1 mL of SiC granules (sieve fraction of 212-425 µm). These SiC granules furthermore diminish heat transfer limitations, or alternatively, the presence of the highly conductive SiC avoids the generation of hot spots. Sieve fractions were used to obtain simultaneously large enough particles to prevent pressure drops and small enough particles to prevent diffusion limitations. For the SiC an other sieve fraction was used to be able to separate this conductor/diluent from the spent catalyst. Metal-to-metal linkages were treated with the oil-based thread lubricant Silver Goop® of Swagelok®. Leak tests were performed with argon at 40 bar and room temperature.

The catalysts were reduced *in situ* to obtain catalytically active, metallic copper nanoparticles. Prior to this reduction, the gas accumulator (the lines upstream of the reactors) was flushed with 20 vol% H_2/Ar at room temperature. With the same gas feed the reduction took place at 250 °C with a heating rate of $2\,°C \cdot min^{-1}$ and this temperature was held for 150 min under a volumetric flow of $142\,mL\,STP \cdot min^{-1}$ for both reactors, while the oven was heated to 130 °C with the same heating rate. After reduction, the reactor and oven were cooled down under a 20 vol% H_2/Ar flow to 100 °C and 70 °C, respectively, with a cooling rate of $10\,°C \cdot min^{-1}$. Next, the gas accumulator was flushed with the syngas mixture (Ar:CO_2:CO:H_2 = 10:7:23:60 vol% in which argon used as an internal standard), prior to flushing the reactor for 30 min under a volumetric flow of $28\,mL\,STP \cdot min^{-1}$. This reaction mixture feed was purified using a metal carbonyl trap containing 4.0 g of H-USY zeolite (CBV-780 from Zeolyst Int., 0.5-1.5 mm) to eliminate iron carbonyls present in the pressurized gas cylinders. The trap was situated upstream the reactor and was kept at a constant temperature of 50 °C. Then, the

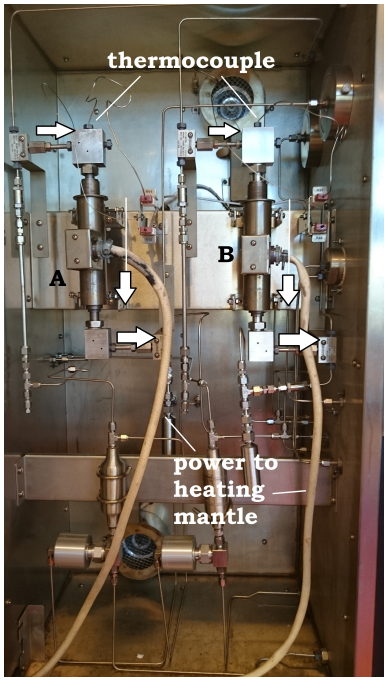

Figure 2.4 Parallel reactors (**a, b**) inside an oven used for catalytic testing. Arrows indicate the gas flow.

pressure was gradually increased over a period of 10 h to 40 bar and eventually the reactor and oven were heated to the reaction temperature of 260 °C and 150 °C, respectively, with a heating rate of $2\,°C \cdot min^{-1}$.

During the 250 h deactivation tests the decompressed product stream was analyzed using a Varian 450 gas chromatograph (GC). The GC was equipped with two channels: the first channel consisting of two series-connected HAYESEP Q (0.5Mx1/8") packed columns and a MOLSIEVE 13x (1.5Mx1/8") molecular sieve column connected to a thermal conductivity detector (TCD) at 175 °C, while the second channel consisted of a CP-SIL 8CB FS capillary column connected to a flame ionization detector (FID) at 250 °C. Before heating to the catalysis temperature three chromatograms were taken to obtain zero syngas conversion, background data. Next, at each 55 min the decompressed product stream was injected into the GC. Prior to injection at 180 °C, the GC columns were purged for 10 min with helium, the carrier gas. Then, the GC oven was held for 5 min at 30 °C, heated with a rate of $10\,°C \cdot min^{-1}$ to 190 °C, and finally held for 24 min at that temperature. After the catalytic tests, the reactors were cooled down to room temperature and another three chromatograms were taken on the GC to check if the zero syngas conversion stream did not differ prior to catalysis. All lines between the reactor and the GC were kept at 150 °C to prevent product condensation.

From integration of the GC peaks, obtained with the TCD, the corresponding amounts of CO, CO_2, and methanol could be obtained. To quantify these amounts the area of the argon GC peak was used as an internal standard. The FID provided GC patterns from which the selectivity of the $CO + CO_2$ conversion (χ_{CO+CO_2}) towards methanol, dimethyl ether (DME), and other hydrocarbons and alcohols were derived. The product selectivities were quantified using pre-calculated response factors (RFs), as depicted in appendix G, and were calculated on a carbon-atoms basis. Finally, the spent catalysts were stored in a water- and oxygen-free glove box.

2.3.1 Catalyst Activity and Selectivity Calculations

With the GC data obtained from the TCD and FID, catalytic activity and product selectivity calculations could be respectively performed. The catalytic activity can be calculated in various ways. The copper time yield (CTY) in $\mathrm{mol_{CO+CO_2}} \cdot \mathrm{g_{Cu}^{-1}} \cdot \mathrm{s^{-1}}$ is calculated via equation (2.10):

$$\mathrm{CTY}_i = \frac{\Phi_{\mathrm{CO}} \cdot \chi_{\mathrm{CO},i} + \Phi_{\mathrm{CO_2}} \cdot \chi_{\mathrm{CO_2},i}}{m_{\mathrm{Cu,react}} \cdot 100\%} \tag{2.10}$$

where Φ_{CO} is the CO flux in $\mathrm{mol} \cdot \mathrm{s^{-1}}$, $\chi_{\mathrm{CO},i}$ the converted quantity of CO in %, and $m_{\mathrm{Cu,react}}$ the mass of copper present in the reactor in g. These three physical quantities are calculated via equations (2.11), (2.12), and (2.13), respectively. $\Phi_{\mathrm{CO_2}}$ and $\chi_{\mathrm{CO_2},i}$ are like-wise calculated.

$$\Phi_{\mathrm{CO}} = \frac{\phi_V \cdot p_{\mathrm{cal}} \cdot x_{\mathrm{CO}}}{R \cdot T_{\mathrm{cal}}} \tag{2.11}$$

$$\chi_{\mathrm{CO},i} = \frac{\left(\frac{\mathrm{CO}}{\mathrm{Ar}}\right)_{\mathrm{feed}} - \frac{\mathrm{CO}_i}{\mathrm{Ar}_i}}{\left(\frac{\mathrm{CO}}{\mathrm{Ar}}\right)_{\mathrm{feed}}} \cdot 100\,\% \tag{2.12}$$

$$m_{\mathrm{Cu,react}} = \frac{m_{\mathrm{cat,react}} \cdot V_{\mathrm{imp}} \cdot c_{\mathrm{imp,Cu}} \cdot M_{\mathrm{Cu}}}{V_{\mathrm{imp}}\left(c_{\mathrm{imp,Cu}} \cdot M_{\mathrm{CuO}} + c_{\mathrm{imp,prom}} \cdot M_{\mathrm{prom}}\right) + m_{\mathrm{sup}}} \tag{2.13}$$

In equation (2.11) ϕ_V is the volumetric flow in $\mathrm{m^3} \cdot \mathrm{s^{-1}}$, x_{CO} the volume fraction of CO present in the feed stream, R the gas constant in $\mathrm{J} \cdot \mathrm{mol^{-1}} \cdot \mathrm{K^{-1}}$, and p_{cal} and T_{cal} the pressure and temperature at 1 atm in Pa and 298 K, respectively, at which the mass flow controller was calibrated. In equation (2.12) CO_i and Ar_i are the i-th TCD peak area of CO and Ar, respectively, and the TCD peak area ratio is corrected to the ratio in the feed stream prior to catalysis. In equation (2.13) $m_{\mathrm{Cu,react}}$ and $m_{\mathrm{cat,react}}$ are the total mass of copper present in the reactor and the catalyst mass loaded in the reactor in g, respectively. V_{imp} is the volume of impregnation solution in L added to the support mass m_{sup} in g, $c_{\mathrm{imp,Cu}}$ and $c_{\mathrm{imp,prom}}$ in the concentrations of Cu and the promoter in the impregnation solution $\mathrm{mol} \cdot \mathrm{L^{-1}}$, respectively, and M_{Cu}, M_{CuO}, and M_{prom} the molar masses of Cu, CuO, and the oxidized promoter in $\mathrm{g} \cdot \mathrm{mol^{-1}}$, respectively.

Next to the CTY the catalytic activity can be calculated directly from the methanol production, called normalized methanol activity (NA_i). This is calculated via equation (2.14). Furthermore, for the time-on-stream t the relation in equation (2.16) is used. The relative methanol activity (RA_i) was calculated via equation (2.15).

$$\mathrm{NA}_i = \frac{\mathrm{MeOH}_i}{\mathrm{Ar}_i} \cdot \left[\left(\frac{\mathrm{MeOH}}{\mathrm{Ar}}\right)_{\mathrm{max}}\right]^{-1} \cdot 100\,\% \tag{2.14}$$

$$\mathrm{RA}_i = \frac{\mathrm{NA}_i \cdot z_{\mathrm{CO+CO_2},t=0}}{z_{\mathrm{CO+CO_2},t=0,\mathrm{max}}} \tag{2.15}$$

$$t = 0 \text{ at } \mathrm{NA}_i = \mathrm{NA}_{\mathrm{max}} \tag{2.16}$$

In equation (2.14) MeOH_i is the i-th TCD peak area of methanol. In equation (2.15) $z_{\mathrm{CO+CO_2},t=0}$ is the catalyst mass-based activity at time-on-stream t of 0, which is further specified in equation (2.18). Furthermore, $z_{\mathrm{CO+CO_2},t=0,\mathrm{max}}$ is this particular activity for the catalyst in the corresponding oxCNT- or HSAG-supported catalyst series, exhibiting the highest CO + $\mathrm{CO_2}$ conversion $\chi_{\mathrm{CO+CO_2},t=0}$ at time-on-stream t of 0.

Furthermore, the catalytic activity could also be derived indirectly from the CO + CO_2 consumption via the catalyst mass-based activity z_{CO+CO_2}. The total CO + CO_2 conversion (χ_{CO+CO_2}) in % and the z_{CO+CO_2} in $mol_{CO+CO_2} \cdot kg_{cat}^{-1} \cdot h^{-1}$ are calculated via equation (2.17) and (2.18), respectively.

$$\chi_{CO+CO_2,i} = \frac{\Phi_{CO} \cdot \chi_{CO,i} + \Phi_{CO_2} \cdot \chi_{CO_2,i}}{\Phi_{CO} + \Phi_{CO_2}} \cdot 100\,\% \tag{2.17}$$

$$z_{CO+CO_2,i} = \frac{\Phi_{CO} \cdot \chi_{CO,i} + \Phi_{CO_2} \cdot \chi_{CO_2,i}}{m_{cat,react}} \cdot \frac{3.6 \cdot 10^6}{100\,\%} \tag{2.18}$$

Finally, the turn over frequency (TOF) is an activity measure for the amount of CO and CO_2 molecules converted per copper surface atom per second and is calculated in s^{-1} via equation (2.19). The copper dispersion D_{Cu} used in equation (2.19) is specified in equation (2.20).

$$TOF_i = \frac{\left(\Phi_{CO} \cdot \chi_{CO,i} + \Phi_{CO_2} \cdot \chi_{CO_2,i}\right) \cdot M_{Cu}}{D_{Cu} \cdot wt_{Cu} \cdot m_{cat,react}} = \frac{z_{CO+CO_2,i} \cdot M_{Cu}}{D_{Cu} \cdot wt_{Cu}} \cdot \frac{100\,\%}{3.6 \cdot 10^6} \tag{2.19}$$

$$D_{Cu} = \frac{6 V_m}{A_m \cdot d_S} \approx \frac{1.04}{d_S} \tag{2.20}$$

In equation (2.19) wt_{Cu} is the copper weight loading in % and in equation (2.20) V_m and A_m are the molar mass in nm^3 and molar particle area in nm^2, respectively, and d_S the surface-averaged particle diameter in nm, obtained from TEM. For copper V_m is $7.09 \times 10^{21}\,nm^3$ and A_m is $4.10 \times 10^{22}\,nm^2$ [66], resulting in the approximation on the most right lid of equation (2.20). The TOF values are calculated prior and after catalysis, mathematically at $i = 0$ and $i = i_{max}$, respectively.

The uncertainty in the TOF values is estimated by the uncertainty (here: standard deviation s) in the with TEM-obtained, surface-averaged particle diameter. Furthermore, it is assumed that the other variables, such as the TCD peak areas and the copper weight loading, had a much lower relative uncertainty. Therefore, the estimation followed equation (2.21).

$$s_{TOF,i} = \frac{s_{d_S}}{d_S} \cdot TOF_i \tag{2.21}$$

The TOF values between the as-synthesized and corresponding spent catalysts are independent of the particle growth, because larger is it calculated per surface copper atom. If a loss of promoter effect might be present the difference in TOF values between the as-synthesized and spent catalysts $s_{TOF,diff}$ is calculated via the following relation:

$$s_{TOF,diff} = \frac{TOF}{100\,\%} \cdot \%s_{TOF,diff} = \frac{TOF}{100\,\%} \cdot \sqrt{\%s_{TOF,f}^2 + \%s_{TOF,s}^2} \tag{2.22}$$

in which $\%s_{TOF,f}$ and $\%s_{TOF,s}$ were the percent standard deviation or relative uncertainty of the corresponding fresh ($i = 0$) and spent ($i = i_{max}$) catalyst, respectively.

The data collected from the FID was used to obtain the carbon atom-based product selectivity S in % following equation (2.23):

$$S_{it} = \frac{A_{it} \cdot N_{C,i}}{RF_i \cdot M_i} \cdot \left(\sum_{i=1}^{I} \frac{A_{it} \cdot N_{C,i}}{RF_i \cdot M_i} \right)^{-1} \cdot 100\,\% \text{ with } t \approx 0, 2, 4, \ldots \tag{2.23}$$

in which A_{it} is the peak area percentage of the i-th product at time-on-stream t in h, $N_{C,i}$ the number of carbon atoms present in the i-th product molecule, and M_i and RF_i the molar mass in $g \cdot mol^{-1}$ and the response factor (RF) of the i-th product, respectively. The RFs of n-C_1-C_{16} alkanes, primary C_1-C_8 alcohols, and DME are used and are displayed in table G.1.

3 Results and Discussion

In this project the stability and promoter effects of copper catalysts were investigated on three different supports: pristine, multi-walled carbon nanotubes (CNTs), oxidized carbon nanotubes (oxCNTs), and high surface area graphite 500 (HSAG). Firstly, in this results section the properties of the supports are shown and discussed in section 3.1. The preparation and characterization of the as-synthesized catalysts are shown in section 3.2. Finally, the reaction chosen to test the stability of these catalysts was the methanol synthesis from synthesis gas under industrially relevant conditions. Section 3.3 shows these stability tests.

3.1 Supports

3.1.1 Synthesis of Oxidized Carbon Nanotubes

The CNTs and HSAG supports were purchased and used as received without further purification. The third type of support, oxCNTs, was obtained via liquid phase oxidation (LPO) of the available CNTs in nitric acid, as described in section 2.1.2. The oxCNTs were successfully obtained and used for catalyst preparation and support characterization without further purification. Every oxCNT-supported catalyst was synthesized from one batch of oxCNTs.

3.1.2 Characterization

The supports were characterized by four techniques: N_2 physisorption, acid and base titrations, mass spectrometry-coupled thermogravimetric analysis (TGA-MS), and transmission electron microscopy (TEM). Briefly, N_2 physisorption was used to obtain the Brunauer-Emmett-Teller (BET) surface areas and total pore volumes, needed for the preparation of the catalysts, as described in section 3.1.2.1. The titrations were performed to acquire the acidic properties, as described in section 3.1.2.2. Furthermore, section 3.1.2.3 discusses the TGA-MS, which was used to check the stability of the supports in reducing and oxidizing atmospheres, relevant for the preparation of the catalysts and the conditions under which the methanol synthesis took place. TEM was used to check if there were no impurities present prior to catalyst syntheses, which could interfere with the catalyst preparation and/or the catalyst performances. The analysis concerning this last technique is further highlighted in section 3.2.2.3.

3.1.2.1 Nitrogen Physisorption

N_2 physisorption was used to track the porosity of the supports, described in section 2.2.1, and as a result to obtain important parameters for the impregnation procedure in the catalyst synthesis. The adsorption and desorption isotherms of N_2 physisorption experiment were shown in figures A.1a, c, and e. The results from the BET, t-plot, and Barrett-Joyner-Halenda (BJH) analyses are displayed in table 3.1. The plots for the BJH analysis were given in figures A.1b, d, and f.

Table 3.1 N_2 physisorption results for the bare supports. Liquid phase oxidation (LPO) of CNTs lead to an enhanced BET surface area. All supports exhibit a minor amount of micropore volume. **a** Retrieved from the desorption isotherm of the corresponding BJH plot, derived from figures A.1b, d, and f.

support	**BET surface area** $(\mathbf{m^2 \cdot g^{-1}})$	**total pore volume** $(\mathbf{cm^3 \cdot g^{-1}})$	**micropore volume** $(\mathbf{cm^3 \cdot g^{-1}}$ **at STP)**	**mean pore size (nm)**[a]
CNT	198.0 ± 0.4	1.47	0.01	57
oxCNT	254.4 ± 0.6	1.27	0.00	47
HSAG	520 ± 4	0.69	0.07	*n/d*

As can be observed in table 3.1 the liquid phase oxidation (LPO) of the CNTs led to a significantly larger BET surface area. The obtained value ($254\,m^2 \cdot g^{-1}$) correlates well with the BET surface area of the oxCNTs, obtained by Van der Wal [47] ($240\,m^2 \cdot g^{-1}$). This means that this oxidation yielded a rougher support surface compared to the non-treated CNTs, induced by the harsh oxidation treatment. This difference in roughness could also be observed in the TEM images, as shown in section 3.2.2.3 and in appendix D. Furthermore, the total pore volume barely changed. This observation might be attributed to the fact that the oxygen-containing surface groups have replaced some of the carbon in the CNTs, which could otherwise be tracked by N_2 molecules. It can be conceived that this effect will not be very significant and together with the fact that some of the outer tube walls will be etched during the harsh synthesis conditions, which would yield in contrast a larger pore volume, the total pore volume only dropped slightly.

For all supports the micropore volume was negligible and thus could be concluded that no micropores were present and that the present pore volume was due to meso- and macroporosity. From the adsorption and desorption isotherms of the tube-like supports a hysteresis loop at a very high p/p_0 value can indeed be seen, indicating large mesopores/small macropores are present. However, from the TEM analysis of the CNT and oxCNT supports, explained in section 3.2.2.3, it appeared that the supports only gave rise to small inner-pore mesopores, induced by the significantly small inner and outer tube size: approximately r_{in} was 4 nm and r_{out} was 15 nm. With a rough estimation via equation 3.1 using the CNT density ρ_{CNT} of approximately $2\,g \cdot cm^{-3}$, the pore volume per gram of support due to inner tube filling was estimated at $0.5\,cm^3 \cdot g^{-1}$. Comparing this outcome to the corresponding BJH plots in figure A.1, the small peak present at approximately 2 nm and $0.2\,cm^3 \cdot g^{-1}$ could be assigned due to this inner pore filling. This is further strengthened by the fact that this small peak could not be attributed to the tensile strength effect (TSE) as both the desorption-based and adsorption-based BJH plots contain this small peak. Briefly, this effect is a result of the instability of the hemispherical meniscus present during desorption in pores with a diameter of approximately 4 nm and is absent during pore filling [67].

The total pore volume of the CNTs and oxCNTs was significantly higher (ca. $1.3\,cm^3 \cdot g^{-1}$; table 3.1) than approximately $0.5\,cm^3 \cdot g^{-1}$ and thus the main part of the total pore volume for these supports consisted of interparticle space. This was further confirmed by the larger peak area in the BJH plots for the large mesopores/small macropores compared to the peak area due to inner pore filling.

$$PV = \frac{r_{in}^2}{\rho_{CNT} \cdot \left(r_{out}^2 - r_{in}^2\right)} \tag{3.1}$$

The BET surface area of HSAG-500 was, as expected, around $500\,m^2 \cdot g^{-1}$. The total pore volume was significantly lower compared to the tube-like supports due to the different morphology of the support: it could be most easily envisioned as an irregular composition of sheet-like structures. Furthermore, due to this irregular morphology the pore sizes were not well-defined and that resulted in a plateau-like BJH plot, as displayed in figure A.1. A sharp peak in the desorption isotherm-based BJH plot was found, but this was an artifact due to the TSE.

3.1.2.2 Acid and Base Titration

Upon liquid phase oxidation (LPO) of the CNT support oxygen-containing groups were introduced into the surface, which yielded oxCNTs. To measure to what extent this oxidation occurred acid and base titrations (titrations of the acidic and basic groups, respectively) of the oxCNTs were performed with the strong base sodium hydroxide and the strong acid hydrochloric acid, respectively, as further described in section 2.2.2. All titration curves are displayed in figure 3.1. From this figure the amount of acidic groups on the support surfaces and the corresponding pK_a values were calculated. The results of these calculations are shown in table 3.2.

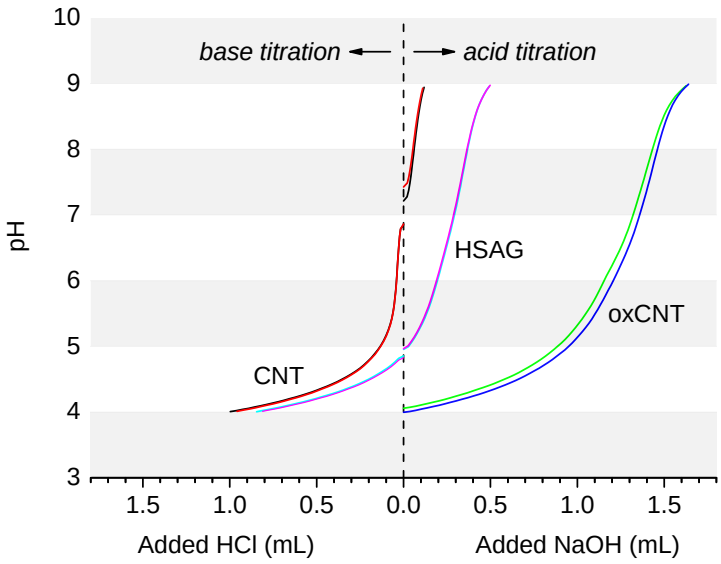

Figure 3.1 Titration curves for CNT, oxCNT, and HSAG supports. The discontinuities in the CNT and HSAG measurements were due to slightly different starting conditions between their corresponding acid and base titrations. Each support was titrated twice and demonstrated a high reproducibility. From this figure it could be concluded that the acidity trend follows oxCNT ≥ HSAG > CNT.

Table 3.2 Base titration results for CNT support and acid titration results for oxCNT and HSAG supports. Numbers in parentheses indicate duplo measurements and demonstrated the reproducibility of these titrations. **a** Absolute amount of added base or acid to reach the equivalence point. **b** pK_a values calculated from the corresponding pK_b values.

support	$m_{\mathbf{sample}}$ **(mg)**	$V_{\mathbf{HCl}}$ **(mL)**[a]	**equivalence point (–)**	**mean** $\mathbf{pK_a}$[b] **(–)**	**basic group concentration**	
					$\mu mol \cdot g_{sup}^{-1}$	nm^{-2}
CNT(1)	25.8	0.004	6.9	7.2	2	0.01
CNT(2)	25.4	0.007	6.9	7.1	3	0.01
support	$m_{\mathbf{sample}}$ **(mg)**	$V_{\mathbf{NaOH}}$ **(mL)**[a]	**equivalence point (–)**	**mean** $\mathbf{pK_a}$ **(–)**	**acidic group concentration**	
					$\mu mol \cdot g_{sup}^{-1}$	nm^{-2}
oxCNT(1)	25.5	1.399	7.7	4.7	548	1.30
oxCNT(2)	26.3	1.437	7.8	4.6	547	1.30
HSAG(1)	26.3	0.344	7.7	5.8	130	0.15
HSAG(2)	26.4	0.338	7.6	5.8	127	0.15

From figure 3.1 it could be observed that all six titration curves included only one smooth equivalence point. It was however expected to observe the individual equivalence points for each oxygen-containing subgroup, such as phenols and carboxylic acids, which are displayed in figure 2.2. This smoothness might probably originate from the diversity in acid dissociation constants (pK_as) of each individual oxygen-containing surface group, which were all in a slightly different, chemical environment. The steepness of the curve was lowest for the oxCNTs, medium for HSAG, and highest for CNTs. This trend could be attributed to the higher amount of oxygen-containing surface groups on the oxCNTs compared to HSAG and CNTs, which therefore also generated more chemically different microenvironments. As mentioned before, this led to an additional smoothness to the titration curves of the oxCNT support. Furthermore, the acidity of the oxCNTs are significantly higher compared to the HSAG and CNTs, because a larger amount of sodium hydroxide was added to reach the equivalence point. Therefore, table 3.2 shows the similar trend for the mean pK_a values of the supports.

Furthermore, the mean pK_a value of the CNTs was near neutral pH and thus a negligible amounts of acidic and basic surface groups were found. The slight acidity found for the HSAG support (pK_a 5.8) was attributed to the synthesis procedure of that material: oxygen was used during its preparation [68] and could be incorporated into the support surface. The found acidities correlate well with the reported acidities by Van der Wal [47].

Moreover, figure 3.1 shows slight pH discontinuities in the CNT- and HSAG-based titration curves between the starting points of the acid and base titrations. This was due to the fact that the amount of dissolved CO_2 in the potassium chloride solution differed from time to time, which caused a different pH value. In addition, the exact amount of weighed support and concentration (in the potassium chloride solution) influences the start pH. Next, the first measured point of the titration curve during the acid titrations (in figure 3.1 seen from the dashed, vertical line) was at a slightly higher pH than it would be expected. This meant that between the first two measurement points of each acid titration curve the sodium hydroxide concentration in the titrated solution was lower compared to the further measurements within one titration curve. The reason for this was the fact that an equilibrium was set between the end of the titrant addition tube and the pre-added potassium chloride solution, which were in contact with each other during the titration. Alternatively, during the addition

of the potassium chloride solution to the support the sodium hydroxide was able to diffuse into the titrated solution prior to the first measurement point. The opposite behavior was true for the base titrations: a lower pH value was obtained for the first measurement point of each base titration than it would be expected, due to the diffusion of hydrochloric acid into the titrated solution prior to the first measurement point. Therefore, the first measured point of every titration curve was not applicable.

3.1.2.3 Mass Spectrometry-Coupled Thermogravimetric Analysis

Thermogravimetric analysis in combination with mass spectrometry (TGA-MS) has been performed to investigate the stability of the CNT, oxCNT, and HSAG supports in the presence of H_2 and O_2, as further described in section 2.2.6. During methanol synthesis a temperature of 260 °C and a reducing atmosphere was applied. Therefore, it was important to test the stability of the carbon supports under similar conditions. Although the gas atmosphere inside the catalytic reactor was different from H_2 or O_2 only, some important results could be obtained from these experiments.

In figure 3.2a the TGA plots for the bare supports under an oxygen atmosphere are given, together with their first derivatives in figures 3.2c. Under an oxygen atmosphere it could be noticed that all supports were fully decomposed at 800 °C. The CNTs were slightly more stable compared to the oxCNTs, which might be ascribed to the fact that the rougher oxCNT support surface and the presence of defects in the form of oxygen-containing groups acted as nucleation points for support oxidation. These reasons might also be adduced to the fact that the decomposition also started considerably earlier compared to the CNTs. Furthermore, the oxygen-containing groups itself might be less stable than a graphitic surface and hence might decompose, which also leads to a lowering in the support mass.

The stability of the HSAG support behaved significantly different under an oxygen atmosphere compared to the tube-like supports. Due to its less well-defined morphology and the presence of acidic groups the decomposition started at around the same point as the oxCNTs, but stayed relatively stable above 550 °C. To illustrate, at 600 °C more than 75 % of its relative mass was still present. Nevertheless, the most relevant feature to notice in these plots is that under an oxygen atmosphere at 260 °C barely no support degradation was present.

During the TGA measurement decomposition products were analyzed using mass spectrometry (MS). These MS plots are shown in figure 3.3a, c, and e. For all supports the degradation in an oxygen atmosphere could be fully assigned to CO_2 evolution. The high ion current measured at the beginning of the m/z 28 channel could be assigned to N_2: prior to the temperature ramp an isothermal treatment in N_2 was applied and the N_2 signal decreased gradually at the start of the measurement, because it was slowly replaced by O_2. Despite the presence of N_2 during the measurement, this gradual shift towards an oxygen flow did not have any significant influence on the TGA curve, because the decomposition of the supports started when the gas exchange was almost completed. However, a proper experiment should include an isotherm with the corresponding decomposition atmosphere prior to heating.

For the TGA measurements under a hydrogen atmosphere, as displayed in figure 3.2b, and d, all supports were relatively stable over a large temperature range: at 800 °C more than 93 % of their relative masses were still present. Furthermore, it could be noted that the CNTs lost least of its mass during the measurement. This observation might be related to the negligible amount of oxygen-containing groups in the CNTs, compared to the slightly acidic HSAG and the more acidic oxCNTs, as described in section 3.1.2.2. Hypothetically, this means that under a hydrogen atmosphere the evolution of H_2O was expected in the corresponding MS plots of the oxCNT and HSAG supports, displayed in figures 3.3d and f, due to the hydrogenation of (some of) the oxygen-containing groups on their surfaces.

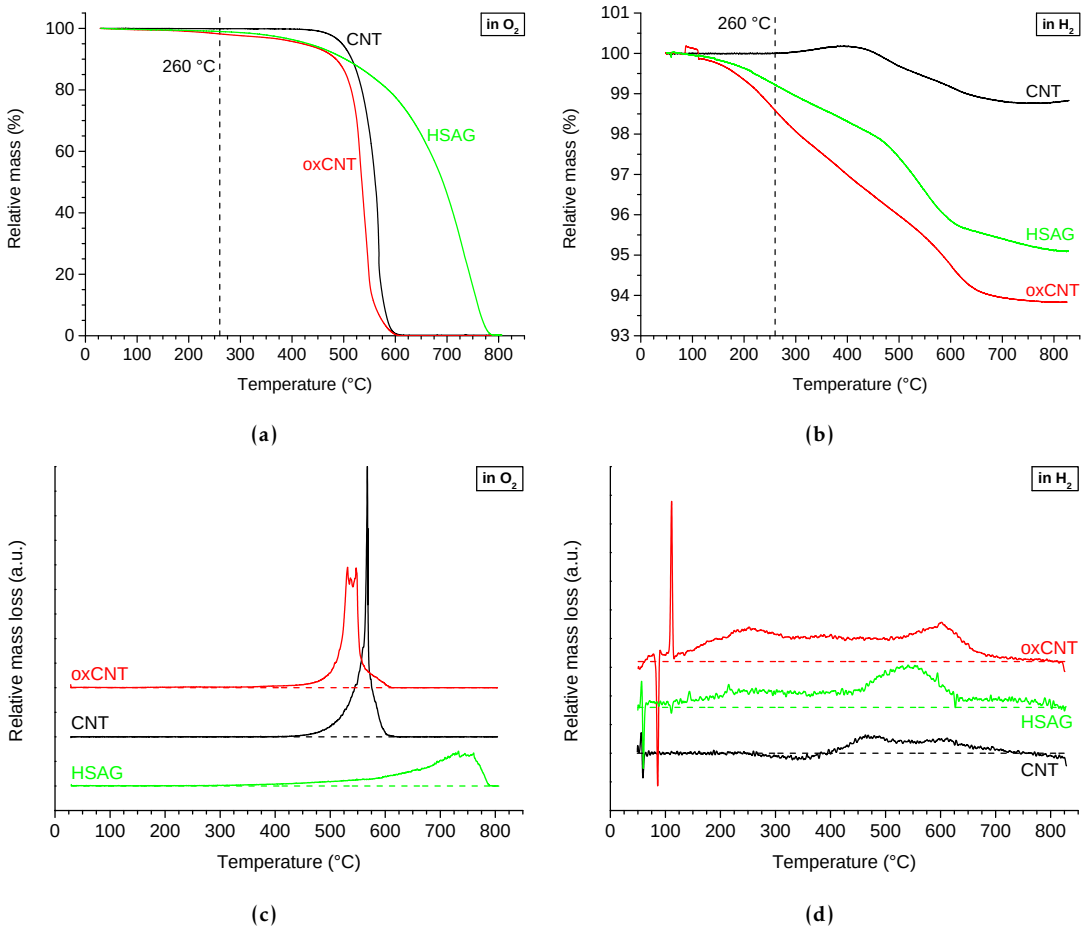

Figure 3.2 (**a**, **b**) TGA plots and (**c**, **d**) their corresponding first derivatives of bare supports in (**a**, **c**) an oxygen and (**b**, **d**) a hydrogen atmosphere. Under an oxygen atmosphere all carbon support were fully decomposed at 800 °C, whereas under a hydrogen atmosphere the supports were significantly more stable over the probed temperature range. The vertical dashed line indicates the temperature used during catalysis. Figure **b** has a different scale than figure **a**. All curves were corrected with a blank, as described in section 2.2.6.

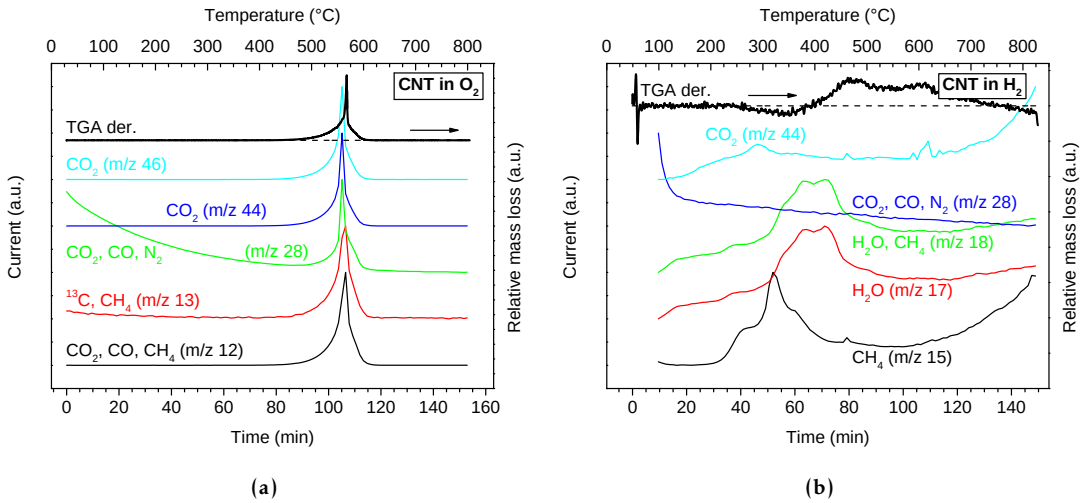

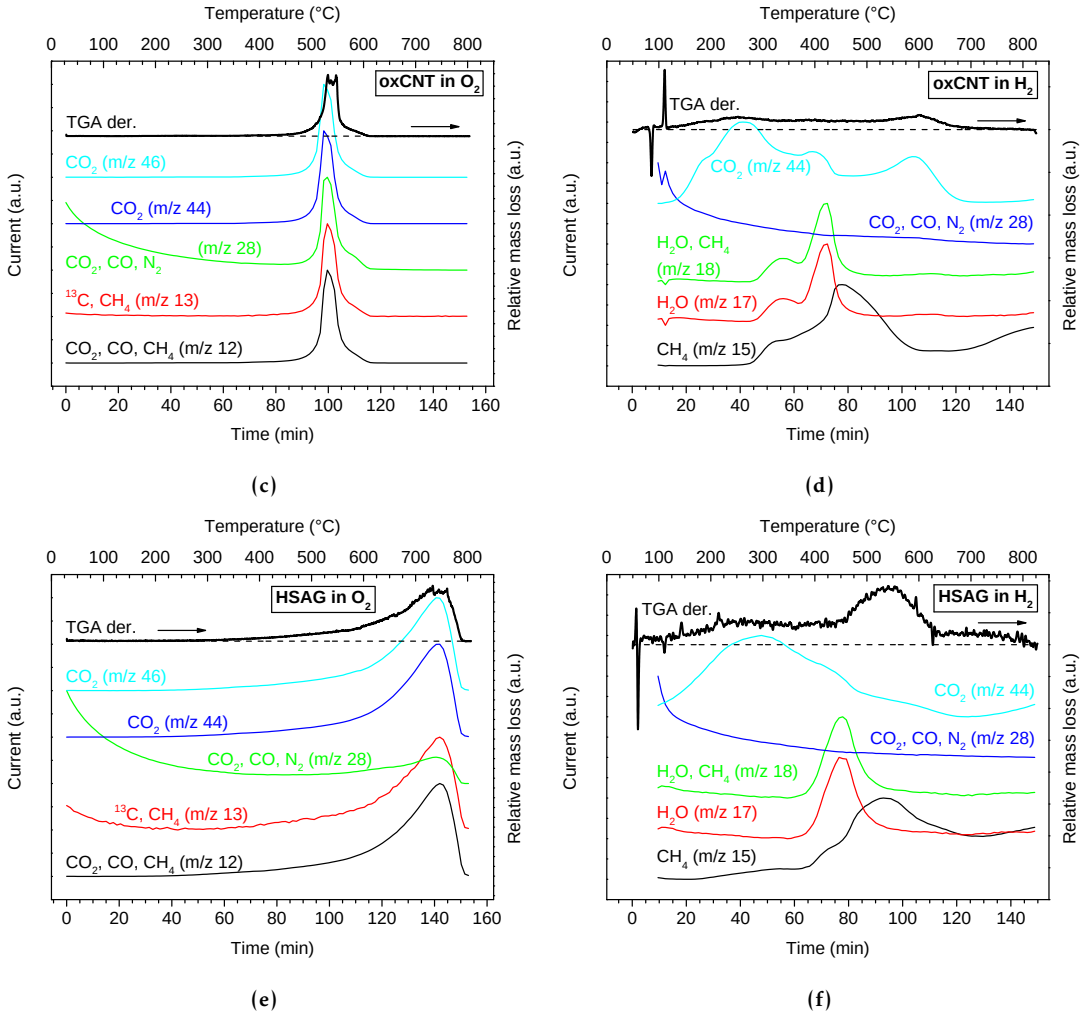

Figure 3.3 MS plots of (**a**, **b**) CNT, (**c**, **d**) oxCNT, and (**e**, **f**) HSAG support in (**a**, **c**, **e**) an oxygen and (**b**, **d**, **f**) a hydrogen atmosphere. Each first derivative of the TGA curve was shown in their corresponding MS plot. The MS curves were linked to both x-axes and the left y-axis and the TGA derivatives also to both x-axes and the right y-axis. Under an oxygen atmosphere the only detected decomposition peak was attributed to CO_2 evolution for all supports, whereas under a hydrogen atmosphere the decomposition of the oxCNT and HSAG supports were mainly based on several CO_2 peaks and one methanation peak, respectively.

Surprisingly, when comparing the aforementioned hypothesis with the corresponding MS plots, depicted in figure 3.3b, d, and f, also some other decomposition products next to H_2O were formed, such as CH_4 and CO_2. Indeed, in figure 3.3f could be observed that during the fastest decomposition of HSAG at around 550 °C, indicated by the largest peak in the first derivative of the corresponding TGA curve, methane was formed. At the other hand, the MS signal of channel m/z 15, attributed to methane evolution, of the oxCNTs in a hydrogen atmosphere, depicted in figure 3.3d, did correlate less significant with the first derivative of the corresponding TGA curve, which implied that methanation was not the main decomposition pathway of the oxCNTs. The larger amount of methanation for the HSAG support might be due to the easily accessible, exposed carbon defects, which might be more prone to methanation. Furthermore, for the MS plots obtained during TGA measurements under a hydrogen atmosphere, shown in figure 3.3b, d, and f, no clear correlations were found between the m/z signals induced by water, and the corresponding first derivative of the TGA curve. This observation would imply that all carbon supports were significantly dry and hence water loss or water generation was not the main reason for the mass losses.

As just described, the main decomposition products of the oxCNT support under a hydrogen atmosphere are not CH_4 and H_2O. Indeed, figure 3.3d suggests that the local maximums of the first derivative of the TGA around 250 °C and 600 °C correlate with the MS signals due to the production of CO_2. The CO_2 release could be attributed to direct carboxylic acid release, probably the most common oxygen-containing surface group in oxCNTs. Finally, figures 3.2d and 3.3d show an unexpected, sudden jump in the first derivative of the TGA curve of the oxCNT support around 100 °C and 10 min of the measurement. This behavior was furthermore observed in the MS signal of channel m/z 28, which was due to the presence of nitrogen. Additionally, after 10 min of the start of the TGA measurement not all nitrogen was exchanged by the hydrogen atmosphere and hence it could be concluded that the gas flow temporarily changed. Despite this behavior, this had no impact on the further progress of the measurement.

Nevertheless, a high stability of all three supports at 260 °C was observed under an oxygen and hydrogen atmosphere. This suggests that support degradation is not likely to occur during catalytic testing, although as-synthesized catalysts behaved differently in TGA than bare supports. These measurements are described in section 3.2.2.2.

3.2 Catalysts

3.2.1 Catalyst preparation

Incipient wetness (co)-impregnation (IWI) of porous carbon supports, or more specifically, pristine carbon nanotubes (CNTs), oxidized carbon nanotubes (oxCNTs), and high surface area graphite (HSAG) was performed as the first step in the catalyst preparation. This IWI was performed as thoroughly described in section 2.1.3. Briefly, the carbon supports were impregnated with an acidified solution, containing copper nitrate and, where needed, zinc, manganese, and chromium nitrates. This preparation technique was performed in such a way that the copper surface loading of each catalyst was kept similar to 1.5 atoms nm^{-2}. For the blank 'catalyst' the impregnation solution consisted of only acidified water. The metal concentrations in the impregnation solutions and the theoretical weight and surface loadings of the as-synthesized catalysts are displayed in table 3.3. After IWI the impregnated supports appeared to be dry, indicating that all added impregnation solution was migrated inside the pores and hence the IWI was succeeded.

Table 3.3 shows that the surface loadings of the CNT-supported catalysts were lower than expected: < 1.5 atoms nm^{-2}. This result could be ascribed to the fact that the needed volume of impregnation solution was calculated from an older N_2 physisorption measurement of the same CNT source. Indeed, for the surface loading calculations, of which the results are presented in table 3.3, a second N_2 physisorption experiment of the specific batch of CNTs resulted in a slightly different BET surface area and total pore volume. These results are displayed in table 3.1. The direct consequence of keeping the surface loadings constant is that the weight loadings of the corresponding metallic copper and promoter oxide could substantially differ. This was indeed reflected for the HSAG-supported catalysts, which had a considerably higher BET surface area and lower total pore volume.

All impregnation solutions were acidified by the similar amount of nitric acid with the intention to obtain similarly acidic impregnation solutions. However, the pH values of the as-made impregnation solutions, presented in table 3.3, appeared to be significantly lower than the expected pH of 1. This lower acidity might be attributed to aqua acids of which the general equilibrium for these acids is depicted in equation (3.2). Despite the weak acidity of the aqua acids the equilibrium lays to the far right-hand side, possibly induced by the

Table 3.3 Concentration of copper and promoter in the aqueous impregnation solutions with the expected weight and surface loadings of the as-synthesized catalysts. **a** Name represents the catalytically active form of the catalyst. **b** Copper loading is presented as metallic copper. **c** Loading as promoter in its most stable oxidation state, indicated by the sample name. **d** Measured pH of the corresponding impregnation solution used during IWI.

catalyst[a]		$c_{\mathbf{impreg}}$ **(mol · L^{-1})**		**weight loading (wt%)**		**surface loading (nm^{-2})**		$\mathbf{pH_{imp}}$[d]
support	metal	copper[b]	promoter[c]	copper[b]	promoter[c]	copper[b]	promoter[c]	
CNT	Cu	0.26	*n/a*	3.1	*n/a*	1.16	*n/a*	0.9
	ZnO-Cu	0.26	0.14	3.0	2.1	1.16	0.62	0.8
	MnO-Cu	0.26	0.14	3.0	1.8	1.16	0.62	0.8
	Cr_2O_3-Cu	0.26	0.14	3.0	3.8	1.16	0.62	0.8
oxCNT	Cu	0.50	*n/a*	3.9	*n/a*	1.50	*n/a*	0.8
	ZnO-Cu	0.50	0.27	3.8	2.6	1.50	0.81	0.7
	MnO-Cu	0.50	0.27	3.8	2.3	1.50	0.81	0.7
	Cr_2O_3-Cu	0.50	0.27	3.7	4.8	1.50	0.81	0.6
HSAG	Cu	1.84	*n/a*	8.4	*n/a*	1.47	*n/a*	0.2
	ZnO-Cu	1.84	0.99	7.9	5.5	1.47	0.79	−0.2
	MnO-Cu	1.84	0.99	8.0	4.8	1.47	0.79	−0.2
	Cr_2O_3-Cu	1.84	0.99	7.6	9.7	1.47	0.79	−0.5

formation of metal-metal bonds within the impregnation solution, which hence expelled additional protons.

$$[M(OH_2)_6]^{n+} + H_2O \rightleftharpoons [M(OH_2)_5(OH)]^{(n-1)+} + H_3O^+ \tag{3.2}$$

Furthermore, table 3.3 shows that the amount of acidification depended on the specific metal nitrate and its corresponding concentration. More specifically, the acidic strength of copper, zinc, and manganese aqua acids appeared to be similar, whereas chromium aqua acid was fairly more acidic. These observations correlate with reported trends from literature, as clarified in table 3.4, in which smaller and highly charged solvated metal ions result in the strongest aqua acids [51]. In practice, these different pH values for the impregnation solutions might had a significant effect on for example the particle size distributions of the as-synthesized catalysts. To investigate this effect each impregnation solution has to have a

Table 3.4 Brønsted acidic properties of aqua acids formed within impregnations solutions. Copper, zinc, and manganese aqua acids lead to a similar decrease in pH value, whereas chromium aqua acids has a higher acidic strength. **a** In an octahedral configuration, without any specified ligands. **b** Data from reference [69]. **c** Data from references [51, 70]. **d** Lowering in pH per 1 M of corresponding aqua acid, calculated from table 3.3. **e** High spin configuration.

aqua acid[a]	$r_{\mathbf{eff}}$ **(pm)**[b]	$\mathbf{pK_a}$ **value**[c]	**ΔpH (L · mol^{-1})**[d]
Cu(II)	73	8.0	-0.4
Zn(II)	74.0	9.5	-0.4
Mn(II)[e]	83.0	10.6	-0.4
Cr(III)	61.5	4.2	-0.7

Table 3.5 Approximate gas hourly space velocities (GHSVs) during direct reduction and *in situ* oxidation of the catalyst preparation. The lower GHSVs for the HSAG-supported catalysts originated from the larger amount of impregnated support compared to the catalyst masses for the tube-like catalysts. **a** GHSV in parentheses was obtained after the direct reduction.

catalyst	**GHSV (h^{-1})**		
	CNT	oxCNT	HSAG
Cu	1331	1479	783 (887)[a]
ZnO-Cu	1210	1663	887
MnO-Cu	1331	1663	634 (887)[a]
Cr_2O_3-Cu	*n/a*	1479	700
blank	1109	1479	783

similar pH value and the specific solubilities of the metal nitrates under changing pH values have to be known. However, no further investigation on this effect was applied within this thesis.

The following steps in the catalyst preparation were drying under vacuum and direct reduction with hydrogen and subsequent *in situ* oxidation with oxygen, as described in sections 2.1.3 and 2.1.4. During the direct reduction copper was reduced to metallic copper, but none of the promoters were reduced to their metallic state, as found by temperature-programmed reduction with hydrogen (H_2-TPR) measurements of the as-synthesized catalysts. This is further described in section 3.2.2.5. The gas hourly space velocities (GHSVs), depicted in table 3.5, changed to some extent over time due to the fact that the density between the impregnated supports and the corresponding as-synthesized catalysts differed to a certain degree and hence resulted in a different catalyst bed volume. Furthermore, the GHSVs between the differently supported catalysts differed due to the different initial density and amount impregnated support. The errors in these measurements were relatively large due to the low catalyst bed height.

3.2.2 Characterization

The as-synthesized catalysts were characterized with X-ray diffraction (XRD), mass spectrometry-coupled thermogravimetric analysis (TGA-MS), temperature-programmed reduction and oxidation (H_2-TPR and TPO), acid and base titrations, transmission electron microscopy (TEM), and high-angle, annular, dark-field scanning-transmission electron microscopy with energy-dispersive X-ray detectors for chemical mapping (HAADF-STEM-EDX). The results of these characterization techniques are described in this section. All catalyst names represent their catalytically active form, which is metallic copper in combination with their most stable promoter oxide. During the catalyst preparation an *in situ* oxidation was applied, which eventually resulted in the as-synthesized, partially or fully oxidized copper catalysts. This should be kept in mind when reading this section.

3.2.2.1 Temperature-Programmed Reduction-Oxidation-Reduction

To investigate if all copper species in the as-synthesized catalysts were fully transformed into CuO after the *in situ* oxidation during catalyst preparation, an *in situ* H_2-TPR/TPO/H_2-TPR treatment was performed. Specifically, the reduction-oxidation-reduction measurement was only carried out for two as-synthesized catalysts with significantly different mean copper nanoparticle sizes to check if smaller as well as larger copper nanoparticles were completely

oxidized to CuO after the *in situ* oxidation. Therefore, the non-promoted catalysts Cu/CNT and Cu/HSAG are used for these experiments, which exhibit a mean copper nanoparticle size of 6 ± 4 nm and 12 ± 7 nm, respectively. These significantly different nanoparticle sizes could be derived from table 3.8 and figures 3.9b and c of the TEM analysis. After the first H_2-TPR of the sequence up to a temperature of 300 °C all copper oxides were fully reduced to metallic copper. This statement was checked by H_2-TPR measurements of all as-synthesized catalysts up to 500 °C, as described in section 3.2.2.5. Next, TPO was performed to 400 °C to oxidize the metallic copper completely to CuO. Finally, a second H_2-TPR was performed to reduce all CuO. This procedure is sketched in figure 3.4. If indeed the TPO completely oxidized each metallic copper nanoparticle, then it was expected to observe similar peaks, due to hydrogen consumption, obtained during the first and second H_2-TPR.

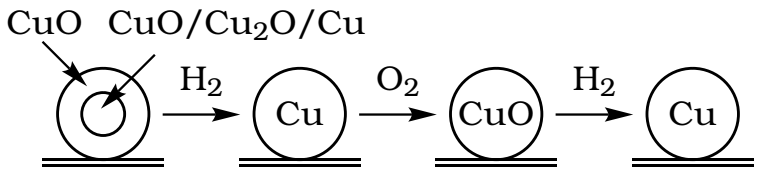

Figure 3.4 Sketch of the oxidation state of the copper species during H_2-TPR/TPO/H_2-TPR treatment. The core of the copper nanoparticles of as-synthesized catalysts might not be fully oxidized after the *in situ* oxidation during the catalyst preparation, whereas after the H_2-TPR steps of this sequence fully reduced copper was obtained.

The H_2-TPR/TPO/H_2-TPR plots are given in figure 3.5. A first feature that could be noticed from both plots was a large oxygen consumption between 350 and 400 °C of both TPO measurements. This enhanced consumption could be ascribed to support degradation. In figure 3.6a, presented in section 3.2.2.2, thermogravimetric analysis (TGA) plot from these catalysts are depicted, which indeed show support decomposition under an oxygen atmosphere within this temperature range. This comparison could be made, because the similar heating rate and amount of oxygen were used in both characterization techniques. In addition, the decomposition was even more severe for the Cu/HSAG catalyst compared to the Cu/CNT catalyst, as was also reflected by the lower support stability in the TGA curves. This was also the reason why no blank correction was applied to these H_2-TPR and TPO curves: the support degradation was different for bare supports (and possibly also for the blank

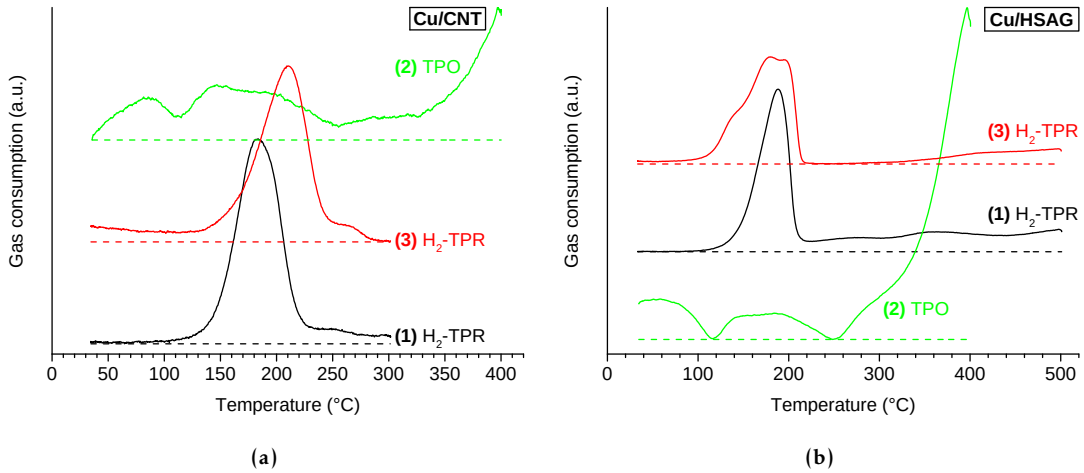

Figure 3.5 Mass-corrected H_2-TPR/TPO/H_2-TPR plots of as-synthesized **a** Cu/CNT and **b** Cu/HSAG catalysts. The peak areas visible in the (1) first and (3) second H_2-TPR plots are similar for the Cu/CNT support and different for the Cu/HSAG support. The increase in oxygen consumption after 300 °C visible in the (2) TPO plots were due to support degradation. The number in parentheses indicated the order of the treatments. No blank correction was applied.

impregnated 'catalysts') compared to Cu/CNT and Cu/HSAG catalysts. This different support decomposition could be assigned to the presence of copper in the catalysts, which is further discussed in section 3.2.2.5. Nevertheless, while assuming no copper species were lost during support degradation and the lack of a blank correction did not have a significant impact on the copper weight loading determination, important information could be extracted from these plots. Indeed, the reduction peaks only depended on the amount of copper present in the reactor.

In table 3.6 the copper weight loadings obtained with these experiments are shown in the middle columns. Furthermore, in this table the weight loadings, obtained with blank-corrected H_2-TPR measurements, are shown in the most left column. These corrected H_2-TPR results are further described in section 3.2.2.5. The theoretical copper weight loadings, as presented in table 3.3 of section 3.2.1, are given in the most right column of table 3.6. Furthermore, copper weight loadings were obtained via TGA measurements, as described in section 3.2.2.2. As could be observed from table 3.6 the copper weight loading did not change significantly for the Cu/CNT catalyst, namely from 3.5 wt% to 3.2 wt%. A conclusion could be drawn that the copper species present in the as-synthesized Cu/CNT catalyst were fully oxidized to CuO. Furthermore, from the TEM images it could be observed that all copper species for the CNT-supported catalyst series were of similar particle size, as displayed in table 3.8. Therefore, during for example X-ray diffraction (XRD) measurements, as described in section 3.2.2.4, it appeared that the copper nanoparticles for the CNT-supported catalysts were completely oxidized to CuO after *in situ* oxidation during catalyst preparation.

Table 3.6 Copper weight loadings calculated from various H_2-TPR and TPO experiments. The copper weight loadings obtained for the Cu/CNT catalyst showed that after the *in situ* oxidation during catalyst preparation and the TPO the copper nanoparticles were fully oxidized to CuO. For the larger copper nanoparticles supported on HSAG an incomplete oxidation was observed after both oxidations. **a** First and second refers to the first and second H_2-TPR measurement within the measurement series, respectively. **b** Obtained via IWI, as described in section 3.2.1.

catalyst	**H_2-TPR (wt%)**	**H_2-TPR/TPO/H_2-TPR[a] (wt%)**		**theoretical loading[b] (wt%)**
		first	second	
Cu/CNT	3.3	3.5	3.2	3.1
Cu/HSAG	3.1	3.0	3.5	8.4

For the Cu/HSAG catalyst a surprising result was noticed from table 3.6: the copper weight loading calculated after the second reduction (3.5 wt%) was barely any larger compared to the copper weight loading obtained after the first H_2-TPR (3.0 wt%). Approximately a doubling of the copper weight loading up to around 8 wt% was expected, regarding to the theoretical copper weight loading. As the increase in copper weight loading was not observed for the 12 ± 7 nm-sized copper nanoparticles of the Cu/HSAG catalyst it was plausible to assume that after a TPO up to 400 °C not all metallic copper, obtained after the first H_2-TPR, was fully oxidized to CuO. In addition, after the *in situ* oxidation at 200 °C during catalyst preparation, as described in section 2.1.4, the copper nanoparticles were not fully oxidized, following XRD experiments described in section 3.2.2.4. Hence, an oxidation temperature increase from 230 °C to 400 °C did not gave any significant further oxidation of the inner Cu_2O and/or Cu phases of the nanoparticles to the fully oxidized CuO. XRD experiments could be performed after an oxidation treatment at 400 °C to confirm the incomplete oxidation of copper. However, high temperature oxidation could cause particle growth of the copper nanoparticles

on the as-synthesized catalysts and could furthermore cause support degradation. Due to these mixed copper phases present in the HSAG-supported catalysts, particle size determination via XRD and copper weight loading determination via H_2-TPR could not be performed with high accuracy.

3.2.2.2 Mass Spectrometry-Coupled Thermogravimetric Analysis

The mass spectrometry-coupled thermogravimetric analysis (TGA-MS) technique was used to investigate the stability of the bare supports under an oxygen and hydrogen atmosphere, as explained in section 3.1.2.3. However, the deposited metals on the supports could influence the support stability, which is for particular importance during catalysis. Therefore, the stability of Cu/CNT and Cu/HSAG was tested under an oxygen atmosphere using TGA-MS. Despite of the relevance of these experiments under a reducing atmosphere and for other catalysts as well, no further TGA-MS measurements were performed for catalysts. In figures 3.6 and 3.7 the TGA curves with their corresponding first derivative and the corresponding MS plots were given, respectively.

As could be observed from the TGA plots in figure 3.6a the incorporation of copper metal species lowered the stability of the support material under an oxygen atmosphere significantly. This observation might be attributed to the fact that copper can act as an oxidation catalyst as well [71–73]. For the Cu/HSAG catalyst this support decomposition was more pronounced than for the Cu/CNT catalyst, which might be due to its higher copper weight loading (8.4 wt% vs. 3.9 wt%). At the other hand, for the HSAG support the decomposition started considerably earlier compared to the CNTs and hence the presence of copper only pronounced this degradation. Furthermore, the shape of the TGA curve for the Cu/HSAG catalyst changed considerably: the decomposition was more defined, or alternatively, the slope was far steeper compared to the TGA curve of the bare HSAG support. In addition, the Cu/HSAG catalyst showed two distinct slopes in plot in comparison with the one of the Cu/CNT catalyst.

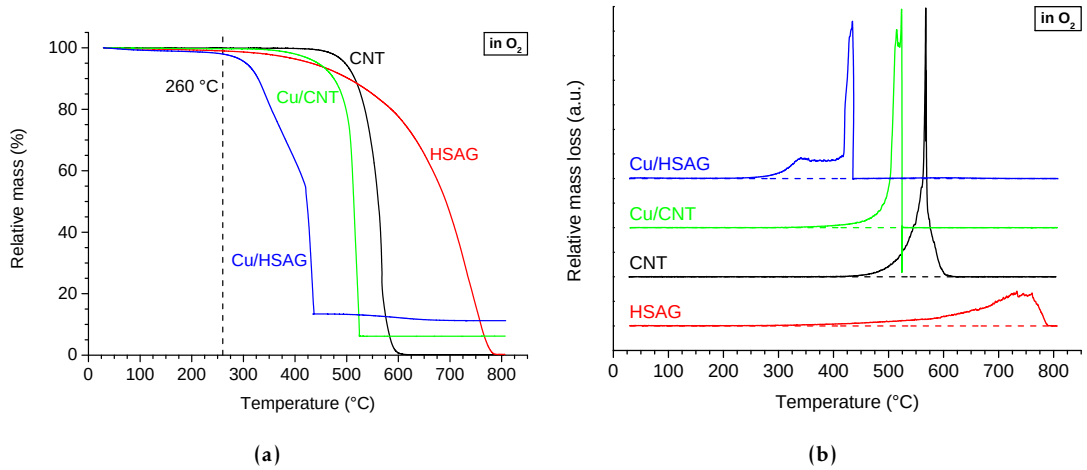

Figure 3.6 **a** TGA plots obtained under a hydrogen atmosphere of bare HSAG and CNT supports and as-synthesized Cu/CNT and Cu/HSAG catalysts with **b** their corresponding derivatives, presented in order of maximum decomposition. The TGA plots in **a** show the influence of copper on the stability of the carbon supports. Decomposition peaks in **b** were shifted to lower temperatures for the copper-based materials. The vertical dashed line represents the temperature used during catalysis.

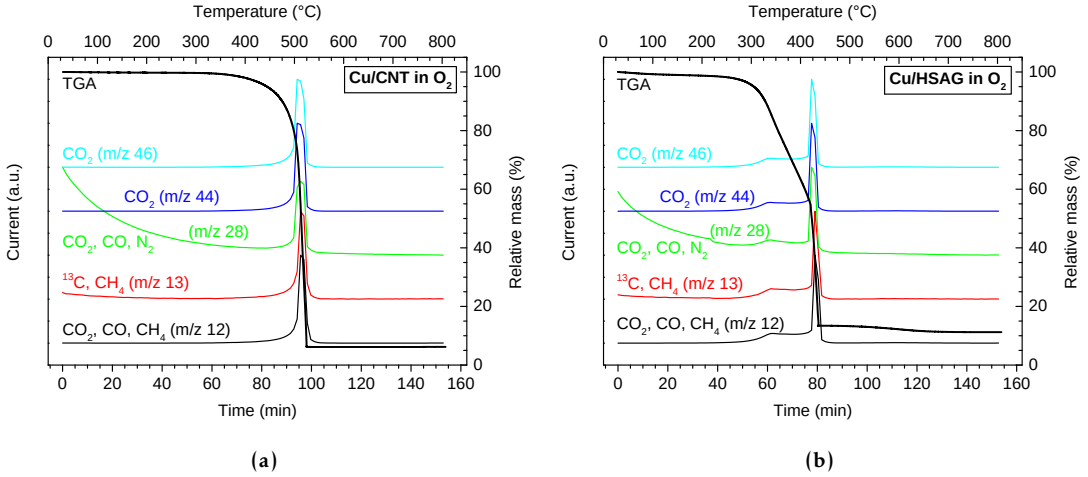

Figure 3.7 TGA-coupled MS plots of as-synthesized **a** Cu/CNT and **b** Cu/HSAG catalysts under an oxygen atmosphere. Each first derivative of the TGA curves was shown in their corresponding MS plot. The MS curves in **a** and **b** show that CO_2 was the only decomposition product. The MS curves were linked to both x-axes and the left y-axis, whereas the first derivatives of the TGA curves correspond to the right y-axis.

Regarding to the MS plots in figure 3.7 the support degradation could be fully assigned to CO_2, the thermodynamically most stable combustion product of carbon in the presence of oxygen. Furthermore, figure 3.7b shows two distinct decomposition slopes, which both plausibly correspond to a different rate of CO_2 evolution. The occurrence of these discrete slopes could not be assigned to, for example, the oxidation of the not fully oxidized Cu_2O cores, present in the large copper nanoparticles of the Cu/HSAG catalyst. This is further described in section 3.2.2.4. The reasons that the first decomposition part was not due to copper oxidation were the facts that 1) this oxidation did not even occur before 400 °C, as derived from the H_2-TPR/TPO/H_2-TPR experiments shown in section 3.2.2.1, and 2) that the stoichiometric equation (3.3) indicates that the relative mass must even slightly increase during the TGA measurement (from 143 g per mole of Cu_2O to 159 g of 2 mol CuO).

$$Cu_2O + \tfrac{1}{2}\,O_2 \longrightarrow 2\,CuO \tag{3.3}$$

From figure 3.6a the Cu/CNT and Cu/HSAG catalysts were stable under a full oxygen atmosphere at 260 °C, the temperature used during catalysis. Moreover, bare supports were more stable under a hydrogen atmosphere than under an oxygen atmosphere, as depicted in figures 3.2a-b of section 3.1.2.3. Hence, it could be assumed that the copper-functionalized supports were stable under a hydrogen atmosphere as well and therefore stable under catalytic conditions. Furthermore, the stability of the promoted catalysts could differ substantially compared to the non-promoted catalysts, due to the larger amount deposited metal and different reactivities towards oxidation. To confirm the stabilities of these supports TGA-MS measurements of the carbon-supported catalysts under reducing conditions should be performed. However, TEM analysis of the spent catalysts, described in section 3.3.3, does not show support degradation or severe particle growth of copper nanoparticles.

Next to a stability assessment, the TGA could also serve as an alternative copper weight loading determination, as all of these carbon supports decomposed completely at a relatively high temperature under an oxygen atmosphere. This determination was only applicable to the non-promoted copper catalysts, whereas for the promoted catalyst a total metal loading (copper oxide plus promoter oxide) would be obtained. In table 3.7 the copper weight loadings of the Cu/CNT and Cu/HSAG catalysts, obtained by TGA, are displayed.

Table 3.7 Copper weight loadings in wt% of Cu/CNT and Cu/HSAG catalysts obtained from TGA experiments. For both catalysts full copper oxidation towards CuO and support degradation at 800 °C were assumed. Comparisons were made with copper weight loadings obtained by H_2-TPR, as decribed in section 3.2.2.5, and theoretical weight loadings, as derived from table 3.3.

catalyst	wt_{Cu} (%)		
	TGA	H_2–TPR	theoretical loading
Cu/CNT	4.8	3.3	3.1
Cu/HSAG	8.8	3.1	8.4

From table 3.7 a good correlation for the Cu/HSAG catalyst between the copper weight loading obtained from TGA and the theoretical copper weight loading was observed, which could not be found with H_2-TPR. Despite this good correlation, for the Cu/CNT catalyst a significantly higher copper weight loading of 4.8 wt% was found via TGA compared to the theoretical weight loading of 3.1 wt%. The reasons for these different copper weight loadings obtained by the various techniques are not known, but might be due to the different assumptions and corresponding errors made between the characterization techniques. To obtain a better insight into these copper weight loadings inductively coupled plasma mass spectrometry (ICP-MS) measurements must be performed.

3.2.2.3 Transmission Electron Microscopy

Transmission electron microscopy (TEM) was applied to obtain copper (oxide) particle size distributions. From these distributions three different mean particle sizes were calculated: number-averaged, surface-averaged, and volume-averaged particle sizes: d_N, d_S, and d_V, respectively. The d_S was relevant for the turn over frequency (TOF) calculations during catalysis and the d_V was used for the comparison of crystallite sizes, obtained from XRD analysis as described in section 3.2.2.4.

As copper and the promoter metals are next to each other in the periodic table only a small difference in their atomic masses (Z) are present, which resulted in barely any Z^2 contrast in the TEM images. Therefore, no difference was observed between the copper and promoter particles. Despite no discrimination could be made, XRD analysis of the as-synthesized

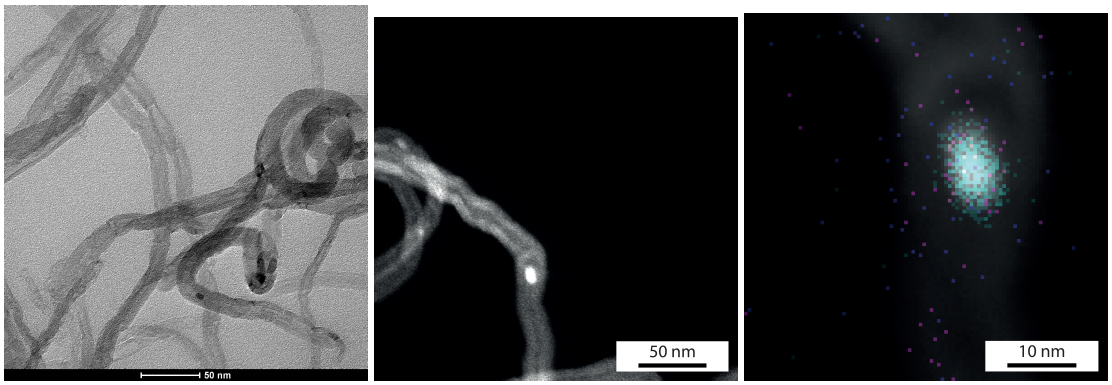

(a) oxCNT blank **(b)** MnO-Cu/oxCNT fresh **(c)** MnO-Cu/oxCNT fresh

Figure 3.8 a TEM image of blank impregnated oxCNTs; **b** HAADF-STEM image of the as-synthesized MnO-Cu/oxCNT catalyst with **c** an EDX chemical map layer on top of it. From these images a cobalt nanoparticle of approximately 5 nm was observed, which were present as the CNT growth catalyst. Co = light blue.

catalysts revealed that all promoters were finely dispersed within the catalyst sample, except for zinc oxide in the ZnO-Cu/CNT catalyst, as described in section 3.2.2.4. For that reason, it could be concluded that nanoparticles observed in TEM images consisted of mostly copper oxide. Next, the difference in particle size between copper oxide and the catalytically relevant copper metal was only small and therefore no particle size correction has been applied. From the TEM analysis of the blank impregnated oxCNTs, depicted in figure 3.8a 5 nm-sized nanoparticles were visible, which might result in disadvantageous consequences. These impurities were apparently not washed out completely during the synthesis of this support. From HAADF-STEM-EDX analysis of the as-synthesized MnO-Cu/oxCNT, depicted in figure 3.8b-c, cobalt-based nanoparticles were observed, which were present as the CNT growth catalyst. It was plausible that the nanoparticles found in the oxCNT blank were also due to cobalt.

In table 3.8 the mean copper particle sizes with their corresponding uncertainties are given. The corresponding histograms for the CNT, oxCNT, and HSAG supports are shown in the appendix in figures E.1, E.2, and E.3, respectively. Furthermore, the TEM images of each as-synthesized and spent catalyst are given in the appendix in figures D.1, D.2, and D.3.

Figure 3.9 shows selected TEM images, which illustrate the effect of the support on the mean copper particle size. This size increased from 2.1 ± 1.0 nm supported on oxCNTs, via 6 ± 4 nm supported on CNTs, towards 12 ± 7 nm supported on HSAG. Below the observed trends are further discussed per support.

Table 3.8 shows that all CNT-supported catalysts contained nanoparticles with a mean copper particle size of approximately 6 nm. As only a small amount of nanoparticles were visible on the CNTs it might be plausible that a considerable amount of copper nanoparticles were smaller than the detection limit of the TEM apparatus. This observation was also reported by Van der Wal [47]. Therefore, the mean copper particle size would be reasonably even smaller.

Table 3.8 Mean copper particle sizes obtained from TEM. d_N, d_S, and d_V are number-averaged, surface-averaged, and volume-averaged particle size, respectively. Reported uncertainties are sample standard deviations. This table shows that the copper nanoparticles on CNT-supported catalysts are significantly larger than those on oxCNT-supported catalysts, but considerably smaller than the ones on HSAG-supported catalysts. Promotion effects on the mean copper particle size were absent for the tube-like supports. **a** Relative uncertainty.

fresh catalyst		**copper particle size (nm)**			**rel. uncert.[a] (%)**
support	metal	d_N	d_S	d_V	
CNT	Cu	6 ± 4	7 ± 4	9 ± 5	57
	ZnO-Cu	6 ± 2	6 ± 2	7 ± 3	38
	MnO-Cu	5.4 ± 1.9	6 ± 2	6 ± 2	35
	Cr_2O_3-Cu	5 ± 3	6 ± 3	6 ± 4	56
oxCNT	Cu	2.1 ± 1.0	2.3 ± 1.0	2.6 ± 1.2	45
	ZnO-Cu	4.2 ± 1.6	4.5 ± 1.7	4.8 ± 1.8	38
	MnO-Cu	1.5 ± 0.8	1.7 ± 1.0	1.9 ± 1.1	56
	Cr_2O_3-Cu	2.3 ± 1.1	2.5 ± 1.2	2.8 ± 1.4	49
HSAG	Cu	12 ± 7	13 ± 8	15 ± 9	58
	ZnO-Cu	7 ± 6	9 ± 7	12 ± 10	78
	MnO-Cu	12 ± 18	21 ± 31	34 ± 50	148
	Cr_2O_3-Cu	6 ± 3	7 ± 3	7 ± 3	43

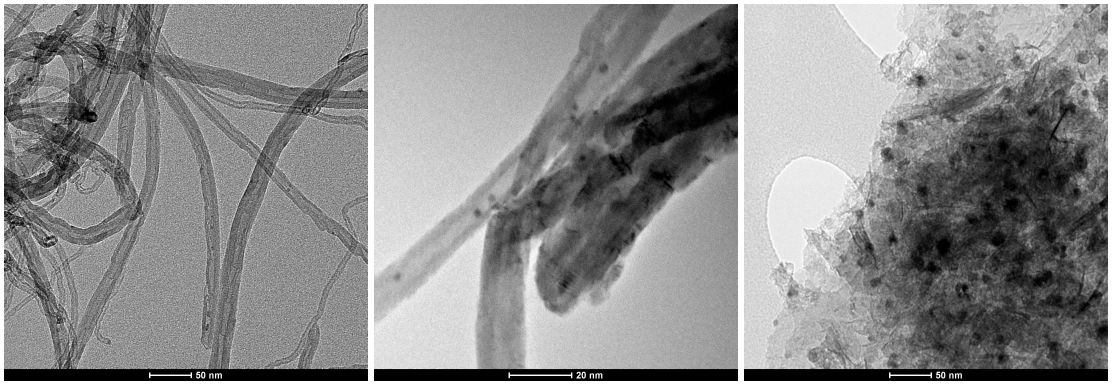

(a) Cu/CNT fresh **(b)** Cu/oxCNT fresh **(c)** Cu/HSAG fresh

Figure 3.9 TEM images of as-synthesized, non-promoted copper catalysts on different supports. The number-averaged particle sizes d_N are 2.1 ± 1.0 nm, 6 ± 4 nm, and 12 ± 7 nm, respectively. This image series indicate that the mean copper particle size was smallest if supported on oxCNTs, larger if supported CNTs, and largest if supported on HSAGs.

Furthermore, no significant differences were noticed on the mean copper particle size upon promotion. These results were in line with XRD measurements, described in section 3.2.2.4, and with the reported copper particle size by Van der Wal [47]: 4 ± 2 nm.

The copper nanoparticles on the oxCNT-supported catalysts were all considerably smaller compared to their CNT-supported counterparts, except for the Zn-promoted catalyst. This was in contrast with the mean copper particle size found by Van der Wal [47] (6 ± 2 nm). In fact, as on the oxCNT-supported catalysts also a low amount of nanoparticles were counted, the mean copper particle size might be even smaller than calculated. The reason that the observed copper particles were smaller than the ones on the CNT-supported catalysts might be ascribed to the fact that the oxCNT support surface was significantly rougher (indicated by a higher BET surface area, as shown in section 3.1.2.1) and more acidic (indicated by a lower pK_a value, as shown in section 3.1.2.2) during catalyst preparation compared to the CNTs. An explanation for this might be that the oxCNTs contained more anchoring sites for the copper ions to deposit upon and to diminish particle growth during catalyst preparation. These anchoring sites consisted of electronegative, oxygen-containing groups on which the positively charged copper ions can attach by electrostatic adsorption. The oxygen-containing groups were plausibly non-charged due to the low acidity ($<$ pH 1) of the impregnation solutions used during IWI. In addition, the roughness of the oxCNT support surface might have hampered the diffusion of the copper nanoparticles along the surface during catalyst preparation. The reason that the mean copper particle size for the Zn-promoted catalyst was slightly larger compared to the other catalysts within the oxCNT-supported catalyst series might be ascribed to a larger counted amount of approximately 5 nm-size cobalt nanoparticles, as shown in figure 3.8. To confirm this HAADF-STEM-EDX mapping has to be performed on the Cu-ZnO/oxCNT catalyst. Finally, for the oxCNT-supported catalysts no significant difference in mean copper particle size was observed upon promotion, as was also not observed for the CNT-supported catalysts as just described.

The mean copper particle size for the as-synthesized Cu/HSAG, ZnO-Cu/HSAG, and especially MnO-Cu/HSAG catalysts were considerably larger compared to their oxCNT-supported and CNT-supported counterparts. The corresponding images are depicted in figure 3.10. The larger copper mean copper particle size found for these HSAG-supported catalysts was in disagreement with the reported size by Van der Wal [47] (6 ± 2 nm). This difference might be attributed to the larger amount of impregnated support (2.5 g vs. 1 g), although this was not confirmed. The larger copper nanoparticles could not be ascribed to its different support acidity compared to CNTs and oxCNTs, as its pK_a value laid between those of the CNT and oxCNT supports, as can be observed in table 3.2. The main reason for the

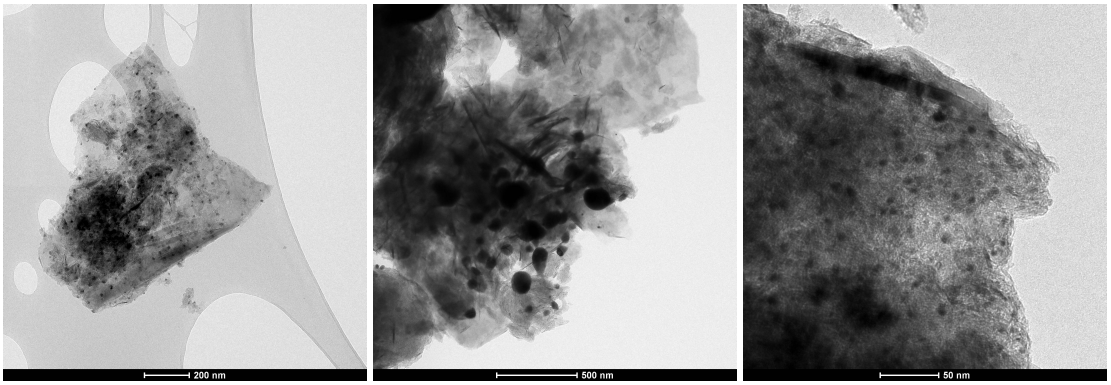

(a) Cu/HSAG fresh **(b)** MnO-Cu/HSAG fresh **(c)** Cr_2O_3-Cu/HSAG fresh

Figure 3.10 TEM images of as-synthesized or fresh, HSAG-supported catalysts. The number-averaged particle sizes d_N are 12 ± 7 nm, 12 ± 18 nm, and 6 ± 3 nm, respectively. This image series shows that the addition of Mn increased the mean copper particle size and the polydispersity, whereas Cr-promotion has the opposite effect.

larger mean copper particle sizes for these catalysts could be due to the different morphology of the support: HSAG is comprised of large sheet-like, graphitic structures on which significantly more support contact might be established compared to the tube-like morphology. That would imply that copper particles could diffuse more easily over a relatively larger support surface compared to the tube-like supports and, hence, could grow more easily to larger nanoparticles during the direct reduction in the catalyst synthesis.

For the catalysts supported on HSAG a promotion effect was nonetheless found: compared to the non-promoted catalyst, Mn-promotion led to significantly larger copper nanoparticles, whereas addition of Cr had the opposite effect. To illustrate, upon Cr-promotion the mean copper particle size was in the same order of those on the CNT-supported catalysts, namely 6 nm. Zn-promotion, however, did not have a considerable influence on the mean copper particle size. These particle size effects were also clearly visible in the TEM images, depicted in figure 3.10. To confirm the particle size effect of Mn-promotion, the MnO-Cu/HSAG catalyst was synthesized twice. Indeed, from XRD analysis it appeared that the similar crystallite size of the copper particles could be reproduced for this catalyst, as depicted in figure B.1.

Finally, table 3.8 shows that all catalysts had a mean copper particle size with a considerable, relative uncertainty, which indicated that all nanoparticles on each catalyst had a substantial size polydispersity. This polydispersity had a relatively large impact on the uncertainty in the TOFs during catalytic testing. These uncertainties can be found in table 3.15 in section 3.3.3.3. For the as-synthesized ZnO-Cu/HSAG and MnO-Cu/HSAG catalysts an even larger relative uncertainty was found, caused by the presence of remarkably large nanoparticles: for the Mn-promoted catalyst copper particles up to 200 nm were found. Therefore, the difference between the volume-averaged and number-averaged particle sizes for these catalysts were substantial, as the more larger copper particles contained more copper atoms on a volume basis compared to the smaller ones.

3.2.2.4 X-Ray Diffraction

X-ray diffraction (XRD) was used to investigate the nature of the copper and promoter species present in the as-synthesized catalysts and to determine the corresponding mean crystallite sizes. The measurements were performed as described in section 2.2.4. The diffractograms are shown in figure 3.11. In general, from the XRD diffractograms in figure 3.11 two peaks due to crystalline CuO could be observed at 2θ of 35.5° and 38.9°. Both of these peaks were comprised of two very near, intense, individual crystallographic planes: for the first, *(002)* at

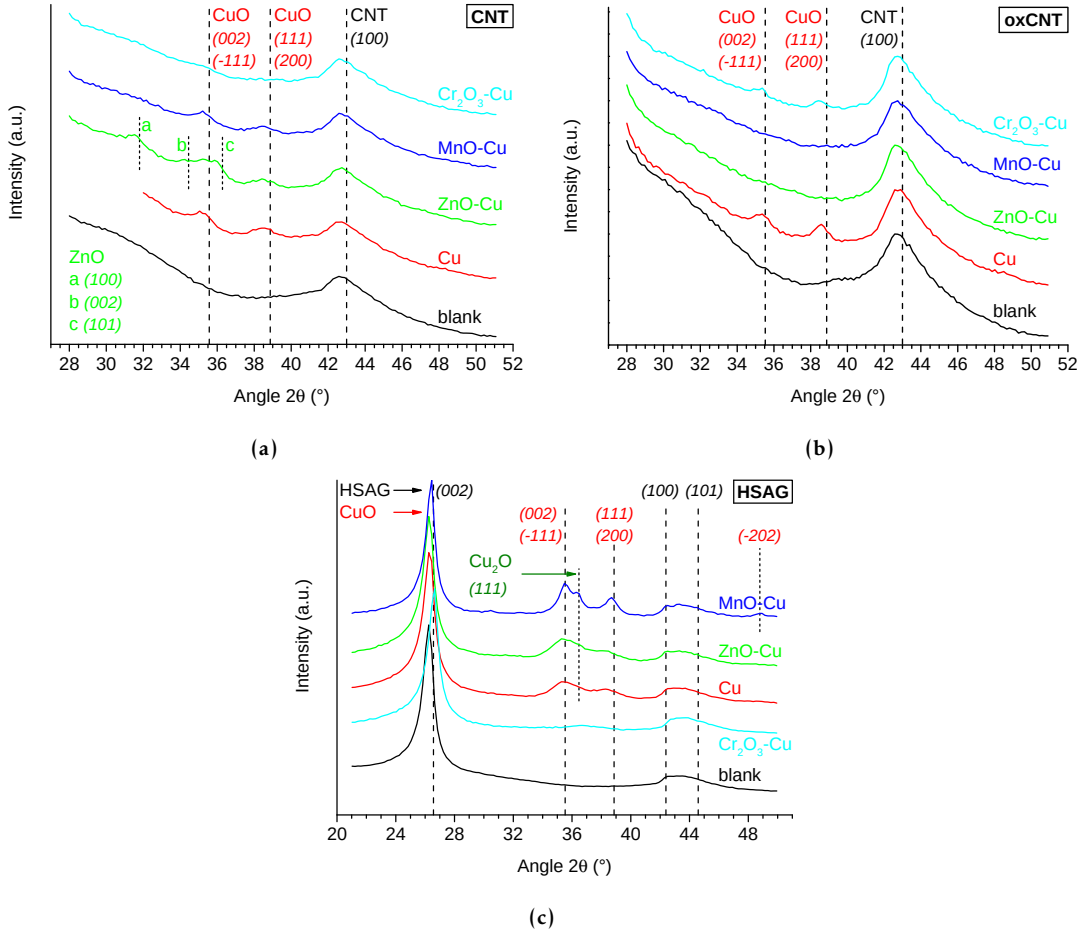

Figure 3.11 XRD diffractograms for the as-synthesized, **a** CNT-supported, **b** oxCNT-supported, and **c** HSAG-supported catalysts. All diffractograms were obtained from Cu anode X-ray radiation. Expected peak positions were marked with vertical lines, labelled with its corresponding crystallographic plane. Almost no diffraction peaks were found for the promoters. Copper crystallite sizes supported on the tube-like supports (**a**, **b**) appeared to be small. Figure **c** shows an increase and a decrease of the mean copper crystallite size upon Mn- and Cr-promotion, respectively.

35.5° (I = 60 %) and *(-111)* at 35.6° (I = 100 %), and for the second, *(111)* at 38.8° and *(200)* at 39.0°, both of maximum intensity. Therefore, the two combined peaks were broadened to some extent and resulted inevitably in smaller crystallite sizes.

Next to the peaks caused by crystalline CuO, diffraction peaks due to the support were observed: the *(100)* crystallographic plane of CNTs at 43.0° in figures 3.11a-b and the *(002)*, *(100)*, and *(101)* crystallographic planes of HSAG at 26.6°, 42.4°, and 44.6°, respectively, in figure 3.11c. Moreover, for the ZnO-Cu/CNT catalyst, depicted in figure 3.11a, three peaks for crystalline ZnO were found: the *(100)*, *(002)*, and *(101)* crystallographic planes at 31.8°, 34.5°, and 36.3°, respectively. As the peaks in the 2θ range 33-37° were caused by both crystalline ZnO and CuO, only the *(100)* ZnO peak was used for the ZnO crystallite size determination, whereas the combined *(111)*-*(200)* was used for the CuO size.

Finally, for the MnO-Cu/HSAG and less pronounced for the ZnO-Cu/HSAG catalyst, depicted in figure 3.11c, a right-sided shoulder was present in the CuO peak at 35.5°. This was ascribed to the *(111)* crystallographic plane of Cu_2O, which was present in the not fully oxidized core of the copper-based nanoparticles. The incomplete oxidation correlated with the large mean copper particle size for these catalysts, as derived from TEM analysis in section 3.2.2.3. In addition, the presence of Cu_2O was in line with the H_2-TPR experiments, described in

section 3.2.2.5, and with the H_2-TPR/TPO/H_2-TPR experiments, described in section 3.2.2.1. No diffraction peaks for metallic copper were observed in the diffractograms of the as-synthesized, HSAG-supported catalysts, which indicated that the cores of every copper nanoparticle was oxidized to at least some extent. Moreover, figure 3.11c qualitatively describes that the diffraction peak due to the *(002)-(-111)* CuO crystallographic planes was most sharp upon Mn-promotion, less sharp for the Zn-promoted and non-promoted catalysts, and considerably broad for Cr-promotion. As a result, the following qualitative trend of the CuO crystallite sizes by promotion could be observed: Mn > Zn ≈ non-promoted > Cr. This was also in line with the volume-averaged particle sizes, obtained with TEM as described in section 3.2.2.3.

In addition, no peaks due to the addition of promoters were found, except for ZnO in the ZnO-Cu/CNT catalyst, as depicted in figure 3.11a. This would suggest that the zinc species were either 1) finely dispersed over the support surfaces, 2) amorphous, or 3) barely present in the catalyst. The intensity of the peaks depends on the weight loading of the promoters in the catalyst (ranging from 1.8 to 9.7 wt%), but these loadings should be high enough to observe at least one diffraction peak due to a promoter. Indeed, from the STEM-HAADF-EDX characterizations of the as-synthesized MnO-Cu/oxCNT and Cr_2O_3-Cu/oxCNT catalysts, described in section 3.3.1, it appeared to be the first case: the promoter species were finely dispersed over the surface. Hence, most particles visible with TEM were largely composed of copper, assuming that all promoters were finely dispersed in all catalysts.

Since no diffraction peaks were observed for manganese and chromium oxides the oxidation state of these metals could not be determined. To obtain the information in which oxidation state the manganese and chromium promoters were present in the as-synthesized catalysts, X-ray photoelectron spectroscopy (XPS) should be performed. To obtain a suggestion about the oxidation states during catalysis, an XPS experiment has to be performed after an *in situ* reduction.

Table 3.9 presents the CuO crystallite sizes obtained by the two peak maximums at 35.5° and 38.9°. From some diffractograms no CuO diffraction peaks were visible and hence no crystallite size determinations could be performed. This would again suggest that the copper (and promoter) species for those catalysts were finely dispersed over the support surface.

From table 3.9 it could be observed that the CuO crystallite sizes of the CNT-supported catalysts were similar to the volume-averaged particle size, obtained by TEM. This observation suggested that for these catalysts the copper particles consisted of only one crystallographic domain. Furthermore, for the Cu/CNT and MnO-Cu/CNT catalysts an equal CuO crystallite size was obtained between the two observed diffraction peaks, indicating a spherical shape of the CuO nanoparticles. This result was in line with TEM analysis, described in section 3.2.2.3. Moreover, in the ZnO-Cu/CNT catalyst crystalline ZnO was found with approximately the same crystallite size of CuO. Therefore, during TEM analysis both ZnO and CuO nanoparticles were probably counted, which could not be discriminated from each other by Z^2 contrast only. Finally, no promoter effects on the CuO particle sizes were found for the CNT-supported catalysts: all CuO particle sizes for each catalyst in the CNT-supported catalysts were similar, as was in agreement with the TEM analysis described in section 3.2.2.3.

For the oxCNT-supported catalysts no diffraction peaks due to CuO were found upon Zn- and Mn-promotion. This was in line with the small volume-averaged particle sizes d_V observed with TEM, as described in section 3.2.2.3. The reason why no diffraction peaks due to ZnO were found on the oxCNTs compared to the CNTs might be attributed to the higher amount of oxygen-containing surface groups for the oxCNTs. Indeed, following TEM analysis this led to smaller copper nanoparticles and plausibly also to smaller zinc-based nanoparticles. Despite the presence of small nanoparticles on all oxCNT-supported catalysts, diffraction peaks due

Table 3.9 CuO crystallite sizes determined by XRD, compared to d_V from TEM. X-ray source: Cu anode. For as-synthesized catalysts absent in this table no peaks due to CuO were found. **a** Volume-averaged copper particle diameter. **b** Crystallite size with corresponding peak maximum at 31.4° was for ZnO. **c** Peak due to crystallographic planes *(111)* and *(200)* overlapped too much with *(100)* peak of CNTs. **d** K_{sf} in Scherrer equation different due to presence of a crystalline Cu_2O core in copper nanoparticles. **e** All four mentioned CuO crystallographic planes overlapped to one peak at 36.6°.

catalyst		**CuO cryst. planes *(002), (-111)***		**CuO cryst. planes *(111), (200)***		**d_V from TEM[a] (nm)**
support	metal	d_{cryst} (nm)	$2\theta_{max}$ (°)	d_{cryst} (nm)	$2\theta_{max}$ (°)	
CNT	Cu	9	35.1	7	38.5	9 ± 5
	ZnO-Cu[b]	9	31.4	8	38.4	7 ± 3
	MnO-Cu	11	35.2	9	38.5	6 ± 2
	Cr_2O_3-Cu[c]	8	35.3	*n/a*	*n/a*	6 ± 4
oxCNT	Cu	9	35.2	11	38.5	2.6 ± 1.2
	Cr_2O_3-Cu	17	35.3	13	38.5	2.8 ± 1.4
HSAG	MnO-Cu[d]	*n/a*	*n/a*	11	38.7	34 ± 50
	Cr_2O_3-Cu[e]	4	36.6	*n/a*	*n/a*	7 ± 3

to CuO were found for the Cu/oxCNT and Cr_2O_3-Cu/oxCNT catalysts. In addition, the calculated crystallite sizes found for these catalysts were significantly larger than their corresponding d_V: 9-17 nm vs. 2.6-2.8 nm. Hence, the calculated crystallite sizes for these catalysts were not reliable.

Only for the MnO-Cu/HSAG and Cr_2O_3-Cu/HSAG catalysts a CuO crystallite size was determined, because for the other two HSAG-suppported catalysts the observed peaks were severely overlapping. As table 3.9 shows a good correlation for the Cr-promoted catalyst was obtained between the calculated CuO crystallite size and d_V, obtained by TEM. However, the diffraction peak was additionally broadened by the fact that four peaks were overlapping, resulting in an underestimation of the mean CuO crystallite size. For the Mn-promoted catalyst the calculated CuO crystallite size appeared to be smaller than the corresponding d_V. This observation might be due to a different shape factor K_{sf}, induced by the presence of a Cu_2O core. To obtain an average copper crystallite size for the Cu/HSAG and ZnO-Cu/HSAG catalysts a Rietveld refinement on the *(111)-(200)* CuO peak at 38.9° could be applied.

Finally, the crystallite sizes of CuO nanoparticles were determined by XRD instead of the catalytically active, metallic copper nanoparticles. As a result, direct comparisons with the mean CuO particle sizes obtained by TEM could be performed. Despite the different densities of CuO and Cu, only small differences between their corresponding Cu nanoparticle/crystallite size would be present. Therefore, no correction was applied for this difference.

3.2.2.5 Temperature-Programmed Reduction

Temperature-programmed reduction under hydrogen (H_2-TPR) was performed, as described in section 2.2.5, to investigate the reduction profile of the as-synthesized catalysts. The reduction temperature of copper oxide is important to know, because copper oxide has to be completely reduced to metallic copper prior to catalysis. Moreover, from the H_2-TPR measurements the copper weight loadings could be obtained for each catalyst.

Figure 3.12 displays the H_2-TPR plots for each as-synthesized catalyst series. From these plots the copper weight loadings are together with the CuO reduction peak positions presented in table 3.10.

In figure 3.12 each H_2-TPR peak at approxmimately 200 °C was attributed to the reduction of CuO, because the reduction temperatures for ZnO, MnO, and Cr_2O_3 were generally higher than 500 °C [61–64]. This statement could be further confirmed by the fact that the obtained copper weight loadings for the CNT- and oxCNT-supported catalysts correlated considerably with their corresponding theoretical copper weight loadings, as depicted in table 3.10.

For the HSAG-supported catalysts all coppper weight loadings were underestimated compared to their theoretical copper weight loadings. This observation was mainly caused by the larger copper nanoparticles compared to the catalysts supported on CNTs and oxCNTs, as these larger particles had a not fully oxidized core. The presence of Cu_2O in these nanoparticles was already confirmed by XRD measurements, as described in section 3.2.2.4, and H_2-TPR/TPO/H_2-TPR experiments, as described in section 3.2.2.1. Indeed, as the stoichiometry of the reduction from Cu_2O to Cu by H_2, depicted in equation (3.4), was different than that for CuO to Cu an underestimation took place. To illustrate, if the copper-based nanoparticles fully consisted of Cu_2O the obtained copper weight loading

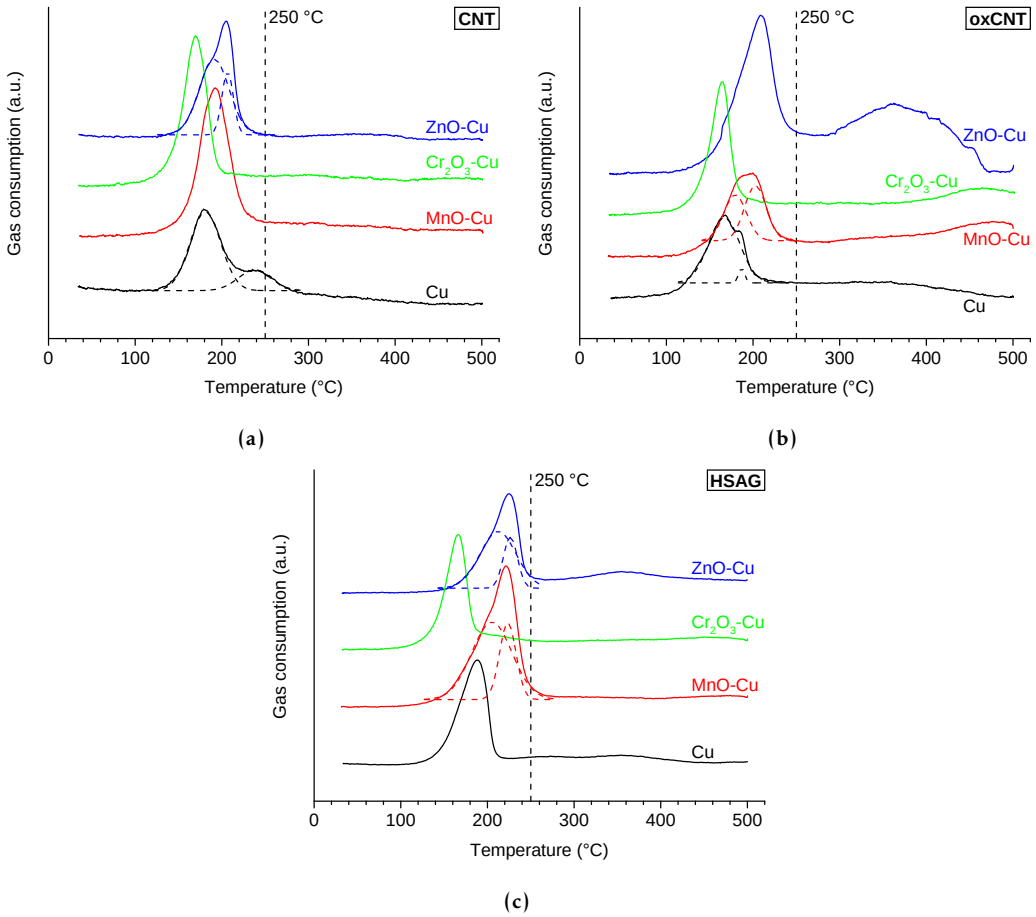

Figure 3.12 H_2-TPR plots for as-synthesized, **a** CNT-, **b** oxCNT-, and **c** HSAG-supported catalysts. All curves within one plot were corrected to the same mass and were corrected from the background signal by subtracting the curve obtained from a corresponding blank impregnated catalyst. All H_2-TPR curves show that the reduction of copper oxide to copper was complete at a reduction temperature of 250 °C, indicated by the vertical dashed lines. The dotted peaks were obtained by a two-peak deconvolution and indicate multiple reduction temperatures were present.

Table 3.10 H_2-TPR results for as-synthesized catalysts. Peaks are also present due to CuO or Cu_2O. **a** Name represents the catalytically active form of the catalyst. **b** Multiple maxima found by a two-peak deconvolution. **c** Number-averaged copper particle diameter, obtained by TEM. **d** Theoretical weight loading, obtained by IWI. **e** Reduction of zinc oxide to metallic zinc.

catalyst[a]		T_{max}[b] (°C)	d_N[c] (nm)	total H_2 uptake ($cm^3 \cdot g_{cat}^{-1}$ at STP)	wt_{Cu} (%)	
support	metal				H_2-TPR	theory[d]
CNT	Cu	181; 238	6 ± 4	11.8	3.3	3.1
	ZnO-Cu	191; 207	6 ± 2	10.4	3.0	3.0
	MnO-Cu	191	5.4 ± 1.9	14.3	4.0	3.0
	Cr_2O_3-Cu	170	5 ± 3	12.3	3.5	3.0
oxCNT	Cu	167; 187	2.1 ± 1.0	11.7	3.5	3.9
	ZnO-Cu	209 (362)[e]	4.2 ± 1.6	18.4	5.4	3.8
	MnO-Cu	180; 203	1.5 ± 0.8	13.2	3.9	3.8
	Cr_2O_3-Cu	164	2.3 ± 1.1	11.9	3.5	3.7
HSAG	Cu	188	12 ± 7	26.7	3.1	8.4
	ZnO-Cu	212; 226	7 ± 6	24.4	2.8	7.9
	MnO-Cu	205; 224	12 ± 18	43.1	5.1	8.0
	Cr_2O_3-Cu	166	6 ± 3	26.2	3.1	7.6

would be exactly twice as large. Moreover, if metallic copper was present in the core of these larger nanoparticles, which was however not the case concerning XRD analysis, then this copper was not tracked, resulting in an even lower copper weight percentage.

$$Cu_2O + H_2 \longrightarrow 2\,Cu + H_2O \tag{3.4}$$

However, for the Cu/HSAG, ZnO-Cu/HSAG, and Cr_2O_3-Cu/HSAG catalysts the copper weight loading was more than a factor 2 higher compared to the theoretical weight loading: 7.6-8.4 wt% vs. 2.8-3.1 wt%. Hence, this difference could not be attributed to only the presence of non-completely oxidized copper species. In addition, from the XRD and TEM analyses, as described in sections 3.2.2.4 and 3.2.2.3, respectively, it appeared that the copper nanoparticles in the Cr_2O_3-Cu/HSAG catalyst were of comparable size of those on oxCNT-supported catalysts, and were therefore completely oxidized. Another explanation for this difference might be that the TCD connected downstream the reactor detected other unknown species than H_2 with a comparable thermal conductivity, although there are only few gases known with similar thermal conductivities as H_2. Finally, the theoretical weight loading of the HSAG-supported catalysts might be different than presented in table 3.10 due to the relatively large BET surface area and total pore volume errors, obtained with N_2 physisorption and displayed in table 3.1. Therefore, inductively coupled plasma mass spectrometry (ICP-MS) experiments have to be performed to obtain the copper and promoter weight loadings more accurately.

The H_2-TPR plots in figure 3.12 demonstrated a good reproducibility between the catalysts promoted with the same metal: for all catalyst series Cr promotion lowered the reduction peak of copper, whereas promotion by Zn and Mn increased the temperature at which the reduction peak of copper occurred. The effect of chromium on the copper oxide reduction temperature was in agreement with Ma *et al.* [44]. These peak shifts could be caused by 1) different copper particle sizes or 2) by a specific promoter effect on the copper species during H_2-TPR, facilitating its reduction to metallic copper. Indeed, both effects were observed. For the as-synthesized catalysts supported on CNTs the copper particle sizes were

comparable to each other (all approximately 6 ± 3 nm, from TEM analysis), and thus the reduction peak shifts were plausibly caused by the specific promoters. This meant that this specific promoter effect must also be present for the other catalyst series. The other effect could be deduced from the Cu/oxCNT, MnO-Cu/oxCNT, and Cr_2O_3-Cu/oxCNT catalysts: their copper oxide reduction peak maximum was shifted a bit downward compared to their CNT-supported counterparts, as depicted in table 3.10. These peak shifts were presumably due to their smaller copper particle size for these catalysts. In addition, the ZnO-Cu/oxCNT and Cr_2O_3-Cu/HSAG catalysts had similar copper partricle sizes, obtained from TEM experiments described in section 3.2.2.3, compared to those for all CNT-supported catalysts and hence their copper reduction peaks appeared to be approximately at the same temperature. Finally, for the Cu/HSAG, ZnO-Cu/HSAG, and MnO-Cu/HSAG catalysts the copper oxide reduction peak was significantly higher compared to the similar catalysts supported on different supports. This peak shift might also be attributed to their considerably larger copper nanoparticle, observed with TEM analysis as described in section 3.2.2.3. All peak shifts caused by differences in copper particle size does not necessarily imply that those smaller particles are thermodynamically more challenging to reduce, but it might also be due to a kinetic effect.

As all catalysts supported on the same carbon support have similar copper weight loadings, as depicted in table 3.10, similar amounts of hydrogen uptake were expected to be found. From the just ascribed acquisition it could hence be concluded that a larger copper oxide particle size on a carbon support led to a H_2-TPR peak with a larger peak area. Similar results were observed by Farahani *et al.* [74]: they reported that larger CuO crystallites need higher reduction temperatures, ascribed to the increase of volume-to-surface ratio, which in turn need higher reduction temperatures.

In addition, another feature which could be observed from the H_2-TPR plots in figure 3.12: most of the copper reduction peaks appeared to consist of multiple reduction peaks. This phenomenon might be attributed to a stepwise oxidation reduction of CuO via Cu_2O towards Cu. Another explanation could be a bimodal copper particle size distribution, in which the larger copper oxide nanoparticles were reduced at higher temperatures compared to the smaller ones, as discussed before. However, from the histograms, obtained during TEM analysis and presented in the appendix in figures E.1, E.2, and E.3, it appeared no such distributions existed.

The most plausible explanation for the occurrence of different reduction peaks per measurement, as depicted in figure 3.12, was reported by Tavasoli, *et al.* [75]. In the case of tube-like carbon supports, as CNTs, the graphene-like structure is bent, which disorders the π-electron density: the concave, inner tube surface becomes depleted of electrons whereas the convex, outer tube surface becomes electron-enriched [76, 77]. The electron-poor, inner tube surface might have led to a stronger copper oxide-support interaction and thereby facilitated the reduction of the copper oxide compared to those on the outer tube surface [75]. Alternatively, the different peaks could be attributed to the copper distribution over the inner and outer tube surface. As this acquisition was not readily applicable to HSAG it could argued that in its amorphous structure microenvironments existed, exhibiting a different amount of concavity and convexity.

At last, an unexpected, broad peak was observed in figure 3.12b for the ZnO-Cu/oxCNT catalyst at approximately 375 °C. This peak might be due to several reasons:

1. reduction of ZnO to Zn by H_2;
2. reduction of ZnO to Zn by carbon from the support;
3. reduction of oxygen-containing groups at the support surface by H_2;
4. detection of species with a similar thermal conductivity as H_2; or

5. malfunction of the H_2-TPR apparatus or contamination the during measurement.

After integration of this peak a corresponding zinc oxide weight loading of 4.9 wt% was calculated. However, the theoretical weight loading of zinc oxide was only 2.6 wt%, as displayed in table 3.3, and moreover this reduction peak was not observed for the similar catalysts supported on CNTs and HSAG. Hence, it would be irrational that this peak at approximately 375 °C was (only) caused by the reduction of zinc oxide. To investigate if the reduction peak could be due to the reduction of oxygen-containing surface groups titrations were performed. This characterization technique is described in detail in section 3.2.2.6. Briefly, as-synthesized ZnO-Cu/oxCNT and Cr_2O_3-Cu/oxCNT catalysts were titrated with acid and base. The obtained support acidities were compared to 1) the acidity of the same catalysts after a post-reduction in a low-pressure, catalytic heat treatment set-up and to 2) the acidity of spent catalysts, obtained after the catalytic tests. The post-reduction procedure is thoroughly described in section 2.1.5. As a result, no significant removal of oxygen-containing surface groups were present. Therefore, the H_2-TPR experiment for the ZnO-Cu/oxCNT catalyst has to be redone.

3.2.2.6 Acid and Base Titrations

To investigate if the reduction peak at 375 °C in the H_2-TPR plot of ZnO-Cu/oxCNT, depicted in figure 3.12b, could be caused by the (partial) reduction of oxygen-containing surface groups of the support, acid and base titrations were carried out for the fresh ZnO-Cu/oxCNT catalyst. As described in section 2.2.2 these titrations were compared with similar titrations of the fresh Cr_2O_3-Cu/oxCNT catalyst, because this catalyst did not show the reduction peak at 375 °C, as depicted in figure 3.12b. To further investigate the amount of surface group reduction the corresponding spent catalysts and catalysts, which underwent a post-reduction, were also titrated. The post-reduction, as described in section 2.1.5, was carried out at 350 °C and further under similar conditions during the corresponding H_2-TPR measurements, as described in section 2.2.5. It was assumed no substantial support degradation of the ZnO-Cu/oxCNT and Cr_2O_3-Cu/oxCNT catalysts was present during the post-reduction up to 350 °C. This assumption was derived from the TGA analyses of the Cu/CNT and Cu/HSAG catalysts under an oxygen atmosphere, depicted in figure 3.6a in section 3.2.2.2, which showed only minor support decomposition at this temperature. In addition, under a hydrogen atmosphere the oxCNT support, shown in figure 3.2b in section 3.1.2.3, was fairly more stable than under an oxygen atmosphere, as depicted in figure 3.2a.

It was expected to observe similar acidic properties for the fresh ZnO-Cu/oxCNT and Cr_2O_3-Cu/oxCNT catalysts, as both catalysts were synthesized on the same acidic support, as derived from table 3.2. Furthermore, no change in the acidic properties was expected upon the post-reduction for the Cr_2O_3-Cu/oxCNT catalyst, because the reduction of copper oxide to metallic copper, which was only present regarding the H_2-TPR plot displayed in figure 3.12b, would not affect the acidity of the support. At the other hand, a lower amount of acidic groups was expected to be present for the ZnO-Cu/oxCNT catalyst after the post-reduction, indicated by the additional reduction peak in the corresponding H_2-TPR plot as displayed in figure 3.12b.

Figure 3.13 depicts the as-described titrations. The mean pK_a values and the amount of acidic and basic groups were retrieved from these titration curves and were presented in tables 3.11 and 3.12, respectively.

From the acid titrations, depicted in figure 3.13 it could be observed that the blank impregnated oxCNTs were significantly less acidic than the bare oxCNT support, derived from the fact that the equivalence point was reached with a lower amount of base titrant. Indeed, from table 3.11 it could be noticed that the acidic group concentration declined from

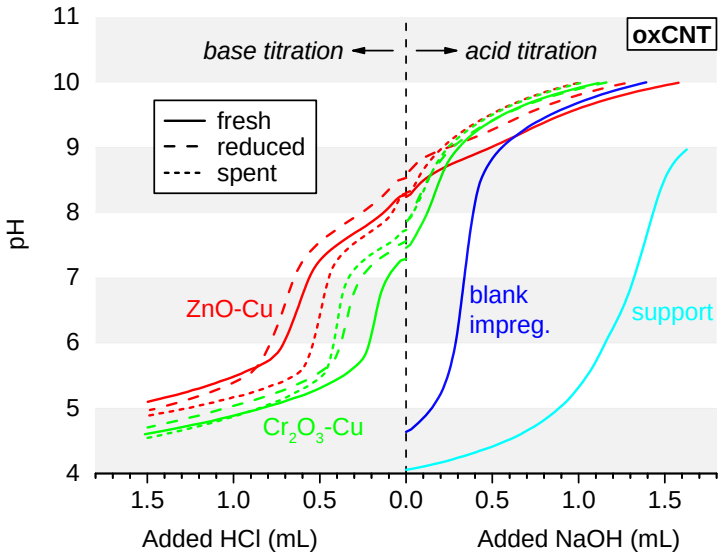

Figure 3.13 Acid and base titration curves of ZnO-Cu/oxCNT and Cr_2O_3-Cu/oxCNT catalysts compared to the blank impregnated oxCNTs and bare oxCNT supports. Fresh means as-synthesized (underwent a direct reduction up to 230 °C under 20 vol% H_2/N_2 flow); reduced catalysts were fresh catalysts, which underwent a post-heat treatment up to 350 °C under 5 vol% H_2/H_2 flow; spent means catalysts after *in situ* reduction up to 250 °C under 20 vol% H_2/Ar flow and subsequent 250 h of catalysis (40 bar of syngas flow, consisting of Ar:CO_2:CO:H_2 = 10:7:23:60 vol%). The acid titration curve of the blank impregnated oxCNTs indicated that after the reduction during catalyst synthesis the amount of acidic groups was signficantly lowered. The addition of metals probably screened the acidic groups, leading to neutral/basic supports. Barely any differences between the reduction procedures were observed.

548 to 145 $\mu mol \cdot g_{sup}^{-1}$. This result could be due to the fact that during the direct reduction in the catalyst preparation not only the metal species were affected, but also a part of the oxygen-containing groups on the oxCNT support surface.

With the introduction of metal species on the oxCNT support, the support acidity of the ZnO-Cu/oxCNT and Cr_2O_3-Cu/oxCNT catalysts turned out to be even less than that of the blank impregnated oxCNTs: it even became slightly basic, as could be observed by the presence of equivalence points in the base titration curves. These observations could be due to

Table 3.11 Acid titration results for the as-synthesized or fresh (F), reduced (R) and spent (S) ZnO-Cu/oxCNT and Cr_2O_3-Cu/oxCNT catalysts. For comparison the blank impregnated oxCNTs and bare support were also acid titrated. For ZnO-Cu/oxCNT-S no equivalence point was found.

catalyst	**equivalence point (–)**	**mean pK_a (–)**	**acidic group concentration**	
			$\mu mol \cdot g_{sup}^{-1}$	nm^{-2}
ZnO-Cu/oxCNT-F	9.2	8.8	280	0.66
ZnO-Cu/oxCNT-R	9.4	9.1	252	0.60
Cr_2O_3-Cu/oxCNT-F	8.3	7.8	74	0.18
Cr_2O_3-Cu/oxCNT-R	8.0	7.9	15	0.04
Cr_2O_3-Cu/oxCNT-S	8.4	8.1	45	0.11
oxCNT blank	7.0	5.1	145	0.34
oxCNT support	7.8	4.7	548	1.30

Table 3.12 Base titration results for the as-synthesized or fresh (F), reduced (R) and spent (S) ZnO-Cu/oxCNT and Cr_2O_3-Cu/oxCNT catalysts. For Zn-promoted catalysts two equivalence points were found. **a** pK_a value calculated from corresponding pK_b values.

catalyst	**equivalence point (–)**	**mean pK_a**[a] **(–)**	**basic group concentration**	
			$\mu mol \cdot g_{sup}^{-1}$	nm^{-2}
ZnO-Cu/oxCNT-F	6.6	6.4	261	0.62
	8.3	5.7	7	0.02
ZnO-Cu/oxCNT-R	6.6	6.2	301	0.71
	8.5	5.5	25	0.06
ZnO-Cu/oxCNT-S	6.4	6.4	203	0.48
	8.3	5.7	5	0.01
Cr_2O_3-Cu/oxCNT-F	6.4	6.9	75	0.18
Cr_2O_3-Cu/oxCNT-R	6.3	6.7	153	0.36
Cr_2O_3-Cu/oxCNT-S	6.3	6.6	171	0.41

the fact that 1) electropositive metal species adsorbed reasonably more strongly onto the electronegative, oxygen-containing surface groups than onto the non-polar carbon support, thereby screening the acidic groups during the titrations, or to the fact that 2) the metal species promoted the reduction of acidic groups compared to the blank impregnated oxCNTs. Furthermore, the shift from an acidic support to a basic support could be attributed to the higher instability of acidic groups compared to basic groups [78].

However, the full screening of all acidic groups by metal species was not the most plausible explanation for the lowered acidity of the fresh catalysts compared to the blank impregnated oxCNTs. For the oxCNT-supported catalyst series a theoretical copper and promoter surface loading of, respectively, 1.50 and $0.81\,nm^{-2}$ was present, which could be derived from table 3.3. For the calculation of these surface loadings it was assumed that all metal species were homogeneously distributed as individual atoms on the support surface. The assumption for a homogeneous distribution of the copper and promoter species was indeed correct, as this distribution was observed in the fresh MnO-Cu/oxCNT and Cr_2O_3-Cu/oxCNT catalysts, determined with HAADF-STEM-EDX analysis shown in figures 3.16a and 3.17a. However, nanoparticles were formed during the catalyst synthesis leading to an effective lowering in the metal surface loading. To illustrate, for the ZnO-Cu/oxCNT and Cr_2O_3-Cu/oxCNT catalysts mean copper particle sizes of 4.2 and 2.3 nm, obtained by TEM described in section 3.2.2.3, resulted in an effective copper surface loading of approximately 0.001 and $0.01\,nm^{-2}$, respectively. In addition, if the mean promoter size on these catalysts was assumed to be approximately 1 nm, as the nanoparticles were not observable with TEM and XRD analysis described in section 3.2.2.3 and 3.2.2.4, respectively, the corresponding surface loading was effectively lowered from $0.81\,nm^{-2}$ to approximately $0.1\,nm^{-2}$. Hence, the total effective surface loading (approximately $0.1\,nm^{-2}$) was governed by the promoter oxide nanoparticles. However, this metal surface loading was not sufficient enough to fully cover all acidic groups present after the direct reduction during catalyst preparation: $0.34\,nm^{-2}$, depicted in table 3.11. Therefore, some acidity was still expected to be tracked by the acid titrations of the as-synthesized ZnO-Cu/oxCNT and Cr_2O_3-Cu/oxCNT catalysts.

Surprisingly, the total amount of acidic and basic groups for both fresh catalysts was higher than that amount on the blank impregnated oxCNT support ($145\,\mu mol \cdot g_{sup}^{-1}$), even after the reasonable coverage of oxygen-containing groups by the metal species. Therefore, upon metal addition to the supports the supports appeared to become more acidic/basic. Alternatively, it

seemed that the addition of metals created additional acidic and basic groups on the support surface. This unexpected result could yet not be explained and further research has to be applied.

Next, a clear difference existed between the base titration curve of the fresh ZnO-Cu/oxCNT catalyst compared to that of the Cr-promoted catalyst: the first-mentioned was considerably more basic than the second-mentioned. This observation might be attributed to the above-ascribed effect of nanoparticle size: the mean copper particle size was significantly larger for the ZnO-Cu/oxCNT catalyst than for the Cr_2O_3-Cu/oxCNT catalyst, leading to a lowering of the effective surface loading. Furthermore, a slight difference in the mean nanoparticle size of the corresponding promoters, which could not be determined with any technique used in this thesis, could significantly alter the effective surface loading of the promoter species. Hence, the screening of the acidic surface groups by metal species was less efficient for the ZnO-Cu/oxCNT catalyst compared to the Cr_2O_3-Cu/oxCNT catalyst and as a result more surface groups were revealed during the titrations. The difference in apparent acidic properties between the titrated fresh catalysts could not originate from the different redox behaviors of zinc oxide and chromium oxide. Indeed, from the corresponding Pourbaix diagrams, calculated with HSC Chemistry v7.14 [15], no redox reactions within the stability area of water were plausible to occur.

After the post-reduction of the ZnO-Cu/oxCNT and Cr_2O_3-Cu/oxCNT catalysts and after catalysis barely any changes in the titration curves were observed compared to the titration curves of their corresponding fresh catalysts, as depicted in figure 3.13. For the Cr-promoted catalyst these observations were predicted, but not for the Zn-promoted one. During the reductions at an elevated temperature it was expected that metal species were removed from their oxygen-containing surface groups, thereby exposing the surface groups, and hence making them more prone to reduction. As the enhanced acidic group reduction was not observed from the titration curves it would suggest that the surprising peak at 375 °C in the H_2-TPR of the ZnO-Cu/oxCNT catalyst, displayed in figure 3.12b, was not caused by the reduction of the surface groups. To furthermore check if no enhanced acidic group reduction was present for the ZnO-Cu/oxCNT and Cr_2O_3-Cu/oxCNT catalysts TGA-MS analysis of these catalysts under an hydrogen flow might be applied.

3.3 Stability Tests

To investigate the stability of the copper catalysts, characterized in section 3.2, catalytic testing under industrial conditions was performed, as described in section 2.3. From the bachelor's thesis of Van der Wal [47] it appeared that the non-promoted, CNT-supported copper catalyst was too unstable under catalytic conditions and hence this catalyst not active towards the production of methanol. This particular instability was due to the relatively smooth surface of the CNTs and the lack of anchoring sites, which had led to a fast growth of the copper nanoparticles during catalysis. For that reason, stability tests were only performed for the oxCNT- and HSAG-supported catalysts. As the equilibrium CO + CO_2 conversion at 260 °C and 40 bar is 32.1 %, as depicted in figure 1.1a, catalytic testings were aimed to be performed below this value to avoid the backwards reaction from methanol to syngas.

3.3.1 oxCNT-Supported Catalyst Series

In figure 3.14a the stability curves for the oxCNT-supported catalysts are shown, which were normalized to the corresponding maximum CO + CO_2 conversion. From this figure it could be observed that all tested catalysts partially deactivated within a long-term, catalytic test of 250 h. Furthermore, figure 3.14b displays equivalent stability curves, which were relative to the initially most active catalyst. More specifically, this catalyst exhibited the highest conversion of CO + CO_2 per amount of catalyst per time under a constant gas hourly space

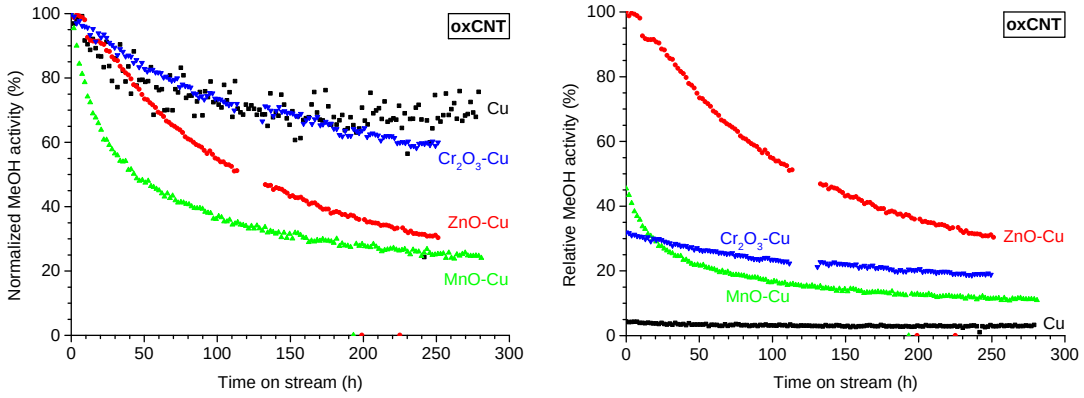

(a) Normalized activity (NA)

(b) Relative activity (RA)

Figure 3.14 Stability curves of the oxCNT-supported catalysts. From curves (**a**, **b**) it could be observed that all catalysts deactivate. From plot **a** the zinc- and especially the manganese-promoted catalysts deactivate rapidly, whereas addition of Cr resulted in a relative stable catalyst. From plot **b** all promoters enhanced the CO + CO_2 conversion with zinc the most effective. Time-on-stream t was set at 0 when the production of methanol was maximum. No methanol was produced during the catalytic test of the blank impregnated CNTs.

velocity (GHSV) for this catalyst series. As could be observed from figure 3.14b the ZnO-Cu/oxCNT catalyst was this most active catalyst, exhibiting an activity towards methanol of approximately 28 times more than for the non-promoted catalyst. In addition, upon manganese and chromium promotion the CO + CO_2 conversion was enhanced compared to the non-promoted catalyst. This and other important stability test-related results were summarized in table 3.13.

Figure 3.14a shows that the addition of promoters had a significant effect on the stability profile of the catalysts. Indeed, the Mn-promoted catalyst deactivated rapidly once the maximum methanol production was reached, whereas after approximately 80 h the decrease in methanol activity was diminished. When ZnO was added to the copper catalyst the initial stability was higher compared to the MnO-Cu/oxCNT catalyst, but deactivated more steadily after approximately 80 h. Upon Cr promotion a significantly different effect was observed: the stability stayed during the full catalytic testing range considerably higher compared to the Zn- and Mn-promoted catalysts.

For the non-promoted catalyst a significant uncertainty within its stability curve could be observed, which was in agreement with the data reported by Van der Wal [47]. This scattering was also reflected in the corresponding selectivity curve, as depicted in the appendix in figure C.1a. This observation could be attributed to the low CO + CO_2 conversion (0.8 %), resulting in a low methanol synthesis activity ($0.2\,\mathrm{mol_{CO+CO_2}} \cdot \mathrm{kg_{cat}^{-1}} \cdot \mathrm{h^{-1}}$). To justify this explanation a comparison of the stability curve of the Cu/oxCNT catalyst (figure 3.14a) with the stability curve of the HSAG-supported counterpart (figure 3.18a) is presented in figure 3.20a. From this comparison it was clear that the higher initial CO + CO_2 conversion for the Cu/HSAG catalyst (1.7 %) led to a diminished scattering. From figure 3.14a it also appeared that the Cu/oxCNT catalyst was the most stable oxCNT-supported catalyst after the stability run had been finished: 68 % of its initial activity was still present. This surprisingly high stability of the Cu/oxCNT catalyst might be due to initial copper particle growth prior to $t = t_0$ was reached. Alternatively, the copper particles grew significantly before the catalytic conditions were reached and the first data point was obtained. The reason for this prior copper particle growth might be related to the lack of the stability-enhancing properties of the added promoters: the addition of Zn, Mn, and Cr stabilized the corresponding copper catalysts at least structurally. In contrast, for the stability curve reported by Van der Wal [47] only 50 % of the initial activity after catalysis was found, which would suggest less prior

Table 3.13 Important stability-related parameters for the oxCNT-supported catalysts at maximum methanol production ($t = t_0$) and after catalysis ($t = 250\,\mathrm{h}$). t = time-on-stream; χ = conversion; z = catalyst mass-based activity; CTY = copper time yield; S = selectivity; TOF = turn over frequency; d_S = surface-averaged particle diameter from TEM; NA = normalized activity (percentage with respect to the original activity); $m_{\mathrm{cat,react}}$ = mass of copper catalyst loaded into the reactor; wt = weight loading. **a** Large, unknown uncertainties due too high scattering. **b** Obtained after full catalytic test: for Cu/oxCNT and Cr_2O_3-Cu/oxCNT catalysts, after 280 h. **c** Weight percentage of promoter oxide as depicted in the corresponding catalyst name.

parameter at $t = t_0$	**oxCNT support**			
	Cu[a]	ZnO-Cu	MnO-Cu	Cr_2O_3-Cu
χ_{CO+CO_2} (%)	0.8	15.6	7.1	5.0
z_{CO+CO_2} ($mol_{CO+CO_2} \cdot kg_{cat}^{-1} \cdot h^{-1}$)	0.2	5.6	2.5	1.8
CTY ($\mu mol_{CO+CO_2} \cdot g_{Cu}^{-1} \cdot s^{-1}$)	1.8	41.5	18.8	13.5
S_{MeOH} (%)	76	99	94	94
TOF ($10^{-3} \cdot s^{-1}$)	0.28 ± 0.13	11 ± 4	2.0 ± 1.1	2.1 ± 1.0
d_S (nm)	2.3 ± 1.0	4.5 ± 1.7	1.7 ± 1.0	2.5 ± 1.2
parameter at $t = 250\,\mathrm{h}$				
NA (%)	68	30.4	25.3	60.0
χ_{CO+CO_2} (%)	0.9	4.3	5.7	2.2
z_{CO+CO_2} ($mol_{CO+CO_2} \cdot kg_{cat}^{-1} \cdot h^{-1}$)	0.3	1.5	2.0	0.8
CTY ($\mu mol_{CO+CO_2} \cdot g_{Cu}^{-1} \cdot s^{-1}$)	2.0	11.5	15.2	5.8
S_{MeOH} (%)	70	97	82	92
TOF ($10^{-3} \cdot s^{-1}$)[b]	0.7 ± 0.2	3.6 ± 1.1	5 ± 2	1.8 ± 0.7
d_S (nm)[b]	6.1 ± 1.8	5.2 ± 1.6	6 ± 2	5.0 ± 1.8
constant parameter				
$m_{\mathrm{cat,react}}$ (mg)	451	400	401	400
wt_{Cu} (wt%)	3.9	3.8	3.8	3.7
wt_{prom} (wt%)[c]	–	2.6	2.3	4.8

copper particle growth was present. To investigate if prior copper particle growth was indeed present for the non-promoted catalyst a stability test of this catalyst has to be performed for only several hours. After this short catalytic test the copper particle size has to be determined by TEM analysis to check if the copper nanoparticles grew substantially.

The stability curves were also visualized relatively to each other on an activity-basis, as depicted in figure 3.14b. As already mentioned in the beginning of this section it appeared that the ZnO-Cu/oxCNT catalyst had the highest initial methanol activity, despite of its larger, initial surface-averaged copper particle diameter ($4.5 \pm 1.7\,\mathrm{nm}$) compared to the other catalysts within this series, as presented in table 3.13. To remind, the decay in methanol production under catalytic conditions was due to copper particle growth and/or loss of promoter effects. Therefore, the addition of Zn must have a chemically promoting effect on the initial activity. The promoting effect of Zn was also proven multiple times in literature [9, 19, 25, 79]. In addition, the Mn and Cr promotion had an promoter effect on the initial activity towards methanol, although it was less pronounced compared to the promoter effect of Zn. These promoting effects were reflected by the initial turn over frequencies (TOFs), as depicted in table 3.13.

Furthermore, a discontinuity in the stability curves, depicted in figure 3.14, was observed for the ZnO-Cu/oxCNT and Cr_2O_3-Cu/oxCNT catalysts. This dissimilarity was due to a malfunction between the gas chromatograph (GC) and the parallel stability reactors. From the stability curves itself it appeared it had no impact on the relative methanol production. However, when the catalyst mass-based activity z_{CO+CO_2} of the MnO-Cu/oxCNT and Cr_2O_3-Cu/oxCNT catalysts were plotted against the time-on-stream t an unexpected behavior was observed, as shown in figure 3.15a.

From the activity curves, presented in figure 3.15a, it appeared that for the Cr-promoted catalyst a sudden decrease in the catalyst mass-based activity occurred after the GC malfunction. Assumed that the gas feed composition and the gas flow in the reactor were constant during catalytic testing, this decrease must be caused by an abruptly lower CO + CO_2 conversion. This unexpected behavior was not observed for the stability curves, depicted in figure 3.14, because they were based on calculations of the GC peak area of methanol. The reason why the CO + CO_2 conversion dropped that significantly is not known.

Furthermore, for the Mn-promoted catalyst the trend of the catalyst mass-based activity z_{CO+CO_2}, depicted in figure 3.15a, was as expected for the first 80 h: an activity decrease due to a lowering in the amount of copper surface area present in the loaded catalyst, induced by copper particle growth. Surprisingly, from 80 h onward the activity was enhanced again. This increase must be due to an increase in CO + CO_2 conversion, which in turn might suggest that the mean surface-averaged copper particle size was decreasing. This was however highly implausible to occur. Another explanation for the increased CO + CO_2 conversion was derived from the methanol selectivity trend plotted against the time-on-stream t, displayed in figure 3.15b. Indeed, in this figure a product selectivity change was occurring: from 80 h of catalytic testing onward the production of Fischer-Tropsch-like products, represented as the C5+ fraction, increased whereas the methanol selectivity started to decrease. However, after 250 h of catalysis the selectivity towards methanol was still significantly higher (82 %) compared to the selectivity of the C5+ fraction (11 %). This would imply that the MnO-Cu/oxCNT catalyst increased the consumption of CO and CO_2 after 80 h of catalysis to synthesize Fischer-Tropsch-like products more actively compared to the methanol synthesis.

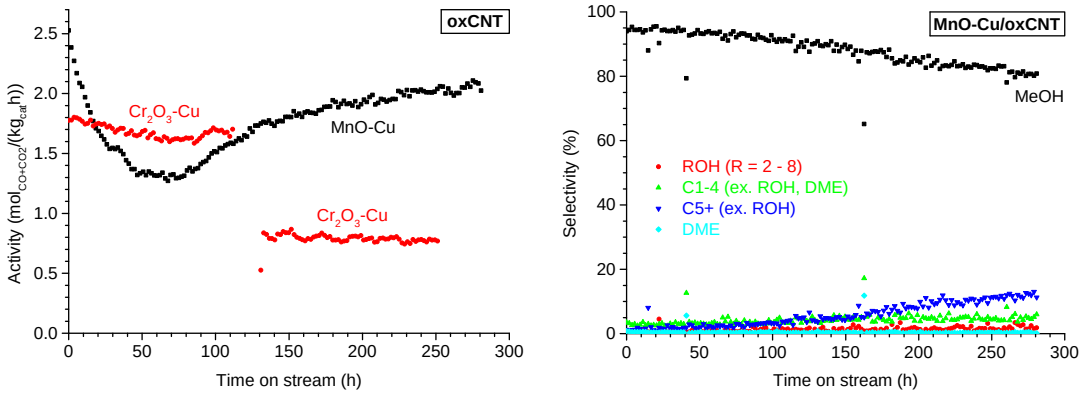

(a) Catalyst mass-based activity (z_{CO+CO_2}) **(b)** Product selectivity (S)

Figure 3.15 a Catalyst mass-based activity curves of the MnO-Cu/oxCNT and Cr_2O_3-Cu/oxCNT catalysts during catalytic testing. **b** Product selectivity curves of the MnO-Cu/oxCNT catalyst. ROH = primary, linear alcohol; DME = dimethyl ether. The activity curve of MnO-Cu/oxCNT **a** increased from approximately 80 h onwards due to the formation of Fischer-Tropsch-like products (C5+ (ex. ROH)), as derived from its corresponding selectivity curve **b**. The activity of the Cr_2O_3-Cu/oxCNT catalyst **a** showed a sudden drop after the GC malfunction.

The reason for the increase of the C5+ selectivity of the MnO-Cu/oxCNT catalyst, depicted in figure 3.15b, could be ascribed to the presence of the cobalt growth catalyst. Cobalt is well-known for long-chain hydrocarbon production and its specific selectivity is even enhanced with the addition of manganese [80–82]. As most probably the weight loading of the growth catalyst was low, it was per amount of catalyst not active enough to produce Fischer-Tropsch-like products for the other oxCNT-supported catalysts. The presence of the growth catalyst was proven for the MnO-Cu/oxCNT catalyst by the HAADF-STEM-EDX technique, as previously presented in figures 3.8b-c in section 3.2.2.3. The cobalt nanoparticles were plausibly accessible for the syngas molecules in the gas feed as also a significant part of the copper nanoparticles were deposited inside the oxCNTs. An induction period of approximately 80 h was apparently needed to diffuse the manganese oxide and cobalt particles over the oxCNT surface to form the Fischer-Tropsch-active CoMnO nanoparticles. This induction period might be due to the presence of oxygen-containing surface groups, retarding the diffusion of metal species. To make this reasoning plausible an ICP-MS characterization on the CNT- or oxCNT-supported catalysts has to be performed to obtain the cobalt weight loading.

Another assumptions made in the above acquisition was that 1) prior to catalysis the manganese particles were apart from the cobalt particles and 2) that the manganese particles were in close contact with the copper nanoparticles, which resulted in the enhanced initial activity towards methanol. At the other hand, during the catalytic tests the manganese oxide and cobalt nanoparticles diffused towards each other. This assumption could be proven by HAADF-STEM-EDX images between the as-synthesized and spent MnO-Cu/oxCNT catalysts, as displayed in figure 3.16. Indeed, in the as-synthesized catalyst (figure 3.16a) the manganese oxide and copper species were both homogeneously and finely distributed over

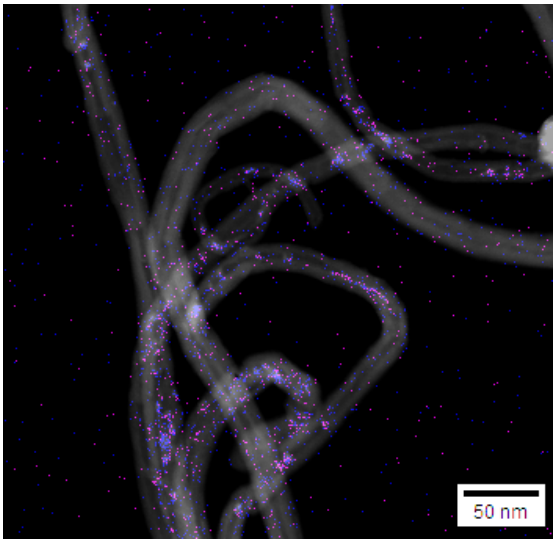

(a) MnO-Cu/oxCNT fresh

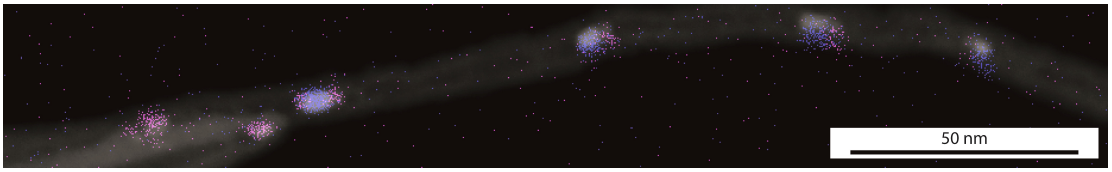

(b) MnO-Cu/oxCNT spent

Figure 3.16 HAADF-STEM-EDX images of MnO-Cu/oxCNT catalysts. Cu = dark blue; Mn = magenta. In the as-synthesized or fresh catalyst **a** a homogeneous distribution of very small manganese oxide and to some extent larger copper nanoparticles was observed. In the spent catalyst **b** clustering of copper and manganese was observed.

the oxCNT support, but partly clustered after 250 h of catalysis (figure 3.16b). Moreover, small copper nanoparticles could be discriminated from figure 3.16a. These observations were in line with the TEM and XRD results, as described in sections 3.2.2.3 and 3.2.2.4, respectively: no diffraction peaks for manganese were observed by XRD and a small mean copper particle size (1.5 ± 0.8 nm) was obtained by TEM.

In the spent MnO-Cu/oxCNT catalyst, depicted in figure 3.16b, larger copper nanoparticles were observed and most of the manganese oxide was still in close contact with the copper species. The manganese oxide was not homogeneously distributed over the copper particles, but clustered sideways to them. Therefore, the amount of intimate contact between the copper and manganese species might be lower compared to the as-synthesized catalyst. To confirm this an extended X-ray absorption fine structure (EXAFS) could be obtained with X-ray absorption spectroscopy (XAS) to determine the local environment of the copper and manganese atoms. In addition, some isolated manganese oxide particles were observed. The promoting effect of manganese to the copper catalyst was for that reason also lowered. Finally, as metal-metal interactions are energetically more favored than metal-carbon interactions, as already mentioned in section 1.4.2, the diffusion of the detected, isolated manganese and cobalt species over the support surface towards each other might be facile.

The redistribution of the chromium species between the as-synthesized and spent Cr_2O_3-Cu/oxCNT catalysts was also visualized with HAADF-STEM-EDX. In figure 3.17 the corresponding images were depicted. For the as-synthesized catalyst, depicted in figure 3.17a, a similar particle distribution over the support surface compared to the as-synthesized

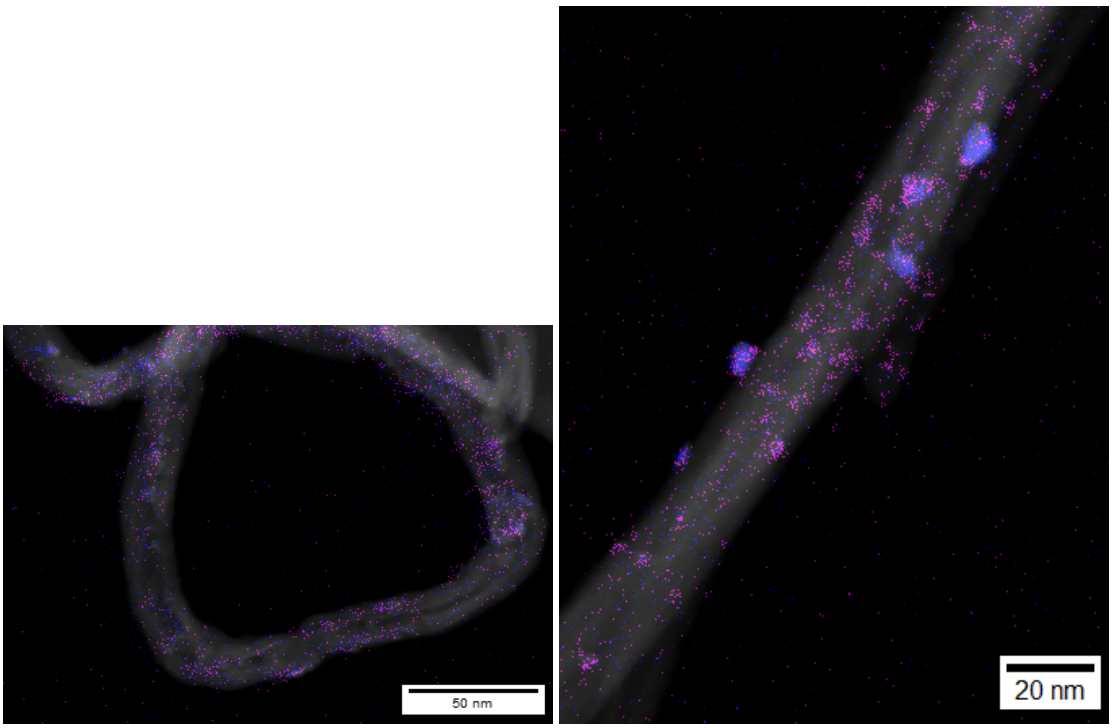

(a) Cr_2O_3-Cu/oxCNT fresh **(b)** Cr_2O_3-Cu/oxCNT spent

Figure 3.17 HAADF-STEM-EDX images Cr_2O_3-Cu/oxCNT catalysts. Cu = dark blue; Cr = magenta. In the as-synthesized or fresh catalyst **a** a homogeneous distribution of very small chromium oxide and to some extent larger copper nanoparticles was observed. In the spent catalyst **b** clustering of copper and chromium was observed.

MnO-Cu/oxCNT was observed: a homogeneous, fine distribution of chromium species and the presence of small copper nanoparticles (2.3 ± 1.1 nm). Again, this was in line with the XRD and TEM analyses, as described in section 3.2.2.3 and 3.2.2.4.

For the HAADF-STEM-EDX characterization of the spent Cr-promoted catalyst, depicted in figure 3.17b, the copper particles were clearly grown during the 250 h of catalysis. For the chromium promoter this particle growth was much less pronounced compared to the manganese promoter: only small chromium clusters were observed in the HAADF-STEM-EDX images and they were also relatively homogeneously distributed. In addition, near the copper particles chromium species were observed. However, from this 2D technique it could not be distinguished if the chromium oxide was covering the copper nanoparticles or a bimetallic phase was formed. Nevertheless, compared to the spent MnO-Cu/oxCNT catalyst the chromium species did not grow significantly and the coverage of copper species by chromium oxide was still preserved. Alternatively, a larger contact area between the chromium and copper species was obtained compared to the intimacy between manganese and copper, as depicted in figure 3.16b. Moreover, table 3.13 shows that for the Cr_2O_3-Cu/oxCNT catalyst 60.0 % of the initial methanol productivity was preserved after 250 h of catalysis, whereas for the MnO-Cu/oxCNT catalyst only 25.3 % was left. Therefore, it was plausible that the promoter effect of chromium on the copper catalyst was better preserved compared to the manganese promoter.

3.3.2 HSAG-Supported Catalyst Series

The stability tests were also performed for the HSAG-supported catalysts of which the synthesis was described in sections 2.1.3 and 2.1.4 and their characterization in section 3.2. In figure 3.18 the stability curves for the HSAG-supported catalysts were displayed in two different ways. From these stability curves it could be derived that all catalysts partially deactivated during catalysis. Furthermore, from figure 3.18b it appeared that upon Zn promotion the initial catalyst activity towards methanol was increased most efficiently. Both sets of curves were obtained in the same way as described in sections 3.3.1 and 2.3. Important stability test-related parameters were presented in table 3.14.

More specifically, from figure 3.18a similar stability trends could be discerned as for the oxCNT-supported counterparts: 1) upon Mn promotion a high initial catalytic instability was observed, but the stability decay was significantly less after a prolonged time of catalytic testing, 2) a steady deactivation of the Zn-promoted copper catalyst was observed, but after 250 h of catalytic testing it almost became less stable compared to the MnO-Cu/HSAG catalyst, and 3) a high, long-term stability of the Cr_2O_3-Cu/HSAG catalyst over the full catalytic testing range was observed. However, the Cu/HSAG catalyst had a considerably lower signal-to-noise level compared to the Cu/oxCNT catalyst, resembling a previously reported stability curve by Van der Wal [47]. This lower amount of scattering was due to the fact that the initial CO + CO_2 conversion χ_{CO+CO_2} (and hence the catalyst mass-based activity z_{CO+CO_2}) was significantly higher: 1.7 vs. 0.8 %, respectively. In addition, the Cu/HSAG catalyst seemed to deactivate faster than its oxCNT-supported counterpart, as depicted in figure 3.20a. As already described in section 3.3.1 this observation was probably due to the initial copper particle growth of the Cu/oxCNT catalyst. Indeed, the pre-deactivation was not present or was less severe for the Cu/HSAG catalyst, indicated by the almost six times larger, initial surface-averaged copper particle size of the Cu/HSAG catalyst (13 ± 8 nm vs. 2.3 ± 1.0 nm). This difference in particle size might have led to a lower prior particle growth rate for the Cu/HSAG catalyst. In addition, the (initial) turn over frequency (TOF) of the Cu/HSAG catalyst was approximately 5 times higher than for the Cu/oxCNT catalyst, implying less severe initial particle growth was present.

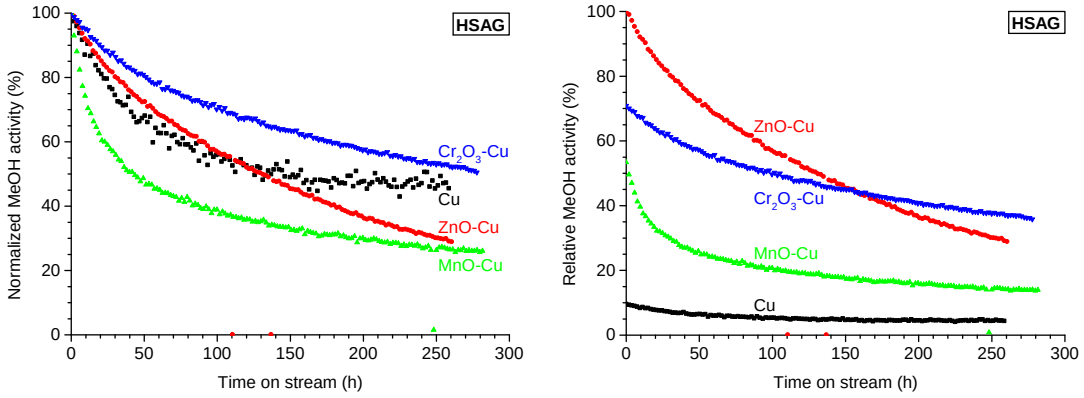

(a) Normalized activity (NA) **(b)** Relative activity (RA)

Figure 3.18 Stability curves of the HSAG-supported catalysts. From curves (**a**, **b**) it could be observed that all catalysts deactivate. Time-on-stream t was set at 0 when the methanol production was maximum. From plot **a** the non-, zinc-, and especially the manganese-promoted catalysts deactivated rapidly, whereas Cr addition resulted in a relatively stable catalyst. From plot **b** all promoters enhanced the initial CO + CO_2 conversion, zinc being the most effective. However, after catalysis the Cr_2O_3-Cu/HSAG catalyst was most stable, due to its diminished particle growth.

Table 3.14 Important stability-related parameters for the HSAG-supported catalysts at maximum methanol production ($t = t_0$) and after catalysis ($t = 250$ h). t = time-on-stream; χ = conversion; z = catalyst mass-based activity; CTY = copper time yield; S = selectivity; TOF = turn over frequency; d_S = surface-averaged particle diameter from TEM; NA = normalized activity left of original activity; $m_{cat,react}$ = mass of copper catalyst loaded into the reactor; wt = weight loading. **a** Obtained after full catalytic test: for MnO-Cu/HSAG and Cr_2O_3-Cu/HSAG catalysts after 280 h. **b** Weight percentage of promoter oxide as depicted in the corresponding catalyst name.

parameter at $t = t_0$	**HSAG support**			
	Cu	ZnO-Cu	MnO-Cu	Cr_2O_3-Cu
χ_{CO+CO_2} (%)	1.7	15.8	8.5	11.2
z_{CO+CO_2} ($mol_{CO+CO_2} \cdot kg_{cat}^{-1} \cdot h^{-1}$)	0.5	5.7	3.0	4.0
CTY ($\mu mol_{CO+CO_2} \cdot g_{Cu}^{-1} \cdot s^{-1}$)	1.8	20.4	10.7	15.0
S_{MeOH} (%)	89	99	97	96
TOF ($10^{-3} \cdot s^{-1}$)	1.5 ± 0.9	11 ± 9	13 ± 20	6 ± 3
d_S (nm)	13 ± 8	9 ± 7	21 ± 31	7 ± 3
parameter at $t = 250$ h				
NA (%)	46.5	30.1	26.3	53.4
χ_{CO+CO_2} (%)	1.1	7.5	2.3	7.1
z_{CO+CO_2} ($mol_{CO+CO_2} \cdot kg_{cat}^{-1} \cdot h^{-1}$)	0.3	2.7	0.8	2.5
CTY ($\mu mol_{CO+CO_2} \cdot g_{Cu}^{-1} \cdot s^{-1}$)	1.2	9.7	2.9	9.5
S_{MeOH} (%)	76	95	92	94
TOF ($10^{-3} \cdot s^{-1}$)[a]	1.0 ± 0.8	6 ± 3	3 ± 4	4.0 ± 1.4
d_S (nm)[a]	14 ± 11	11 ± 5	17 ± 25	7 ± 3
constant parameter				
$m_{cat,react}$ (mg)	452	400	400	400
wt_{Cu} (wt%)	8.4	7.9	8.0	7.6
wt_{prom} (wt%)[b]	–	5.5	4.8	9.7

From figure 3.18a it was already mentioned that upon chromium addition the catalytic stability was enhanced compared to the Cu/HSAG catalyst. Therefore, the addition of chromium to the copper catalyst stabilized the catalytic methanol production and chromium could therefore be regarded as a structural promoter. Furthermore, Cr promotion simultaneously enhanced the initial activity towards methanol, as displayed in figure 3.18b.

From the relative methanol activity curves, shown in figure 3.18b, the Zn-promoted catalyst was initially the most active catalyst. This observation was in accordance with the results obtained in section 3.3.1. However, after 250 h of catalysis the Cr_2O_3-Cu/HSAG catalyst was the most active catalyst. This observation might be explained by the fact that the initial surface-averaged copper particle size of the Cr-promoted catalyst was significantly smaller after catalysis than the one of the spent ZnO-Cu/HSAG catalyst: 7 ± 3 vs. 11 ± 5 nm. The Cr-promoted catalyst had for that reason a larger copper surface area, leading to a higher production of methanol. This result was also reflected in a larger copper time yield (CTY), catalyst mass-based activity z_{CO+CO_2}, and CO + CO_2 conversion χ_{CO+CO_2} of the Cr_2O_3-Cu/HSAG catalyst relative to the Zn-promoted, HSAG-supported catalyst. Furthermore, the copper nanoparticles of the Cr_2O_3-Cu/HSAG catalyst barely grew with respect to the ones of the Zn-promoted catalyst, as could be derived from table 3.14. This trend was, as already mentioned, reflected in the high stability of the Cr-promoted catalysts, both supported on oxCNTs and HSAG as depicted in figure 3.20d. Therefore, chromium acted as a good structural promoter for the copper-based, carbon-supported catalysts for methanol synthesis. However, the main drawback of using chromium as promoter is the high toxicity, especially on industrial scale [83, 84].

3.3.3 Particle and Crystallite Size Analysis of Spent Catalysts

During 250 h of catalysis the oxCNT- and HSAG-supported catalysts deactivated, as depicted in figures 3.14 and 3.18. This deactivation could be caused by three reasons: 1) the copper nanoparticles on the catalyst surfaces grew, resulting in a lower amount of catalytically active copper surface area, 2) the catalyst became less selective towards methanol, and 3) the promoter effect was lost for the promoted catalysts.

The copper particle growth was investigated for each tested catalyst with transmission electron microscopy (TEM), as described in section 3.3.3.1, and X-ray diffraction (XRD) measurements, as described in section 3.3.3.2. Moreover, for the MnO-Cu/oxCNT and Cr_2O_3-Cu/oxCNT catalysts this was also investigated with electron-dispersive X-ray chemical mapping, accompanied with high-angle, annular, dark-field, scanning-tranmission electron microscopy (HAADF-STEM-EDX), depicted in figures 3.16 and 3.17. Section 3.3.3.3 describes the turn over frequencies (TOFs), from which promoter effect losses could be derived.

3.3.3.1 Particle Size Analysis

Comparisons between the copper particle size for the as-synthesized and spent catalysts are investigated by transmission electron microscopy (TEM) analysis, depicted in the appendix in figures D.2 and D.3. Accompanying histograms are presented in the appendix in figures E.2 and E.3. In figure 3.19 selected as-synthesized and spent catalysts supported on oxCNTs and HSAG are displayed. From all TEM images and the accompanying histograms it could be observed that the copper particles grew significantly. The calculated surface-averaged particle sizes for each tested catalyst are presented in tables 3.13 and 3.14 and in the appendix in table F.1. Furthermore, the histograms suggest that a coalescence-like particle growth was present during catalysis by the fact that no increase of smaller particles were observed. However, after a prolonged time of particle growth, which could be after 250 h of catalysis, all *in situ* generated, smaller nanoparticles could be consumed for the growth of the larger nanoparticles. Hence, no Ostwald ripening would be observed after 250 h of catalytic testing. In addition, from the TEM analyses of the spent, HSAG-supported catalysts it appeared that

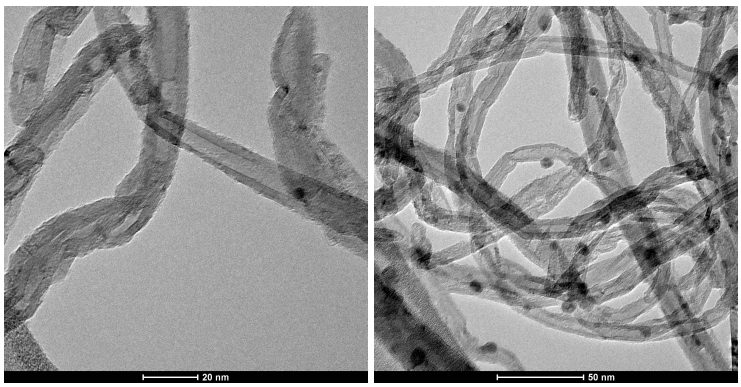

(a) MnO-Cu/oxCNT fresh **(b)** MnO-Cu/oxCNT spent

(c) ZnO-Cu/HSAG fresh **(d)** ZnO-Cu/HSAG spent

Figure 3.19 TEM images of two selected as-synthesized and spent catalysts. From these images it appeared that the relative copper particle growth was higher for the oxCNT-supported catalysts compared to the HSAG-supported catalysts.

the most abundant particles were approximately of the same size compared to their sizes in the corresponding as-synthesized catalysts, as could be derived from the histograms in figure E.3. However, some considerably large nanoparticles were formed during catalysis, as visualized by the histograms and TEM images, depicted in figure E.3 and for example figure 3.19d. Hence, these significantly large nanoparticles increased the surface-averaged particle size and the accompanying relative uncertainty significantly. To investigate if Ostwald ripening was present during catalysis particle size distributions have to be determined by TEM after only several hours of catalysis.

With HAADF-STEM-EDX of the MnO-Cu/oxCNT catalyst, depicted in figure 3.16, it could be observed that the manganese particle size increased considerably upon catalysis. Despite this observation with HAADF-STEM-EDX no discrimination between copper and the promoter species could be discerned by TEM analysis, due to the fact that barely no phase contrast was available between those metal species. As a result, during particle size analysis of the spent MnO-Cu/oxCNT catalyst both copper and manganese oxide were counted. To overcome this miscounting problem a mean particle size determination with a simultaneous chemical mapping with EDX might be performed, although this would be a considerably elaborate characterization technique.

From tables 3.13 and 3.14 and in the appendix table F.1 it appeared that the copper particle growth was more pronounced for the oxCNT-supported catalysts than for the catalysts supported on HSAG. An explanation for this observation was derived from the difference in the effective metal surface loading between the two supports, as already discussed in the titrations section 3.2.2.6. Indeed, as the copper nanoparticles were significantly larger for the

as-synthesized, HSAG-supported catalysts (except for the Cr-promoted one) compared to the copper nanoparticles for the as-synthesized, oxCNT-supported catalysts, the promoter species were presumably also larger. However, this was not irrefutably proven by the TEM and XRD analyses, described in sections 3.2.2.3 and 3.2.2.4, respectively. Due to the presumably larger promoter nanoparticles in the as-synthesized, HSAG-supported catalysts the effective surface loading was therefore lowered to a less extent. As a result, the relative 2D distance between the copper nanoparticles on the oxCNT-supported catalysts was lower compared to the copper nanoparticles on the catalysts supported on HSAG. Hence, a larger particle growth rate was observed for the oxCNT-supported catalysts compared to the HSAG-supported catalysts.

Surprisingly, it seemed that after the comparison of the stability curves between the carbon supports, depicted in figure 3.20, the larger rate of particle growth for the copper nanoparticles supported on oxCNTs did not affect the stability profile during catalytic testing. In fact, nearly the same deactivation behaviors were observed between the oxCNT-supported catalysts and their corresponding HSAG-supported catalysts. It was however expected that the faster rate of particle growth for the oxCNT-supported catalysts steepened the catalyst deactivation in the beginning of the corresponding stability curves. Furthermore, the presence of nearly identical stability profiles between the catalysts supported on the different

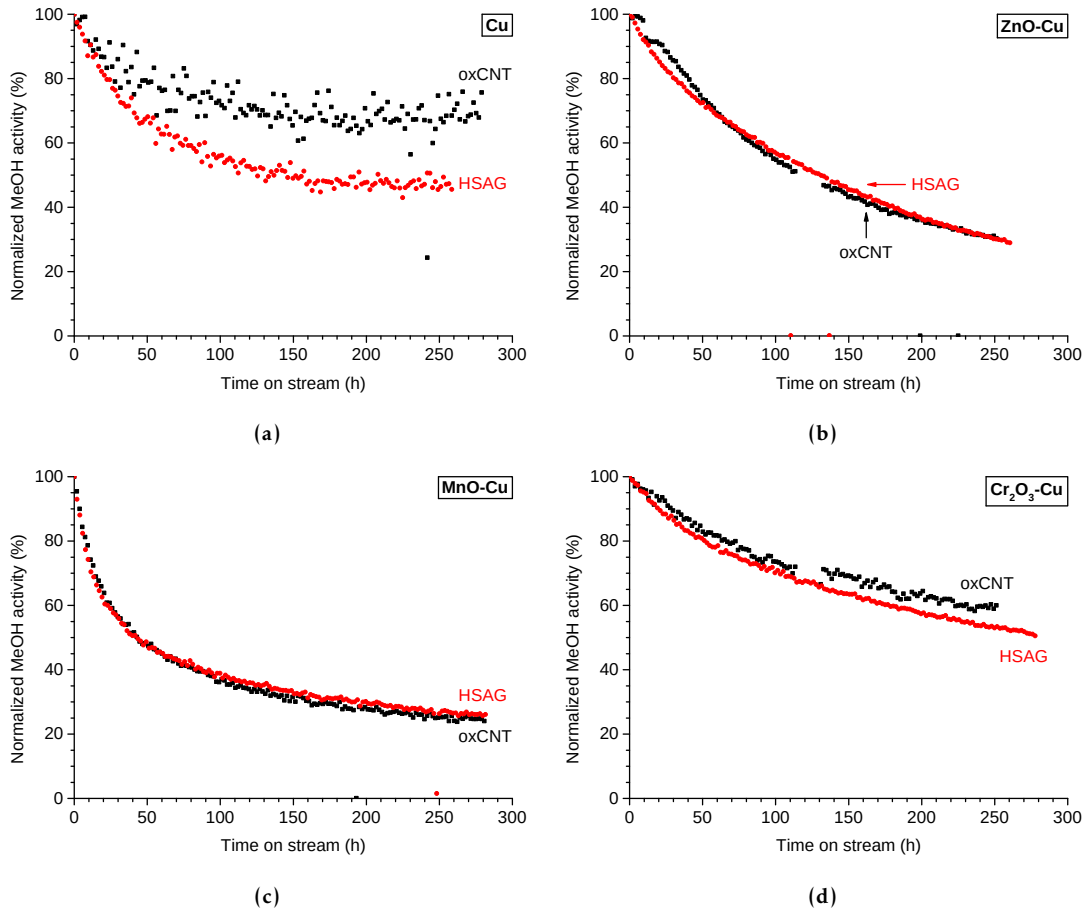

Figure 3.20 Stability curve comparisons with the normalized activity (NA) between oxCNT- and HSAG-supported catalysts. From the promoted catalysts in figures **b**-**d** in appeared that the no any significant difference between the stability profiles was present between the different supports. This indicated the large rate of particle growth for the oxCNT-supported copper nanoparticles and the different morphology and acidity between the supports had no influence. The difference for the non-promoted catalysts in figure **a** indicated particle growth prior to $t = 0$.

carbon supports suggested that the different morphology and acidity between the supports did not affect the rate of catalyst deactivation. However, as the individual impact of the particle growth rate and the different supports could not be discriminated from the comparison plots, as shown in figure 3.20, it might be that the combination of both effects diminish the differences in the stability profiles. Finally, from figure 3.20 a difference between the stability curves of the non-promoted catalysts could be observed. An explanation for this phenomenon is presented in section 3.3.1: due to a plausible, initial copper particle growth for the oxCNT-supported catalyst the maximum normalized activity towards methanol was reached before the first measurement was taken.

3.3.3.2 Crystallite Size Analysis

The copper particle growth during 250 h of catalysis was next to transmission electron microscopy (TEM), as described in section 3.3.3.2, also analyzed with X-ray diffraction (XRD). The advantage of using XRD analysis is that element-specific crystallite growth could be determined, or equivalently, the growth of copper and accompanied promoter separately. Figures 3.21a-b display the diffractograms of the promoted, spent catalysts supported on oxCNTs and HSAG, respectively. These diffractograms were compared to the diffractograms obtained from their corresponding as-synthesized catalysts, as depicted in figures 3.21c-d. The diffractograms of the spent catalysts were obtained after passivation under ambient conditions, whereas the as-synthesized catalysts underwent an *in situ* oxidation at 200 °C prior to XRD analysis, as described in section 2.1.4. Therefore, no valuable crystallite size determinations for the spent catalysts could be performed. However, the presence of crystalline promoters might indicate the growth of promoter species.

From figure 3.21a diffraction peaks due to the zinc oxide promoter were observed for the spent ZnO-Cu/oxCNT catalyst. As these peaks were absent for the corresponding as-synthesized catalyst, as depicted in figure 3.21c, it could be concluded that the growth of zinc species occurred during catalysis. As a result, this promoter growth indicated that a the promoting effect of zinc oxide was diminished. This observation was in line with the turn over frequency (TOF) analysis, discussed in section 3.3.3.3. Furthermore, from figure 3.21a a considerably broad peak in the Cr_2O_3-Cu/oxCNT diffractogram could be discerned at 31°, which suggested the presence of CrO_3. As this peak indicated small chromium nanoparticles, this was in agreement with the HAADF-STEM-EDX analysis, as depicted in figure 3.17b. However, the highly oxidizing Cr(VI) species was presumably not stable and should be converted into its more stable Cr(III) form. Finally, for the spent MnO-Cu/oxCNT catalyst, shown in figure 3.21a, no manganese-related diffraction peaks were observed. This was in disagreement with the HAADF-STEM-EDX analysis, displayed in figure 3.16b, which showed considerably large, separate manganese nanoparticles. In addition of this disagreement, these manganese nanoparticles in the spent catalyst were also significantly larger compared to the chromium nanoparticles in the spent Cr_2O_3-Cu/oxCNT catalyst, as depicted in figure 3.17b. Moreover, no peaks related to crystalline copper species were noticed for the diffractogram of the spent MnO-Cu/HSAG catalyst, displayed in figure 3.21a. However, this was expected according to TEM analysis of the spent catalysts, described in section 3.3.3.1, which showed that the volume-averaged copper particle sizes of the spent MnO-Cu/HSAG catalyst were comparable to those of the spent, oxCNT-supported catalysts. These unexpected observations regarding to the absence of diffraction peaks related to manganese and copper species might be explained by the fact that no proper crystallization took place.

Figure 3.21b depicts the diffractograms of the spent, promoted, HSAG-supported catalysts. For the spent ZnO-Cu/HSAG and MnO-Cu/HSAG catalysts a significant amount of metallic copper was observed compared to all other diffractograms of the spent catalysts, displayed in figures 3.21a-b. This observation could be related to their considerably larger, mean copper particle sizes, as depicted in the appendix in table F.1. Next, in figure 3.21b diffraction peaks for the ZnO-Cu/HSAG catalyst due to zinc oxide were again observed, compared to the

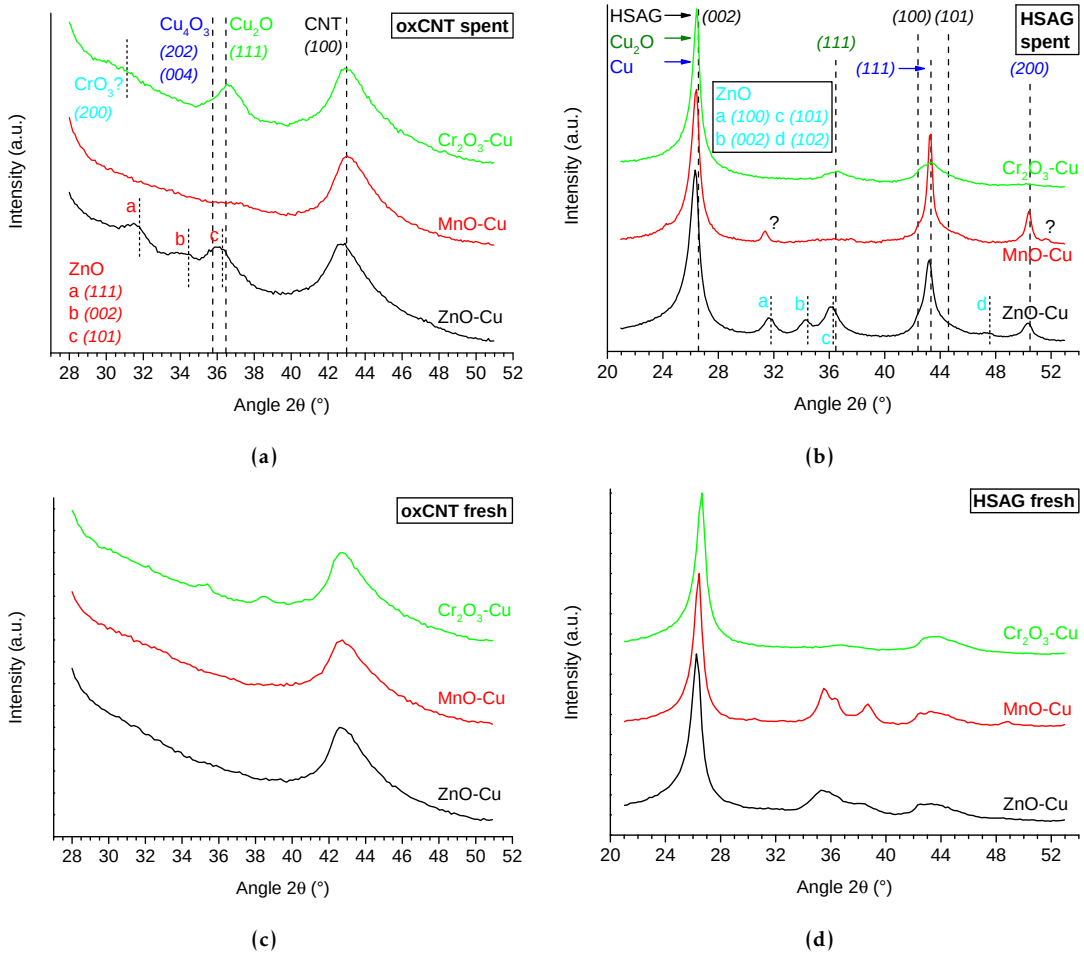

Figure 3.21 XRD diffractograms of the (**a**, **c**) oxCNT-supported and (**b**, **d**) HSAG-supported catalysts; (**a**, **b**) Spent catalysts with (**c**, **d**) their corresponding as-synthesized catalysts. X-ray source: Cu anode. Diffractograms of the spent catalysts were obtained after catalyst passivation under ambient conditions, whereas the as-synthesized catalysts underwent an *in situ* oxidation at 200°C prior to XRD analysis, as described in section 2.1.4. Figures **c**-**d** were already depicted in figures 3.11b-c, respectively. From these figures it could be derived that the zinc promoters grew significantly for both catalyst series. For the spent Cr_2O_3-Cu/HSAG catalyst barely no particle growth was observed. For the spent, Mn-promoted catalysts no Mn- or copper oxide-related diffraction peaks were obtained, indicating amorphization.

diffractogram of its oxCNT-supported counterpart, depicted in figure 3.21a. As a result, this significant growth of the zinc oxide promoter could explain the strong deactivation during catalysis, as derived from figure 3.18a. Furthermore, for the spent Cr_2O_3-Cu/HSAG catalyst, as shown in figure 3.21b, barely any difference was observed compared to its as-synthesized counterpart, displayed in figure 3.21d. The only broad peak at 36.5° in both diffractograms corresponds to Cu_2O or to a severe overlap of the CuO diffraction peaks, present at 35.5° and 38.9°, as described in section 3.2.2.4. This observation indicated that considerably small copper nanoparticles were present in both the as-synthesized and spent Cr_2O_3-Cu/HSAG catalysts and hence no significant particle growth was present during catalysis. This was in agreement with the high stability of the Cr_2O_3-Cu/HSAG catalyst during catalysis, as depicted in figure 3.18b. Again, this observation indicated that chromium is a good structural promoter.

Finally, for the spent MnO-Cu/HSAG catalyst no manganese- and copper oxide-related diffraction peaks could be observed, as shown in figure 3.21b. As this result was also observed for the spent MnO-Cu/oxCNT catalyst, depicted in figure 3.21a, it suggested that during catalysis the manganese- and copper oxide-related species amorphorized the outer layer of copper-based nanoparticles, while keeping metallic copper species untouched. This suggestion was in agreement with the stability profiles for the MnO-Cu/oxCNT and MnO-Cu/HSAG catalysts, as depicted in figures 3.14a and 3.18a, showing a rapid deactivation during the first 80 h of catalysis in which the amorphorization might took place. After 80 h this amorphous shell might be around maximum thickness, diminishing the stability decay significantly. However, two peaks were found in the diffractogram of the MnO-Cu/HSAG catalyst, as depicted in figure 3.21b, which could not be assigned to any known manganese, copper, or bimetallic species.

3.3.3.3 Turn Over Frequencies

A difference in the turn over frequency (TOF) values at the start and end of catalysis could indicate a loss of promoter effect. If no promoters were present or no loss of promoter effect was present the TOF values must indeed be constant, assuming an inverse, linear relation existed between the surface-averaged copper particle diameter d_S and the CO + CO_2 conversion χ_{CO+CO_2}. The calculation of the TOF values is described in section 2.3.1.

Table 3.15 presents the TOF values of the tested catalysts at the start and end of catalysis. These values were compared to the surface-averaged copper particle diameters d_S in the last two columns. The uncertainties in the TOF values were estimated by the standard deviation in the corresponding d_S.

In table 3.15 it could be observed that the uncertainties for each obtained TOF value was considerably high, especially for the HSAG-supported catalysts. As a result, the TOF values at the start and end of the catalytic testing were for almost each catalyst within the experimental error. Therefore, determinations of a possible loss of promoter effect for the spent catalysts were challenging.

Table 3.15 Turn over frequencies (TOFs) of the oxCNT- and HSAG-supported catalysts at the start and end of catalysis. The TOF values are compared to the surface-averaged copper particle diameter d_S, obtained by TEM. Uncertainties in the TOF values were estimated from the standard deviations in the mean copper particle diameters. Only for the ZnO-Cu/oxCNT catalyst the loss of promoter effect could be derived from the TOF values. t = time-on-stream.

catalyst		**TOF (10^{-3} s^{-1})**		**d_S (nm)**	
support	metal	$t = t_0$	$t = t_{max}$	fresh	spent
oxCNT	Cu	0.30 ± 0.13	0.7 ± 0.2	2.3 ± 1.0	6.1 ± 1.8
	ZnO-Cu	11 ± 4	3.6 ± 1.1	4.5 ± 1.7	5.2 ± 1.6
	MnO-Cu	2.0 ± 1.1	5 ± 2	1.7 ± 1.0	6 ± 2
	Cr_2O_3-Cu	2.1 ± 1.0	1.8 ± 0.7	2.5 ± 1.2	5.0 ± 1.8
HSAG	Cu	1.5 ± 0.9	1.0 ± 0.8	13 ± 8	14 ± 11
	ZnO-Cu	11 ± 9	6 ± 3	9 ± 7	11 ± 5
	MnO-Cu	13 ± 20	3 ± 4	21 ± 31	17 ± 25
	Cr_2O_3-Cu	6 ± 3	4.0 ± 1.4	7 ± 3	7 ± 3

Only the Cu/oxCNT, ZnO-Cu/oxCNT, and MnO-Cu/oxCNT catalysts showed a significant difference between their corresponding TOF values at the start and end of catalysis. Surprisingly, for the non-promoted catalyst an increase in the TOF value was observed: from $0.30 \times 10^{-3}\,s^{-1}$ to $0.7 \times 10^{-3}\,s^{-1}$. An increase in the TOF would however be impractical, because that would suggest that during catalysis exposed copper metal sites would become more active towards CO + CO_2 conversion. This observation could be explained by the copper particle growth prior to catalysis. Indeed, for the TOF calculation the surface-averaged copper particle diameter d_S of the as-synthesized Cu/CNT catalyst ($2.3 \pm 1.0\,nm$) and the catalyst mass-based activity z_{CO+CO_2} at time-on-stream $t = t_0$ was used. Therefore, the prior copper particle growth decreased the TOF value of the Cu/oxCNT catalyst at $t = t_0$ significantly.

For the ZnO-Cu/oxCNT catalyst a decrease in the TOF value was observed. If the TOF decreased after catalysis the methanol activity decreased more than the d_S increased and thus a third variable must have altered the TOF. This phenomenon could be attributed to the loss of promoter effect. To confirm this promoter loss clustering of zinc oxide nanoparticles have to be observed with HAADF-STEM-EDX.

For the MnO-Cu/oxCNT catalyst a decrease in the TOF value was expected as the clustering of manganese particles for the spent MnO-Cu/oxCNT catalyst was observed with HAADF-STEM-EDX, as presented in figure 3.16b. However, an increase in the TOF value upon catalysis was observed. This result could be explained by the higher CO + CO_2 conversion towards long-chain hydrocarbons after prolonged time of catalysis, as displayed in figure 3.15a. This increased catalyst mass-based activity might be induced by the presence of cobalt-manganese nanoparticles, in which cobalt originates from the CNT growth catalyst.

3.4 Copper Colloid Synthesis

To prepare well-defined model catalysts for methanol synthesis a colloidal approach was pursued to obtain monodisperse copper colloids as a starting point. This monodispersity would be the key parameter to diminish or even exclude the Ostwald ripening as one of the particle growth modes during catalytic testing. Ideally, the catalyst deactivation would then only be caused by coalescence, another mode of particle growth.

The copper colloids were synthesized after the article of Yin *et al.* [37], as described in section 2.1.1. After 14 syntheses, as depicted in table 2.1, no monodisperse copper colloids could be obtained. For the 'colloidal' solution obtained after the experiment of entry 3 of this table transmission electron microscopy (TEM) images were taken. These images are presented in figure 3.22. From figure 3.22a copper aggregates of several micrometers could observed, which were also visible to the naked eye. However, figure 3.22b shows that also several relatively monodisperse colloids of approximately 50 nm were synthesized. Nevertheless, a colloidal size of approximately 7.5 nm was expected, according to Yin *et al.* [37]. For the other colloidal syntheses no TEM images were taken, but the inhomogeneity as observed for the 'colloidal' solution obtained after the experiment of entry 3 was also noticed for the other solutions.

An explanation for the unsuccessful colloidal syntheses might be the source of the copper(I) acetate (CuOAc) reagent. Indeed, figure 3.23 displays the color difference of the CuOAc between two different bottles of the same chemical supplier, indicating that apparently different purities were present. For the experiments of entries 1-11 of table 2.1 the light green CuOAc was used, as depicted in figure 3.23a, whereas for the experiments of entries 12-14 the 'forest green' CuOAc was used, shown in figure 3.23b. As the synthesis procedure reported by Yin *et al.* [37] describes the use of 'forest green' CuOAc, it was expected that successful colloidal syntheses were obtained with this reagent. However, no monodisperse colloidal solutions were obtained. In addition, for different molar scales, heating rates, reaction

temperatures, heating times, oleic acid purity, and solvents (trioctylamine and oleylamine) the copper colloidal synthesis was endeavored several times, but appeared to be yet unsuccessful.

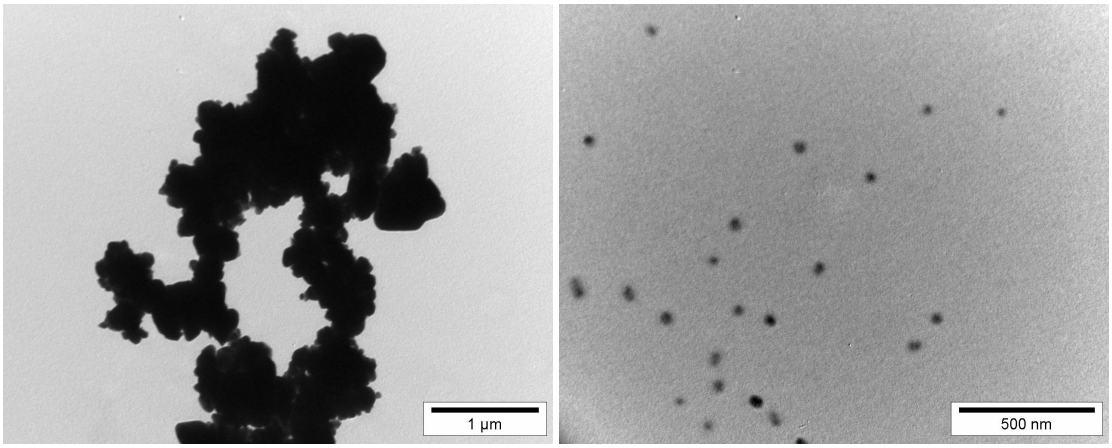

Figure 3.22 TEM images of copper aggregates and colloids, taken from the 'colloidal' solution obtained after the experiment of entry 3 of table 2.1. Figure **a** shows copper aggregates of several micrometers, visible by the naked eye. Figure **b** shows relatively monodisperse copper colloids of approximately 50 nm, whereas a colloidal size of approximately 7.5 nm was expected. No mean copper colloid size and corresponding histogram were calculated.

Figure 3.23 Copper(I) acetate (CuOAc) from different bottles of the same supplier. **a** Light green, from 'old' bottle. **b** Forest green, from 'new' bottle. According to the reported synthesis procedure of Yin *et al.* [37] a forest green CuOAc reagent has to be used.

4 Conclusions

In the chemical industry the $Cu/ZnO/Al_2O_3$ catalyst is used to convert CO_2-enriched synthesis gas (H_2/CO) into methanol. Within this catalyst the zinc oxide promoter enhances the catalytic activity, but simultaneously destabilizes the methanol production significantly. In literature the promoting effects of other metals, such as manganese [40–43] and chromium [41, 44–46], upon metallic copper are investigated. However, those articles generally lack in a simultaneous reporting of the stability, activity, and selectivity of these promoted catalysts. In addition, catalytic testings up to for example 250 h are commonly not reported. Furthermore, the promoter effects may be influenced by the presence of a metal oxidic support, leading to the need of an inert support to investigate promoter-specific effects. Therefore, this thesis reports the effects of zinc, manganese, and chromium addition to copper-based, carbon-supported catalysts. More specifically, the effect of promoter addition on the copper particle size and the catalytic performance of the catalysts were investigated in this thesis.

Effect of carbon supports and promoter addition on the copper particle size
Pristine carbon nanotubes (CNTs), oxidized carbon nanotubes (oxCNTs), and high surface area graphite (HSAG) were used as the preferred carbon supports. The CNTs were successfully modified to oxCNTs by liquid phase oxidation (LPO). As a result, a significant increase in BET surface area and acidic group concentration on the support surface were observed upon this modification. Commercial HSAG possesses an acidity in between of CNTs and oxCNTs.

Catalysts were successfully prepared by incipient wetness impregnation (IWI) of the CNTs, oxCNTs, and HSAG by an aqueous metal nitrate solution and subsequent direct reduction. The LPO of CNTs led to the deposition of smaller copper nanoparticles on the oxCNT support (2.5 nm vs. 6 nm), induced by the higher amount of anchoring sites for the copper particles. The copper nanoparticles deposited on HSAG were significantly larger than on the tube-like supports, induced by the different support morphology.

The addition of finely dispersed zinc, manganese, or chromium promoters to the tube-like supports, as confirmed by X-ray diffraction (XRD), did not have any significant effect on the copper particle size. However, for HSAG-supported catalysts manganese promotion significantly increased the copper particle size and corresponding polydispersity, whereas chromium promotion decreased this particle size.

Catalytic performance of promoted catalysts
The catalytic performance of oxCNT- and HSAG-supported catalysts was investigated during 250 h of methanol synthesis. Prior to catalysis catalytically active, metallic copper was obtained via an *in situ* reduction, as confirmed by temperature-programmed reduction with hydrogen (H_2-TPR). In this thesis the observed high initial activity and high instability of the zinc-promoted catalysts was in agreement with reported literature. The loss of the zinc promoter effect was confirmed by a decay in the turn over frequency (TOF). Furthermore,

manganese and chromium were less strong chemical promoters than zinc, whereas in addition the methanol production of the manganese-promoted catalysts was not stabilized. This loss of the manganese promoter effect was observed as nanoparticle clustering by HAADF-STEM-EDX. However, chromium also acted as a good structural promoter for the carbon-supported catalysts by diminishing the copper particle growth. This observation was in agreement with the reported results by Kilo *et al.* [41] and Yurieva *et al.* [46].

The high selectivity towards methanol was for most of the tested catalysts preserved over 250 h of catalysis. However, the MnO-Cu/oxCNT catalyst showed an increase in the C5+ product selectivity after prolonged time of catalysis, presumably induced by the presence of Fischer-Tropsch-active cobalt-manganese species.

This thesis shows that the addition of finely dispersed chromium oxide to HSAG-supported copper nanoparticles leads to the synthesis of small copper particles, enhances the initial activity of the methanol synthesis, and stabilizes the catalytic stability for over 250 h of catalysis.

Synthesis of copper colloids
In addition to the investigation of promoter effects on methanol synthesis catalysts the effects of using monodisperse copper colloids on the catalytic performance was explored. Indeed, monodisperse nanoparticles would induce less Ostwald ripening, leading to different catalytic stability behaviors. However, the syntheses of copper colloids were yet unsuccessful and hence the corresponding research objectives could not be answered.

5 Outlook

As was discussed in sections 3.3.1 and 3.3.2 the manganese, chromium, and especially zinc promoters enhanced the initial activity of the catalysts during 250 h of catalysis significantly, whereas chromium also enhanced the methanol production stability considerably. Hence, from stability tests of the promoted, CNT-supported catalysts valuable information could be retrieved.

The CO + CO_2 conversion (χ_{CO+CO_2}) of the MnO-Cu/oxCNT catalyst decayed during the first hours of catalysis, but increased after approximately 80 h, as depicted in figure 3.15a. During the increase of χ_{CO+CO_2} the C5+ selectivity, corresponding to Fischer-Tropsch-like products, increased accordingly as depicted in figure 3.15b. This phenomenon was ascribed to the presence of cobalt-manganese species. The presence and amount of the cobalt growth catalyst in the oxidized carbon nanotubes (oxCNTs) could be verified with inductively coupled plasma mass spectrometry (ICP-MS). To validate the activity behavior of the MnO-Cu/oxCNT catalyst during catalysis the catalytic test has to be reproduced.

A sudden drop in χ_{CO+CO_2} was observed for the Cr_2O_3-Cu/oxCNT catalyst during catalysis, as depicted in figure 3.15a, attributed to a GC malfunction. Hence, this sudden decrease was also displayed in the corresponding χ_{CO+CO_2}-derived copper time yield (CTY) and catalyst mass-based activity (z_{CO+CO_2}), displayed in figures C.3a and C.5a, respectively. To obtain more valuable activity and conversion curves the stability test of the Cr_2O_3-Cu/oxCNT catalyst has to be redone.

For the Cu/oxCNT catalyst (and to a smaller extent for the Cu/HSAG catalyst) a significant scattering in the stability curves was observed, as derived from figures 3.14a and 3.18a, respectively. This observation was attributed to copper particle growth prior to the catalysis conditions were reached. To confirm this hypothesis a catalytic test of the Cu/oxCNT catalyst has to be performed for only several hours. Afterwards, it could be validated by transmission electron microscopy (TEM) if severe particle growth will be present prior to catalysis.

During 250 h of catalysis the supported copper particles could sinter by coalescence or Ostwald ripening. In the histograms of the spent catalysts, depicted in the appendix in figures E.2b, d, f, and h and E.3b, d, f, and h, it appeared that particle growth was only present due to coalescence, as no smaller nanoparticles were observed. To validate that Ostwald ripening was not the main deactivation mode during catalysis an oxCNT- or HSAG-supported catalyst has to be tested for approximately two days. If again no smaller nanoparticles are observed in the TEM images, no Ostwald ripening is likely to be present during catalytic testing.

In addition, fitting of the stability curves could be performed to obtain a quantitative way to describe the stability curves.

High-angle, annular, dark-field, scanning-transmission electron microscopy with energy-dispersive X-ray (HAADF-STEM-EDX) analysis, as described in section 3.3.1, could be used to confirm the clustering of zinc oxide in the zinc-promoted catalysts into relatively large nanoparticles after 250 h of catalysis. This suggestion was derived from the fact that the zinc-promoted catalysts deactivated rapidly, as depicted in figures 3.14b and 3.18b, and that the TOF values declined significantly after catalysis, as described in section 3.3.3.3.

From the turn over frequency (TOF) analyses of the oxCNT- and HSAG-supported catalysts, described in section 3.3.3.3, it appeared that the relative uncertainties within the obtained values were significantly large, induced by the broad copper particle size distributions of the catalytic systems. Therefore, these uncertainties hampered the interpretation for the promoted catalysts on a potential loss of promoter effect. To obtain more valuable TOF data catalytic model systems with well-defined nanoparticle sizes have to be prepared. To achieve this, the catalyst synthesis procedure could be altered by for example different promoter concentrations, a different program for the direct reduction and subsequent *in situ* oxidation, and a different drying procedure. Alternatively, a colloidal copper approach might be used as they could be synthesized with a small particle size distribution, although the investigation of the promoter effect will be challenging.

The thermogravimetric analysis (TGA) experiments of the as-synthesized catalysts, as described in section 3.2.2.5, were only performed for the Cu/CNT and Cu/HSAG catalysts under an oxygen atmosphere. To validate that these catalysts were also stable during catalysis TGA measurements under a reducing atmosphere have to be performed. Furthermore, promoted catalysts can be investigated by TGA under reducing atmospheres to verify that the addition of promoters does not significantly alter the support stability. Moreover, the TGA experiments of the bare supports, as described in section 3.1.2.3, were all performed under an oxygen and hydrogen atmosphere. However, to obtain the most valuable TGA curves the measurements have to be performed under a syngas feed as used in the reactor for catalytic testing ($Ar:CO_2:CO:H_2$ = 10:7:23:60 vol%). Furthermore, in the corresponding mass spectrometry (MS) plots under an oxygen atmosphere, displayed in figures 3.3a, c, and e, the high ion current in the first 80 min of the m/z 28 channel was due to the slow disappearance of nitrogen, applied in the prior isotherm. To obtain nitrogen-corrected MS plots a hydrogen or oxygen isotherm of approximately 80 min have to be applied prior to heating.

From the H_2-TPR plots of the as-synthesized catalysts, shown in figure 3.12 in section 3.2.2.5, the multiple peaks might be assigned to a stepwise reduction of copper(II) oxide to metallic copper. To verify if this was the case the H_2-TPR experiments could be performed at a lower heating rate: $2\,°C \cdot min^{-1}$ vs. $5\,°C \cdot min^{-1}$. If the overlapping peaks separate the multiple peaks in the H_2-TPR plots could be assigned to different copper reduction steps. If no peak separation will be observed but only a total peak shift, the described explanation in section 3.2.2.5 will be prevailing: copper nanoparticles deposited inside and outside the nanotubes exhibit a different reduction temperature. To validate this hypothesis the IWI could be performed with impregnation solutions based on more hydrophobic solvents, such as isopropanol and ethanol. It is expected that a higher hydrophobicity of the solvent might change the deposition ratio of the copper nanoparticles on the inner and outer nanotube surface. Hence, a peak intensity shift is expected within the multiple copper oxide reduction peaks. Finally, in H_2-TPR plot of ZnO-Cu/oxCNT, depicted in figure 3.12b, an unexpected peak appeared at 375 °C. The origin of this peak could not be derived from the reduction of zinc oxide and/or from the reduction of oxygen-containing groups, as derived from titrations described in section 3.2.2.6. To further validate that the reduction peak has not been caused to acidic group reduction, TGA-MS experiments could be applied to ensure no significant mass loss due to acidic groups was present for the ZnO-Cu/oxCNT catalyst. Hence, the H_2-TPR experiment for the ZnO-Cu/oxCNT catalyst has to be redone to verify if the occurrence of the peak at 375 °C was artificial.

From the H_2-TPR/TPO/H_2-TPR experiments, as described in section 3.2.2.1, it appeared that the large copper nanoparticles deposited on for example the Cu/HSAG catalyst were not fully oxidized, even after an oxidation up to 400 °C. To confirm this incomplete oxidation of the copper nanoparticles X-ray diffraction (XRD) experiments could be performed of the Cu/HSAG catalyst after the oxidation treatment at 400 °C to confirm this incomplete oxidation of copper. The H_2-TPR/TPO/H_2-TPR and the subsequent, particular XRD measurements could also be performed for the MnO-Cu/HSAG catalyst, exhibiting an even larger mean copper particle size, to compare this to the results of the Cu/HSAG catalyst.

The oxidation states of the carbon-supported manganese and chromium promoters could not be validated by XRD, as described in section 3.2.2.4, due to their small appearance. Therefore, X-ray photoelectron spectroscopy (XPS) can be used to validate the Zn(II) oxidation state and the expected Mn(II) and Cr(III) oxidation states in the as-synthesized catalysts. To obtain a suggestion of the present metal oxidation states during catalysis XPS has to be performed after an *in situ* reduction.

In this thesis a copper weight loading analysis was performed on all as-synthesized catalysts by temperature-programmed reduction with hydrogen (H_2-TPR), described in section 3.2.2.5, and for the as-synthesized Cu/CNT and Cu/HSAG catalysts also by thermogravimetric analysis (TGA), described in section 3.2.2.2. The obtained copper weight loadings were compared to the calculated, theoretical weight loading, as presented in section 3.2.1. However, no good correlations between the H_2-TPR-obtained copper weight loadings of the HSAG-supported catalysts could be obtained. Hence, inductively coupled plasma mass spectrometry (ICP-MS) can be performed to verify the copper weight loading. In addition, with this technique weight loadings of the promoters can be determined. From the metal weight loading the copper time yield (CTY) and turn over frequency (TOF) can be calculated with higher accuracy. Finally, a TGA experiment under an oxygen atmosphere up to 800 °C for the as-synthesized Cu/oxCNT catalyst would deliver a copper weight loading for this specific catalyst, as at this high temperature the oxCNTs were fully oxidized, as described in section 3.1.2.3.

As described in section 3.2.1 the pH values of the impregnation solutions differ substantially from each other. These pH differences could have affected the metal nitrate solubility in the impregnation solutions and hence the point of metal deposition while drying after incipient wetness impregnation (IWI). As a result, the metal distribution over the carbon supports might be affected by this pH difference and/or by the nature of the promoter and support. To exclude this pH effect from the promoter and support effects on the mean copper particle size each impregnation solution must be acidified by different amounts of HNO_3 to a pH of 1. Consequently, new catalyst series have to be synthesized with these corrected impregnation solutions.

Acknowledgements

During this project there were a lot of people who helped me with my research, which I would like to thank. At first, I would really like to thank my daily supervisor Lisette Pompe and professor Petra de Jongh. Lisette was always helpful and ready to help me with my research, whereas professor De Jongh gave me the opportunity to do my master's thesis about this subject. Moreover, Lisette imaged all my synthesized catalysts with TEM and helped me with the loading of the catalytic reactor, for which I would like to thank her. Also in the beginning of this project Roy van den Berg helped me with the loading of this reactor.

The project started off with the synthesis of colloidal copper particles. I would like to thank Marianna Casavola, who helped me to get a grip onto the colloidal synthesis procedure.

Furthermore, I would like to thank people who helped me with the characterization techniques of my catalysts. At first, Wouter Lamme helped me a lot with the HAADF-STEM-EDX method and the titration set-up. Geert van Stuijvenberg and Baira Donoeva also helped me a lot with the titration experiments. Next, I would like to thank Gang Wang and Carlos Hernandez Meija, who helped me with the H_2-TPR and TPO experiments. Also Marjan Versluijs-Helder helped me a lot with the execution of the TGA measurements, whereas Jeroen van den Reijen gave me support in the analysis of the corresponding results. Peter Bramwell helped me with providing the N_2 physisorption data. Finally, I would like to thank Lars van der Wal, whose bachelor's thesis provided the basis of this research.

At last but not at least, I would like to thank Koen Bossers, Geert van Stuijvenberg, and Laurens Mandemaker for the fruitful discussions and all other people of the Inorganic Chemistry and Catalysis group with whom I had a really great time during my master's thesis.

Bibliography

[1] U.S. Energy Information Administration (eia), *Technically recoverable shale oil and shale gas resources: An assessment of 137 shale formations in 41 countries outside the United States*, Technical report, U.S. Department of Energy, Washington, D.C., 2013, URL: *http://www.eia.gov/analysis/studies/worldshalegas/pdf/fullreport.pdf*.

[2] Methanol Market Services Asia (MMSA), *Methanol supply and demand balance*, Technical report, 2013, URL: *http://www.methanolmsa.com/*.

[3] Methanol Market Services Asia (MMSA), *Methanol*, 2014, URL: *http://www.methanolmsa.com/methanol/*.

[4] Liu, X.-M., Lu, G., Yan, Z.-F., and Beltramini, J., *Recent advances in catalysts for methanol synthesis via hydrogenation of CO and CO_2*, Ind. Eng. Chem. Res., 42(25), 6518–6530, 2003, URL: *http://pubs.acs.org/doi/abs/10.1021/ie020979s*.

[5] Methanol Institute, *Methanol*, 2011, URL: *http://methanol.org/*.

[6] Olah, G., *Beyond oil and gas: The methanol economy*, Angew. Chem. Int. Ed., 44(18), 2636–2639, 2005, URL: *http://www.ncbi.nlm.nih.gov/pubmed/15800867*.

[7] Deeb, R., Anderson, T., Kavanaugh, M., and Kell, L., *Methanol: Fate and transport in the environment*, in: *The toxicology of methanol*, edited by Clary, J., chapter 2, pp. 11–46, John Wiley & Sons, Inc., Hoboken, New York: U.S.A.2013, 1st edition, ISBN 978-047031759-4.

[8] Barceloux, D. G., Bond, G. R., Krenzelok, E. P., Cooper, H., and Vale, J. A., *American Academy of Clinical Toxicology practice guidelines on the treatment of methanol poisoning*, J. Toxicol. Clin. Toxicol., 40(4), 415–446, 2002, URL: *http://www.ncbi.nlm.nih.gov/pubmed/12216995*.

[9] Khassin, A., Minyukova, T., and Yurieva, T., *Genesis of catalysts for methanol synthesis*, Mendeleev Commun., 24(2), 67–74, 2014, URL: *http://linkinghub.elsevier.com/retrieve/pii/S0959943614000029*.

[10] Waugh, K., *Methanol synthesis*, Catal. Lett., 142(10), 1153–1166, 2012, URL: *http://link.springer.com/10.1007/s10562-012-0905-2*.

[11] Ratnasamy, C., and Wagner, J., *Water gas shift catalysis*, Catal. Rev., 51(3), 325–440, 2009, URL: *http://www.tandfonline.com/doi/abs/10.1080/01614940903048661*.

[12] Zhang, Q., He, D., and Zhu, Q., *Recent progress in direct partial oxidation of methane to methanol*, J. Nat. Gas Chem., 12(2), 81–89, 2003, URL: *http://www.jngc.dicp.ac.cn/jngc/2003/03-02/2003-02-0081.pdf*.

[13] Tang, P., Zhu, Q., Wu, Z., and Ma, D., *Methane activation: The past and future*, Energy Environ. Sci., 7(8), 2580–2591, 2014, URL: *http://xlink.rsc.org/?DOI=C4EE00604F*.

[14] Aasberg-Petersen, K., Stub Nielsen, C., Dybkjæ r, I., and Perregaard, J., *Large scale methanol production from natural gas*, Technical report, Haldor Topsøe, Lyngby, 2008, URL: *http://www.topsoe.com/sites/default/files/topsoe_large_scale_methanol_prod_paper.ashx_.pdf*.

[15] Roine, A., Lamberg, P., Mansikka-aho, J., Björklund, P., Kentala, J.-P., Talonen, T., Kotiranta, T., Ahlberg, R., Gröhn, A., Saarinen, O., Myyri, J., Sipilä, J., and Vartiainen, A., *HSC Chemistry v7.14 software*, 2011.

[16] Prieto, G., Zečević, J., Friedrich, H., de Jong, K., and de Jongh, P., *Towards stable catalysts by controlling collective properties of supported metal nanoparticles*, Nat. Mater., 12(1), 34–39, 2013, URL: *http://www.ncbi.nlm.nih.gov/pubmed/23142841*.

[17] Agny, R. M., and Takoudis, C. G., *Synthesis of methanol from carbon monoxide and hydrogen over a copper-zinc oxide-alumina catalyst*, Ind. Eng. Chem. Prod. Res. Dev., 24(1), 50–55, 1985, URL: *http://pubs.acs.org/doi/abs/10.1021/i300017a010*.

[18] Höppener, R. H., Doesburg, E. B. M., and Scholten, J. J. F., *Preparation and characterization of stable copper/zinc oxide/alumina catalysts for methanol systhesis*, Appl. Catal., 25(C), 109–119, 1986, URL: *https://www.researchgate.net/publication/250690413_Preparation_and_Characterization_of_CopperZinc_OxideAlumina_Catalysts_for_Methanol_Synthesis*.

[19] Baltes, C., Vukojević, S., and Schüth, F., *Correlations between synthesis, precursor, and catalyst structure and activity of a large set of CuO/ZnO/Al_2O_3 catalysts for methanol synthesis*, J. Catal., 258(2), 334–344, 2008, URL: *http://linkinghub.elsevier.com/retrieve/pii/S0021951708002662*.

[20] Saito, M., and Murata, K., *Development of high performance Cu/ZnO-based catalysts for methanol synthesis and the water-gas shift reaction*, Catal. Surv. Asia, 8(4), 285–294, 2004, URL: *http://link.springer.com/10.1007/s10563-004-9119-y*.

[21] Kniep, B., Ressler, T., Rabis, A., Girgsdies, F., Baenitz, M., Steglich, F., and Schlögl, R., *Rational design of nanostructured copper-zinc oxide catalysts for the steam reforming of methanol*, Angew. Chem. Int. Ed., 43(1), 112–15, 2004, URL: *http://www.ncbi.nlm.nih.gov/pubmed/14694487*.

[22] Bems, B., Schur, M., Dassenoy, A., Junkes, H., Herein, D., and Schlögl, R., *Relations between synthesis and microstructural properties of copper/zinc hydroxycarbonates*, Chem. Eur. J., 9(9), 2039–2052, 2003, URL: *http://onlinelibrary.wiley.com/doi/10.1002/chem.200204122/epdf*.

[23] Waugh, K., *Methanol synthesis*, Catal. Today, 15(1), 51–75, 1992, URL: *https://www.researchgate.net/publication/222223565_Methanol_Synthesis*.

[24] Bowker, M., Hadden, R., Houghton, H., Hyland, J., and Waugh, K., *The mechanism of methanol synthesis on copper/zinc oxide/alumina catalysts*, J. Catal., 109(2), 263–273, 1988, URL: *https://www.researchgate.net/publication/244391154_Mechanism_of_methanol_synthesis_on_copperzinc_oxidealumina_catalysts*.

[25] Studt, F., Behrens, M., Kunkes, E. L., Thomas, N., Zander, S., Nørskov, J. K., and Schlögl, R., *The mechanism of CO and CO_2 hydrogenation to methanol over Cu-based catalysts*, ChemCatChem, 7(7), 1105–1111, 2015, URL: *http://onlinelibrary.wiley.com/doi/10.1002/cctc.201500123/abstract*.

[26] Datye, A., Xu, Q., Kharas, K., and McCarty, J., *Particle size distributions in heterogeneous catalysts: What do they tell us about the sintering mechanism?*, Catal. Today, 111(1-2), 59–67, 2006, URL: *http://www.sciencedirect.com/science/article/pii/S092058610500711X*.

[27] Twigg, M., and Spencer, M., *Deactivation of supported copper metal catalysts for hydrogenation reactions*, Appl. Catal. A, 212(1-2), 161–174, 2001, URL: *http://linkinghub.elsevier.com/retrieve/pii/S0926860X00008541*.

[28] Bartholomew, C., *Mechanisms of catalyst deactivation*, Appl. Catal. A, 212(1-2), 17–60, 2001, URL: *http://www.sciencedirect.com/science/article/pii/S0926860X00008437*.

[29] Goeppert, A., Czaun, M., Jones, J.-P., Surya Prakash, G., and Olah, G., *Recycling of carbon dioxide to methanol and derived products - closing the loop*, Chem. Soc. Rev., 43(23), 7995–8048, 2014, URL: *http://www.ncbi.nlm.nih.gov/pubmed/24935751*.

[30] Dolan, G., *Methanol production and markets: Past, present, and future*, in: *The toxicology of methanol*, edited by Clary, J., chapter 1, pp. 1–10, John Wiley & Sons, Inc., Hoboken, New York: U.S.A.2013, 1st edition, ISBN 978-047031759-4.

[31] Quinn, R., Dahl, T., and Toseland, B., *An evaluation of synthesis gas contaminants as methanol synthesis catalyst poisons*, Appl. Catal. A, 272(1-2), 61–68, 2004, URL: *http://linkinghub.elsevier.com/retrieve/pii/S0926860X04004491*.

[32] Pahmy, R., and Mohamed, A., *Utilization of carbon nanotubes as a support material in metal-based catalyst systems: Applications in catalysis*, Recent Pat. Eng., 6(1), 31–47, 2012, URL: *http://www.eurekaselect.com/openurl/content.php?genre=article&issn=1872-2121&volume=6&issue=1&spage=31*.

[33] Pham, H., Anderson, A., Johnson, R., Schmidt-Rohr, K., and Datye, A., *Improved hydrothermal stability of mesoporous oxides for reactions in the aqueous phase*, Angew. Chem. Int. Ed., 51(52), 13163–13167, 2012, URL: *http://www.ncbi.nlm.nih.gov/pubmed/23161647*.

[34] Prieto, G., Meeldijk, J., de Jong, K., and de Jongh, P., *Interplay between pore size and nanoparticle spatial distribution: Consequences for the stability of CuZn/SiO_2 methanol synthesis catalysts*, J. Catal., 303, 31–40, 2013, URL: *http://linkinghub.elsevier.com/retrieve/pii/S002195171300081X*.

[35] Hong, Z.-S., Cao, Y., and Deng, J.-F., *A convenient alcohothermal approach for low temperature synthesis of CuO nanoparticles*, Mater. Lett., 52(1-2), 34–38, 2002, URL: *https://www.researchgate.net/publication/248266306_A_Convenient_Alcohothermal_Approach_for_Low_Temperature_Synthesis_of_CuO_Nanoparticles*.

[36] Zhu, J., Li, D., Chen, H., Yang, X., Lu, L., and Wang, X., *Highly dispersed CuO nanoparticles prepared by a novel quick-precipitation method*, Mater. Lett., 58(26), 3324–3327, 2004, URL: *https://www.researchgate.net/publication/248267433_Highly_Dispersed_CuO_Nanoparticles_Prepared_by_a_Novel_Quick_Precipitation_Method*.

[37] Yin, M., Wu, C.-K., Lou, Y., Burda, C., Koberstein, J., Zhu, Y., and O'Brien, S., *Copper oxide nanocrystals*, J. Am. Chem. Soc., 127(26), 9506–9511, 2005, URL: *http://pubs.acs.org/doi/pdf/10.1021/ja050006u*.

[38] Casavola, M., Hermannsdörfer, J., De Jonge, N., Dugulan, A. I., and De Jong, K. P., *Fabrication of Fischer-Tropsch catalysts by deposition of iron nanocrystals on carbon nanotubes*, Adv. Funct. Mater., 25(33), 5309–5319, 2015, URL: *http://doi.wiley.com/10.1002/adfm.201501882*.

[39] Arrigo, R., Hävecker, M., Wrabetz, S., Blume, R., Lerch, M., McGregor, J., Parrott, E., Zeitler, J., Gladden, L., Knop-Gericke, A., Schlögl, R., and Su, D., *Tuning the acid/base properties of nanocarbons by functionalization via amination*, J. Am. Chem. Soc., 132(28), 9616–9630, 2010, URL: *http://pubs.acs.org.proxy.library.uu.nl/doi/pdf/10.1021/ja910169v*.

[40] Brands, D., Poels, E., and Bliek, A., *Ester hydrogenolysis over promoted Cu/SiO_2 catalysts*, Appl. Catal. A, 184(2), 279–289, 1999, URL: *http://www.sciencedirect.com/science/article/pii/S0926860X99001064*.

[41] Kilo, M., Weigel, J., Wokaun, A., Koeppel, R., Stoeckli, A., and Baiker, A., *Effect of the addition of chromium- and manganese oxides on structural and catalytic properties of copper/zirconia catalysts for the synthesis of methanol from carbon dioxide*, J. Mol. Catal. A: Chem., 126(2-3), 169–184, 1997, URL: *http://www.sciencedirect.com/science/article/pii/S138111699700109X*.

[42] Lachowska, M., and Skrzypek, J., *Methanol synthesis from carbon dioxide and hydrogen over Mn-promoted copper/zinc/zirconia catalysts*, React. Kinet. Catal. Lett., 83(2), 269–273, 2004, URL: *http://link.springer.com/article/10.1023/B:REAC.0000046086.93121.36*.

[43] Słoczyński, J., Grabowski, R., Kozłowska, A., Olszewski, P., Lachowska, M., Skrzypek, J., and Stoch, J., *Effect of Mg and Mn oxide additions on structural and adsorptive properties of $Cu/ZnO/ZrO_2$ catalysts for the methanol synthesis from CO_2*, Appl. Catal. A, 249(1), 129–138, 2003, URL: *http://www.sciencedirect.com/science/article/pii/S0926860X03001911*.

[44] Ma, L., and Wainwright, M., *Development of skeletal copper-chromia catalysts I . Structure and activity promotion of chromia on skeletal copper catalysts for methanol synthesis*, Appl. Catal. A, 187(1), 89–98, 1999, URL: *http://www.ingentaconnect.com/content/els/0926860x/1999/00000187/00000001/art00200*.

[45] Fujitani, T., Saito, M., Kanai, Y., Kakumoto, T., Watanabe, T., Nakamura, J., and Uchijima, T., *The role of metal oxides in promoting a copper catalyst for methanol synthesis*, Catal. Lett., 25(3-4), 271–276, 1994, URL: *http://link.springer.com/article/10.1007/BF00816307*.

[46] Yurieva, T. M., and Minyukova, T. P., *State of copper in Cu-Zn-Al oxide catalysts for methanol synthesis*, React. Kinet. Catal. Lett., 29(1), 55–61, 1985, URL: *http://link.springer.com/article/10.1007/BF02067949*.

[47] Van der Wal, L., *Stability of carbon-supported copper catalysts in the methanol synthesis reaction*, Bachelor thesis, Utrecht University, 2014.

[48] Marceau, E., Carrier, X., and Che, M., *Impregnation and drying*, in: *Synth. Solid Catal.*, edited by de Jong, K., chapter 4, pp. 59–82, Wiley-VCH Verlag GmbH & Co. KGaA, Weinheim, Germany2009, 2nd edition, ISBN 9783527320400.

[49] Perego, C., and Villa, P., *Catalyst preparation methods*, Catal. Today, 34(3-4), 281–305, 1997, URL: *https://www.researchgate.net/publication/236658347_Catalyst_preparation_methods*.

[50] Eggenhuisen, T. M., and De Jongh, P. E., *Supported nanoparticles*, in: *Nanoparticles: Workhorses of Nanoscience*, edited by De Mello Donegá, C., chapter 5, pp. 121–144, Springer-Verlag, Berlin Heidelberg2014, 1st edition, ISBN 978-3-662-44823-6.

[51] Atkins, P., Overton, T., Rourke, J., Weller, M., and Armstrong, F., *Inorganic Chemistry*, Oxford University Press Inc., Oxford2014, 6th edition, ISBN 978-0-19-964182-6.

[52] Munnik, P., Wolters, M., Gabrielsson, A., Pollington, S., Headdock, G., Bitter, J., de Jongh, P., and de Jong, K., *Copper nitrate redispersion to arrive at highly active silica-supported copper catalysts*, J. Phys. Chem. C, 115(30), 14698–14706, 2011, URL: *http://pubs.acs.org/doi/pdf/10.1021/jp111778g*.

[53] Toupance, T., Kermarec, M., and Louis, C., *Metal particle size in silica-supported copper catalysts. Influence of the conditions of preparation and of thermal pretreatments*, J. Phys. Chem. B, 104(5), 965–972, 2000, URL: *http://pubs.acs.org/doi/abs/10.1021/jp993399q*.

[54] Haynes, W., *CRC Handbook of Chemistry & Physics Online, 95th Edition*, 2014, URL: *http://www.hbcponline.com/*.

[55] Sing, K., *The use of nitrogen adsorption for the characterisation of porous materials*, Colloids Surf. A, 187-188, 3–9, 2001, URL: *http://www.sciencedirect.com/science/article/pii/S0927775701006124*.

[56] De Jongh, P. E., and Eggenhuisen, T. M., *Nanoporous materials and confined liquids*, in: *Nanoparticles: Workhorses of Nanoscience*, edited by De Mello Donegá, C., chapter 4, pp. 99–120, Springer-Verlag, Berlin Heidelberg2014, 1st edition, ISBN 978-3-662-44822-9.

[57] Goertzen, S., Thériault, K., Oickle, A., Tarasuk, A., and Andreas, H., *Standardization of the Boehm titration. Part I. CO_2 expulsion and endpoint determination*, Carbon, 48(4), 1252–1261, 2010, URL: *http://www.sciencedirect.com/science/article/pii/S0008622309007854*.

[58] Rawle, A., *Basic principles of particle size analysis*, Surf. Coat. Int., 86(2), 58–65, 2003.

[59] Patterson, A. L., *The Scherrer formula for X-ray particle size determination*, Phys. Rev., 56(10), 978–982, 1939, URL: *http://link.aps.org/doi/10.1103/PhysRev.56.978*.

[60] Scherrer, P., *Bestimmung der Grösse und der inneren Struktur von Kolloidteilchen mittels Röntgenstrahlen*, Göttinger Nachrichten, 2, 98–100, 1918, URL: *http://link.springer.com/chapter/10.1007/978-3-662-33915-2_7*.

[61] Fierro, G., Lo Jacono, M., Inversi, M., Porta, P., Cioci, F., and Lavecchia, R., *Study of the reducibility of copper in CuO-ZnO catalysts by temperature-programmed reduction*, Appl. Catal. A, 137(2), 327–348, 1996, URL: *http://www.sciencedirect.com/science/article/pii/0926860X95003118*.

[62] Stobbe, E. R., de Boer, B. A., and Geus, J. W., *The reduction and oxidation behaviour of manganese oxides*, Catal. Today, 47(1-4), 161–167, 1999, URL: *https://www.researchgate.net/publication/223223391_The_Reduction_and_Oxidation_Behavior_of_Manganese_Oxides*.

[63] Wang, S., Murata, K., Hayakawa, T., Hamakawa, S., and Suzuki, K., *Dehydrogenation of ethane with carbon dioxide over supported chromium oxide catalysts*, Appl. Catal. A, 196(1), 1–8, 2000, URL: *http://www.ingentaconnect.com/content/els/0926860x/2000/00000196/00000001/art00450*.

[64] Al-Zahrani, S. M., Jibril, B. Y., and Abasaeed, A. E., *Selection of optimum chromium oxide-based catalysts for propane oxidehydrogenation*, Catal. Today, 81(3), 507–516, 2003, URL: *http://www.sciencedirect.com/science/article/pii/S0920586103001494*.

[65] NIST, *Mass spectrometry data center*, URL: *http://chemdata.nist.gov/*.

[66] Van den Berg, R., Parmentier, T. E., Elkjær, C. F., Gommes, C. J., Sehested, J., Helveg, S., De Jongh, P. E., and De Jong, K. P., *Support functionalization to retard Ostwald ripening in copper methanol synthesis catalysts*, ACS Catal., 5(7), 4439–4448, 2015, URL: *http://pubs.acs.org/doi/abs/10.1021/acscatal.5b00833*.

[67] Groen, J., Peffer, L., and Pérez-Ramírez, J., *Pore size determination in modified micro- and mesoporous materials. Pitfalls and limitations in gas adsorption data analysis*, Microporous Mesoporous Mater., 60(1-3), 1–17, 2003, URL: *http://www.sciencedirect.com/science/article/pii/S1387181103003391*.

[68] Busca, G., *Other solid acid and basic catalytic materials*, in: *Heterogeneous Catalytic Materials: Solid State Chemistry, Surface Chemistry and Catalytic Behavior*, chapter 8, pp. 278–280, Elsevier B.V., Amsterdam, The Netherlands2014, 1st edition, ISBN 978-0-444-59524-9.

[69] Shannon, R., *Revised effective ionic radii and systematic studies of interatomic distances in halides and chalcogenides*, Acta Crystallogr. Sect. A, A32(5), 751–767, 1976, URL: *http://journals.iucr.org/a/issues/1976/05/00/a12967/a12967.pdf*.

[70] Gilson, R., and Durrant, M., *Estimation of the pKa values of water ligands in transition metal complexes using density functional theory with polarized continuum model solvent corrections*, Dalton Trans., (46), 10223–10230, 2009, URL: *http://pubs.rsc.org/en/content/articlepdf/2009/dt/b911593e*.

[71] Gu, L., and Jin, C., *Copper-catalyzed aerobic oxidative cleavage of C–C bonds in epoxides leading to aryl nitriles and aryl aldehydes*, Chem. Commun., 51(30), 6572–6575, 2015, URL: *http://xlink.rsc.org/?DOI=C5CC00360A*.

[72] Martínez, N., Venturini, R., Soé Silva, H., González, J., and Rodríguez, A., *Copper on activated carbon for catalytic wet air oxidation*, Mater. Res., 12(1), 45–50, 2009, URL: *http://www.scielo.br/scielo.php?pid=S1516-14392009000100004&script=sci_arttext*.

[73] Valkaj, K., Katovic, A., Tomašic, V., and Zrncevic, S., *Characterization and activity of Cu/ZSM5 catalysts for the oxidation of phenol with hydrogen peroxide*, Chem. Eng. Technol., 31(3), 398–403, 2008, URL: *http://doi.wiley.com/10.1002/ceat.200700354*.

[74] Farahani, B., Rajabi, F., Bahmani, M., Ghelichkhani, M., and Sahebdelfar, S., *Influence of precipitation conditions on precursor particle size distribution and activity of Cu/ZnO methanol synthesis catalyst*, Appl. Catal. A, 482, 237–244, 2014, URL: *http://linkinghub.elsevier.com/retrieve/pii/S0926860X14003688*.

[75] Tavasoli, A., Trépanier, M., Dalai, A., and Abatzoglou, N., *Effects of confinement in carbon nanotubes on the activity, selectivity, and lifetime of Fischer-Tropsch Co/Carbon nanotube catalysts*, J. Chem. Eng. Data, 55(8), 2757–2763, 2010, URL: *http://pubs.acs.org/doi/pdf/10.1021/je900984c*.

[76] Chen, W., Fan, Z., Pan, X., and Bao, X., *Effect of confinement in carbon nanotubes on the activity of Fischer-Tropsch iron catalyst*, J. Am. Chem. Soc., 130(29), 9414–9419, 2008, URL: *http://pubs.acs.org/doi/pdf/10.1021/ja8008192*.

[77] Pan, X., Fan, Z., Chen, W., Ding, Y., Luo, H., and Bao, X., *Enhanced ethanol production inside carbon-nanotube reactors containing catalytic particles*, Nat. Mater., 6(7), 507–511, 2007, URL: *http://www.nature.com/nmat/journal/v6/n7/pdf/nmat1916.pdf*.

[78] Figueiredo, J. L., *Functionalization of porous carbons for catalytic applications*, J. Mater. Chem. A, 1(33), 9351–9364, 2013, URL: *http://xlink.rsc.org/?DOI=c3ta10876g*.

[79] Behrens, M., Studt, F., Kasatkin, I., Kühl, S., Hävecker, M., Abild-Pedersen, F., Zander, S., Girgsdies, F., Kurr, P., Kniep, B.-L., Tovar, M., Fischer, R., Nørskov, J., and Schlögl, R., *The active site of methanol synthesis over $Cu/ZnO/Al_2O_3$ industrial catalysts*, Science, 336(6083), 893–897, 2012, URL: *http://www.ncbi.nlm.nih.gov/pubmed/22517324*.

[80] Khodakov, A., Chu, W., and Fongarland, P., *Advances in the development of novel cobalt Fischer-Tropsch catalysts for synthesis of long-chain hydrocarbons and clean fuels*, Chem. Rev., 107(5), 1692–1744, 2007, URL: *http://pubs.acs.org/doi/pdf/10.1021/cr050972v*.

[81] Bezemer, G., Radstake, P., Falke, U., Oosterbeek, H., Kuipers, H., van Dillen, A., and de Jong, K., *Investigation of promoter effects of manganese oxide on carbon nanofiber-supported cobalt catalysts for Fischer-Tropsch synthesis*, J. Catal., 237(1), 152–161, 2006, URL: *http://www.sciencedirect.com/science/article/pii/S0021951705004203*.

[82] Thiessen, J., Rose, A., Meyer, J., Jess, A., and Curulla-Ferré, D., *Effects of manganese and reduction promoters on carbon nanotube supported cobalt catalysts in Fischer–Tropsch synthesis*, Microporous Mesoporous Mater., 164, 199–206, 2012, URL: *http://linkinghub.elsevier.com/retrieve/pii/S1387181112003137*.

[83] Cervantes, C., Campos-García, J., Devars, S., Gutiérrez-Corona, F., Loza-Tavera, H., Torres-Guzmán, J. C., and Moreno-Sánchez, R., *Interactions of chromium with microorganisms and plants*, FEMS Microbiol. Rev., 25(3), 335–347, 2001, URL: *http://www.ncbi.nlm.nih.gov/pubmed/11348688*.

[84] Zayed, A. M., and Terry, N., *Chromium in the environment: Factors affecting biological remediation*, Plant Soil, 249(1), 139–156, 2003, URL: *http://link.springer.com/article/10.1023/A:1022504826342*.

Appendices

A Nitrogen Physisorption Isotherms

In this appendix the nitrogen physisorption isotherms of the bare supports, CNTs, oxCNTs, and HSAG, are displayed in figure A.1a, c, and e, respectively. The corresponding BJH curves are depicted in figure A.1b, d, and f, respectively. In section 3.1.2.1 the nitrogen physisorption experiments for the bare supports are discussed.

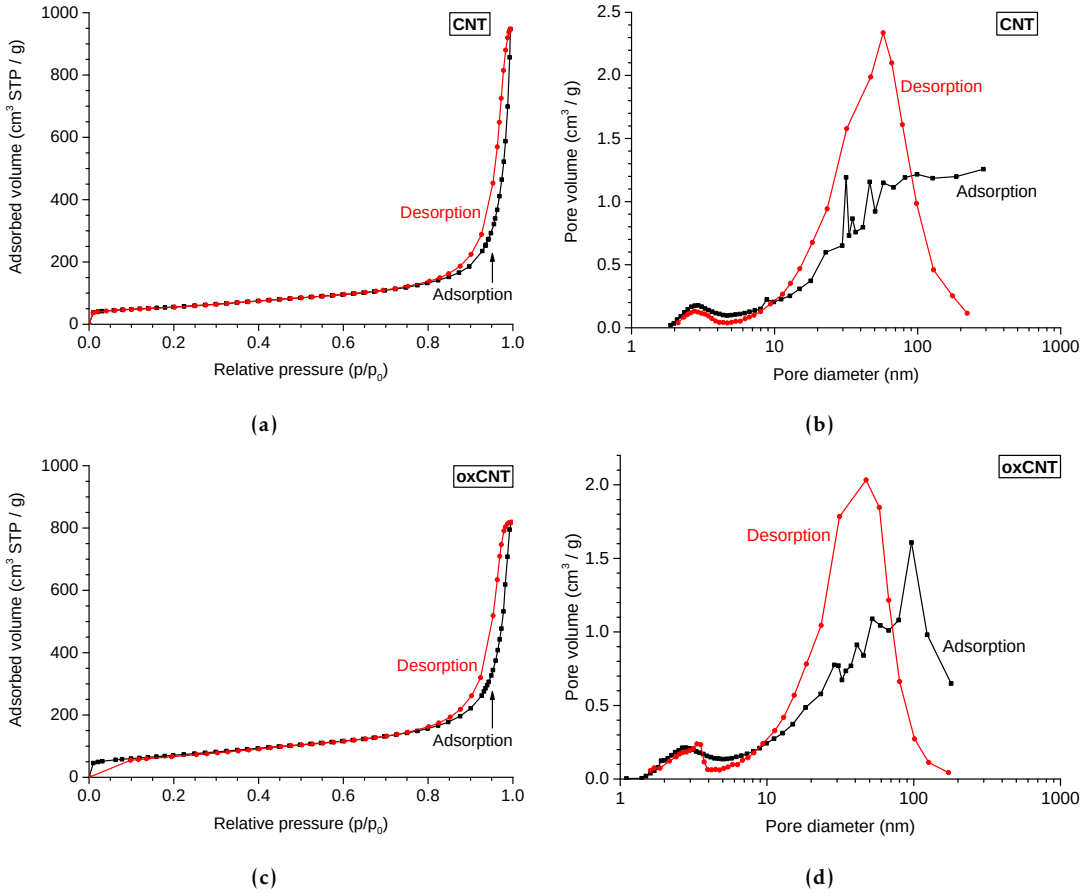

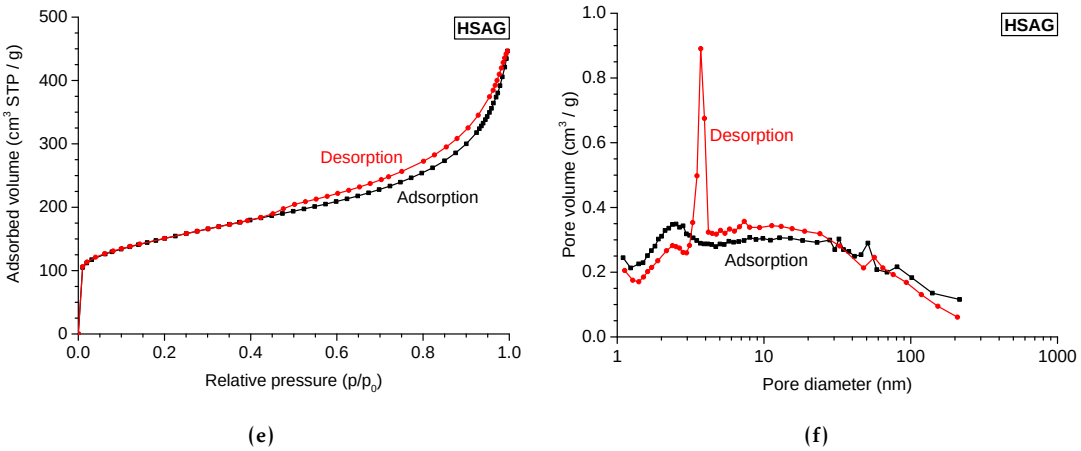

Figure A.1 N_2 physisorption isotherms at 77 K, containing both the adsorption and desorption branches, of the **a** CNT, **c** oxCNT, and **e** HSAG supports. Corresponding BJH plots are respectively depicted at **b**, **d**, and **f**.

B X-Ray Diffractogram Comparison

The MnO-Cu/HSAG catalyst was synthesized twice to investigate if the larger copper nanoparticles in the catalyst could be reproduced. The secondly synthesized catalyst was characterized by X-ray diffraction (XRD) to investigate the reproducibility. The results of this diffractogram comparison are given in figure B.1. Qualitatively, only small differences between the diffractograms of the MnO-Cu/HSAG catalysts could be observed. The copper crystallite size could however not be calculated, due to overlapping peaks.

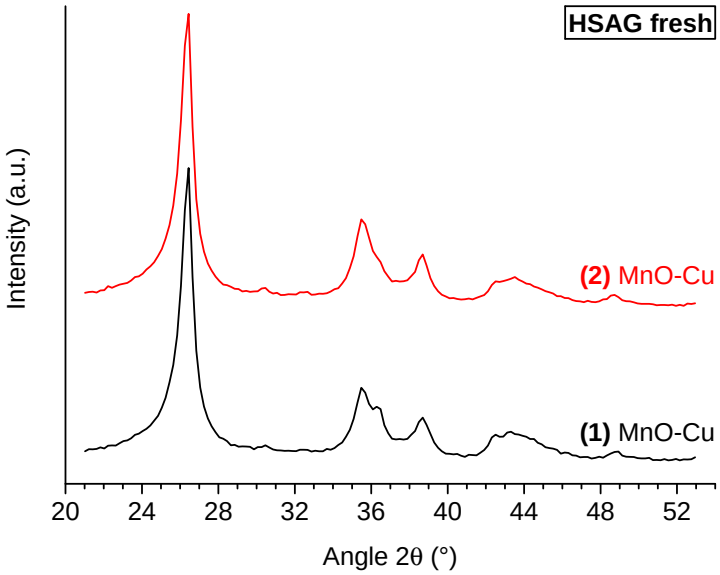

Figure B.1 Comparison of XRD diffratograms of as-synthesized, reproduced MnO-Cu/HSAG catalysts. Qualitatively, only small differences could be observed between the two diffractograms. For example, the shoulder at 36.5° due to a Cu_2O crystallite was relatively smaller for the reproduced than the for the original catalyst, indicating smaller particles were obtained for the reproduced catalyst to some extent. No copper crystallite size could be obtained by the Scherrer equation. The (1) MnO-Cu/HSAG catalyst was further used in this thesis.

C Selectivity, Conversion, and Activity Curves During Catalysis

From the data obtained with the thermal conductivity detector (TCD) equipped onto the downstream, online gas chromatograph (GC) during catalysis information about different parameters could be obtained, calculated from the equations presented in section 2.3.1. In figures C.1 and C.2 the product selectivity curves of the oxCNT-supported and HSAG-supported catalysts were given, respectively. Furthermore, in figures C.3, C.4, and C.5 the, respectively, copper time yield (CTY), total CO and CO_2 conversion, and catalyst mass-based methanol activity comparisons between the oxCNT-supported and HSAG-supported catalysts are depicted. In section 3.3 this data is discussed.

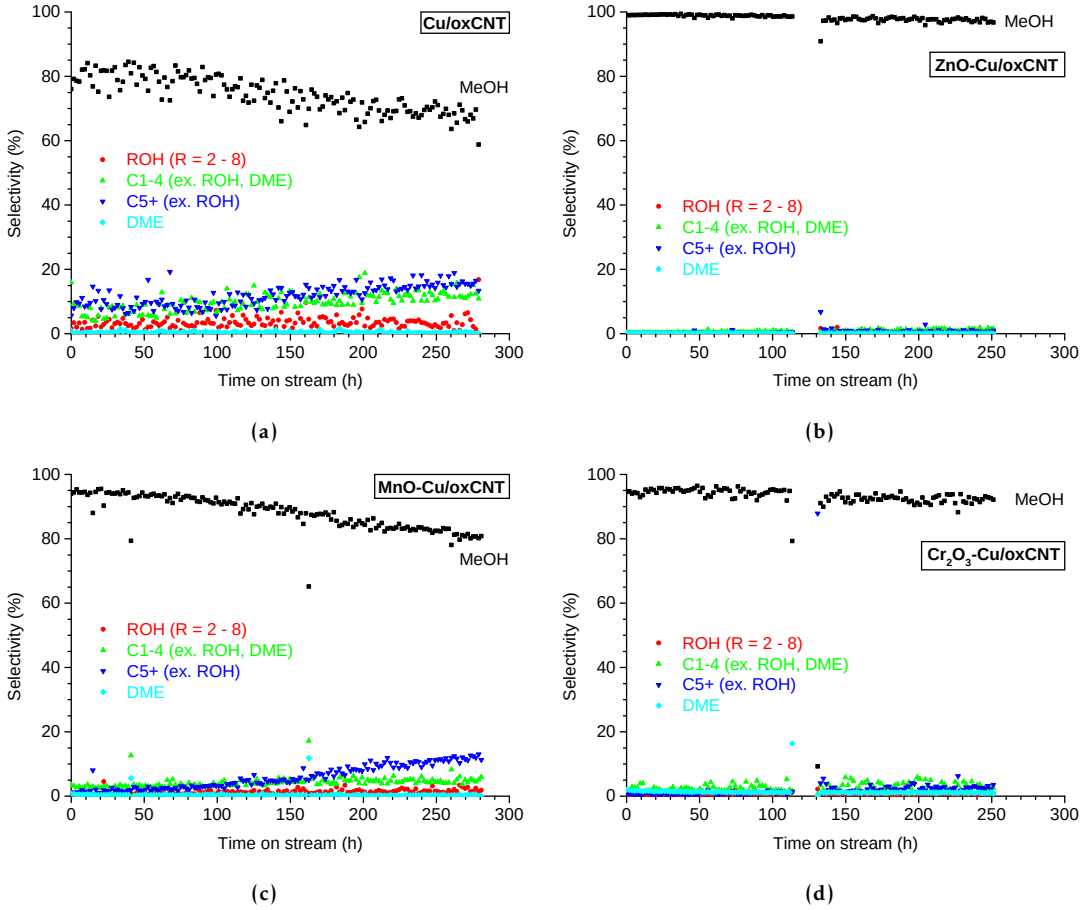

Figure C.1 Product selectivity curves of the oxCNT-supported catalysts. Figures **b** and **d** showed no change in methanol selectivity. Figure **c** showed an increase in Fischer-Tropsch-like products (C5+ fraction) after 80 h of catalysis. Figure **a** showed a relatively low and scattered selectivity towards methanol, induced by prior particle growth and low CO and CO_2 conversion levels.

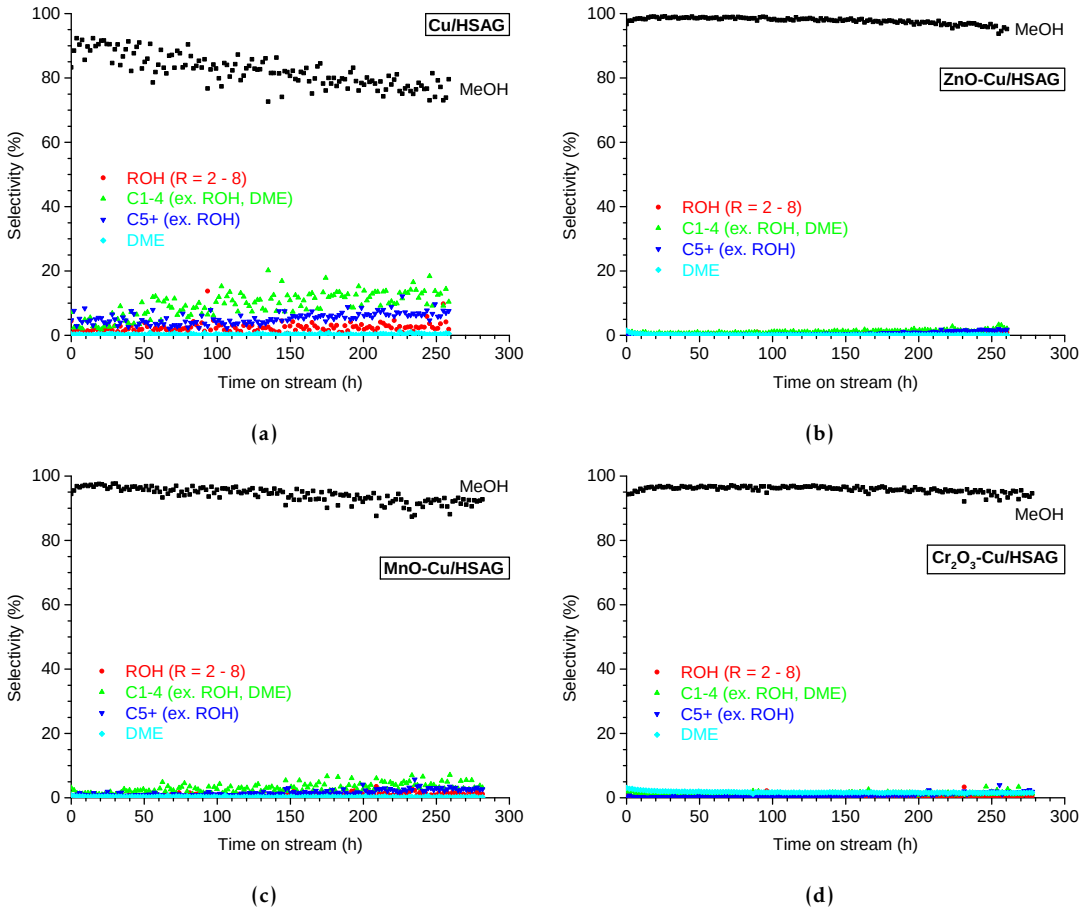

Figure C.2 Product selectivity curves of the HSAG-supported catalysts. Figures **b**-**d** showed a stable and considerably selective production of methanol. Figure **a** showed a relatively low and scattered selectivity towards methanol, induced by prior particle growth and low CO and CO_2 conversion levels.

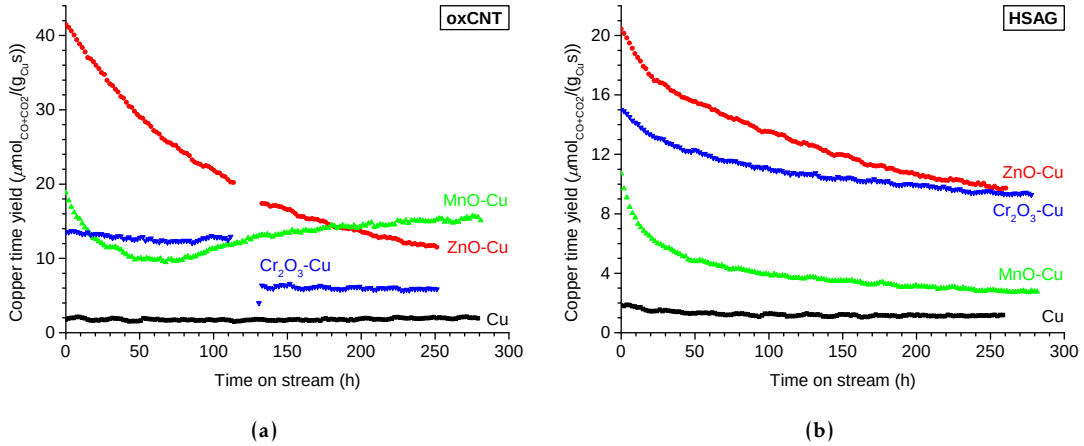

Figure C.3 Copper time yields (CTY) of the **a** oxCNT-supported and **b** HSAG-supported catalysts. Figure **a** showed an increase in activity after 80 h, corresponding to the synthesis of Fischer-Tropsch-like products, indicated by figure C.1c. Figure **a** showed a sudden drop in CTY after GC malfunction, observed from ZnO-Cu/oxCNT and Cr_2O_3-Cu/oxCNT. Figure **b** showed decreasing CTY values for the HSAG-supported catalysts. For both supports the unpromoted catalyst had a considerably low CTY.

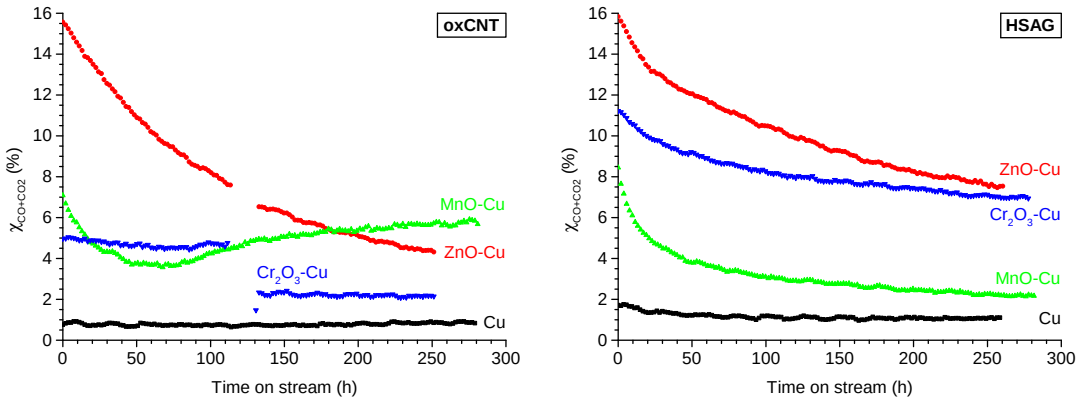

Figure C.4 Total CO and CO_2 conversions (χ_{CO+CO_2}) of the **a** oxCNT-supported and **b** HSAG-supported catalysts. Figure **a** showed an increase in χ_{CO+CO_2} after 80 h, corresponding to the synthesis of Fischer-Tropsch-like products, indicated by figure C.1c. Figure **a** showed a sudden drop in conversion after GC malfunction, observed from ZnO-Cu/oxCNT and Cr_2O_3-Cu/oxCNT. Figure **b** showed decreasing χ_{CO+CO_2} values for the HSAG-supported catalysts. For both supports the unpromoted catalyst had a considerably low χ_{CO+CO_2}.

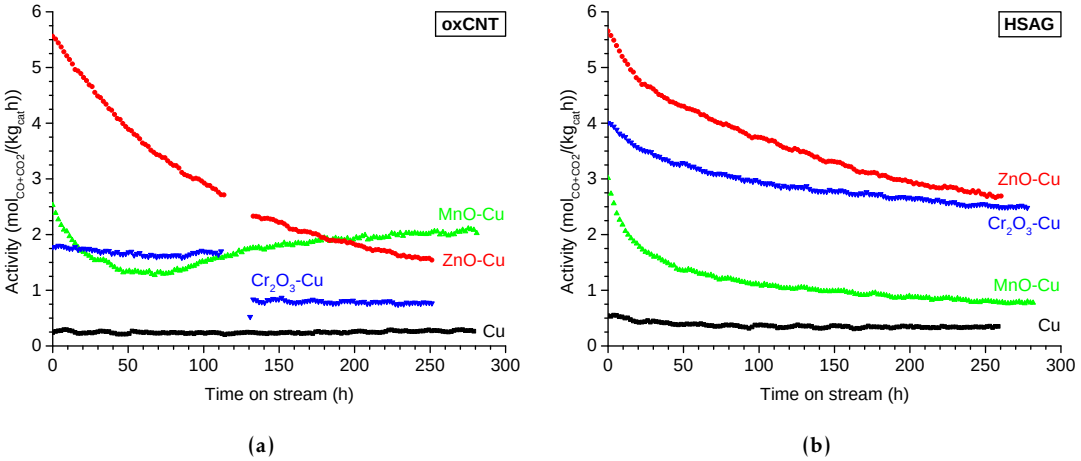

Figure C.5 Catalyst mass-based activity curves towards methanol (χ_{CO+CO_2}) of the **a** oxCNT-supported and **b** HSAG-supported catalysts. Figure **a** showed an increase in z_{CO+CO_2} after 80 h, corresponding to the synthesis of Fischer-Tropsch-like products, indicated by figure C.1c. Figure **a** showed a sudden drop in conversion after GC malfunction, observed from ZnO-Cu/oxCNT and Cr_2O_3-Cu/oxCNT. Figure **b** showed decreasing z_{CO+CO_2} values for the HSAG-supported catalysts. For both supports the unpromoted catalyst had a considerably low z_{CO+CO_2}.

D Transmission Electron Microscopy Images

In this appendix one or two representative transmission electron microscopy (TEM) images of each catalyst are displayed. In figure D.1 TEM images of the as-synthesized, CNT-supported catalysts are displayed, whereas in figures D.2 and D.3 comparisons between the TEM images of the as-synthesized and the corresponding spent catalysts are given of the oxCNT-supported and HSAG-supported catalysts, respectively. In sections 3.2.2.3 and 3.3.3.1 the as-synthesized and spent TEM images are discussed, respectively.

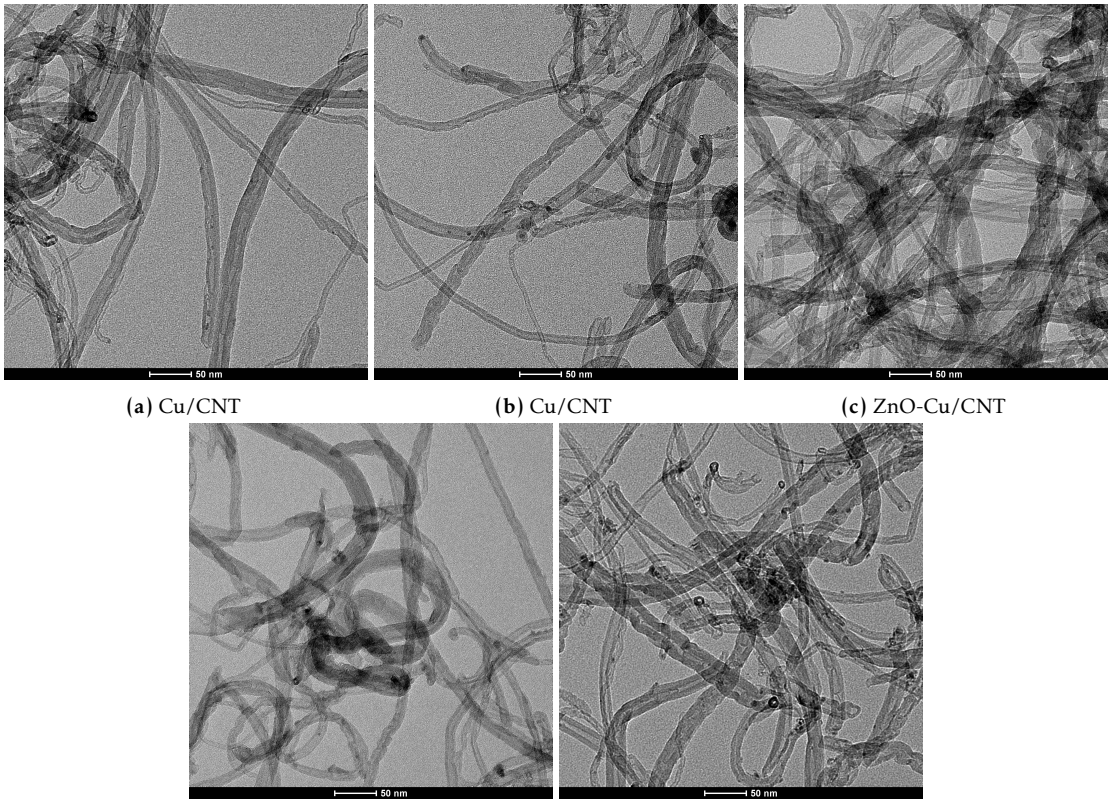

(a) Cu/CNT **(b)** Cu/CNT **(c)** ZnO-Cu/CNT

(d) MnO-Cu/CNT **(e)** Cr_2O_3-Cu/CNT

Figure D.1 TEM images of as-synthesized CNT-supported catalysts.

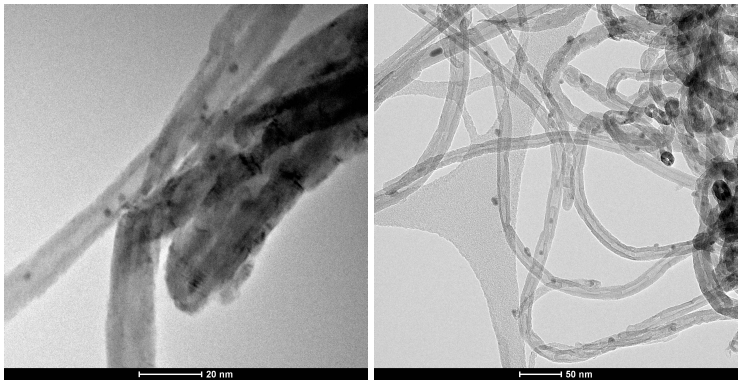

(a) Cu/oxCNT fresh **(b)** Cu/oxCNT spent

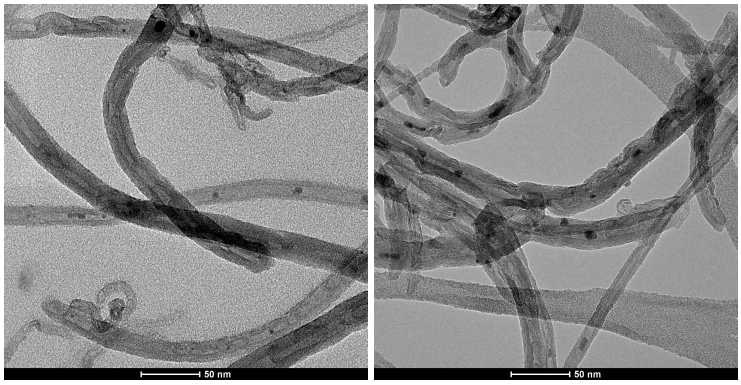

(c) ZnO-Cu/oxCNT fresh **(d)** ZnO-Cu/oxCNT spent

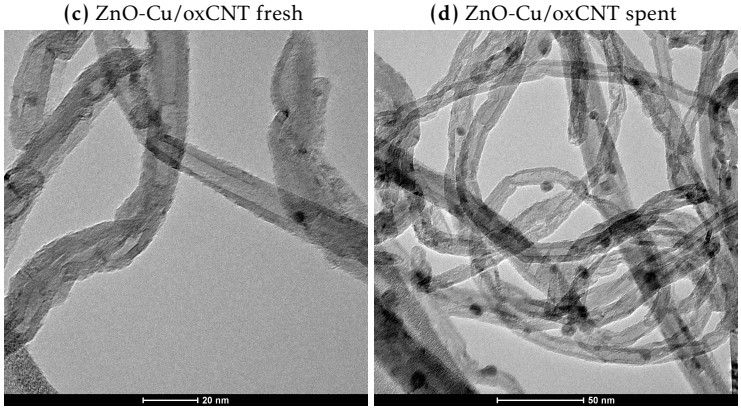

(e) MnO-Cu/oxCNT fresh **(f)** MnO-Cu/oxCNT spent

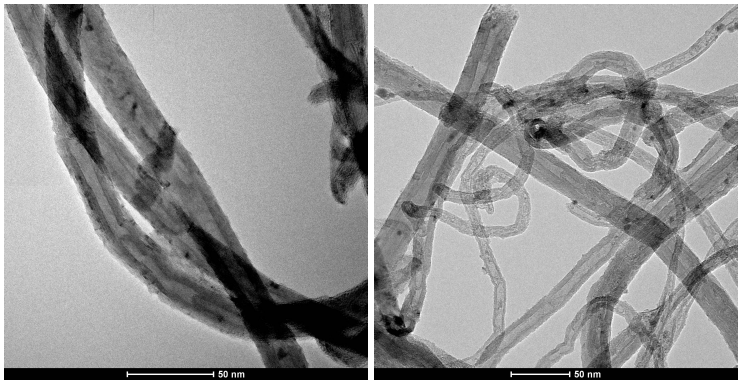

(g) Cr_2O_3-Cu/oxCNT fresh **(h)** Cr_2O_3-Cu/oxCNT spent

Figure D.2 TEM images of as-synthesized or fresh and spent oxCNT-supported catalysts.

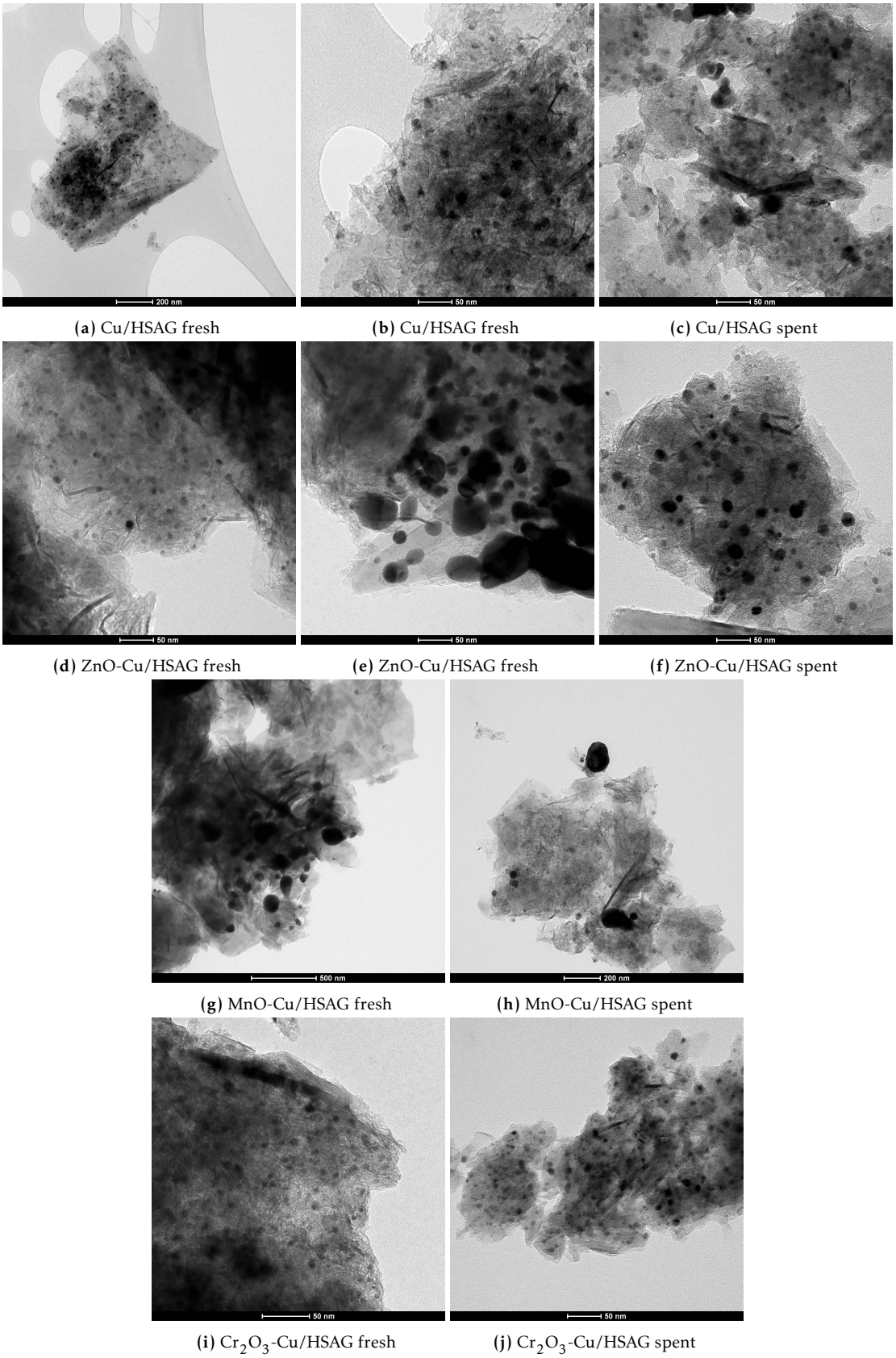

(a) Cu/HSAG fresh **(b)** Cu/HSAG fresh **(c)** Cu/HSAG spent

(d) ZnO-Cu/HSAG fresh **(e)** ZnO-Cu/HSAG fresh **(f)** ZnO-Cu/HSAG spent

(g) MnO-Cu/HSAG fresh **(h)** MnO-Cu/HSAG spent

(i) Cr_2O_3-Cu/HSAG fresh **(j)** Cr_2O_3-Cu/HSAG spent

Figure D.3 TEM images of as-synthesized or fresh and spent HSAG-supported catalysts.

E Particle Size Histograms

From transmission electron microscopy (TEM) a particle size distribution per catalyst could be obtained. These distributions were depicted in histograms, with accompanying number-averaged copper particle diameter d_N. In figure E.1 the histograms of the as-synthesized, CNT-supported catalysts are given, whereas in figures E.2 and E.3 comparisons between the histograms of the as-synthesized and the corresponding spent catalysts are given of the oxCNT-supported and HSAG-supported catalysts, respectively. In sections 3.2.2.3 and 3.3.3.1 the as-synthesized and spent TEM images are discussed, respectively.

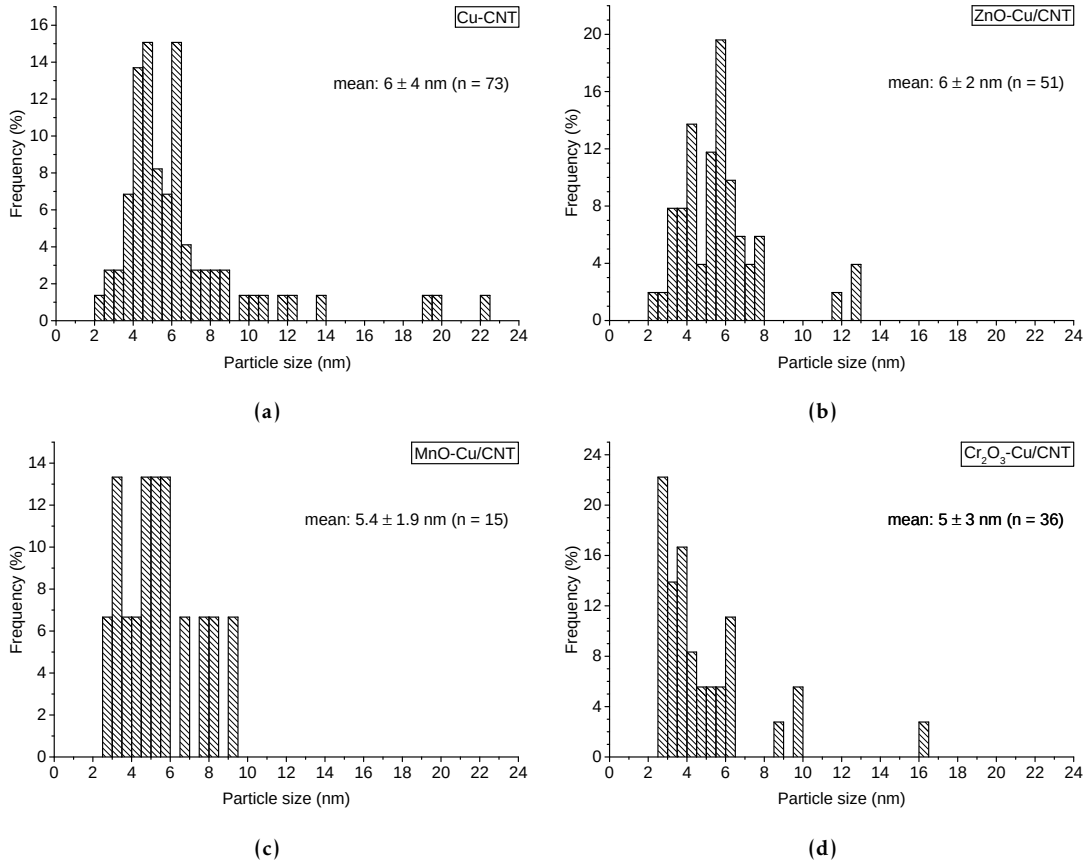

Figure E.1 Histograms for the as-synthesized or fresh, CNT-supported catalysts. In the histograms the number-averaged particle size with the corresponding standard deviation and number of counted particles was given.

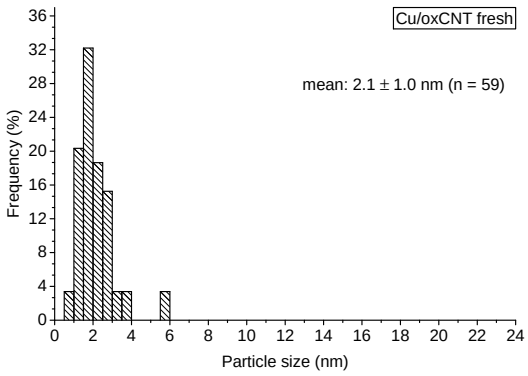
Cu/oxCNT fresh
mean: 2.1 ± 1.0 nm (n = 59)
Frequency (%)
Particle size (nm)

(a)

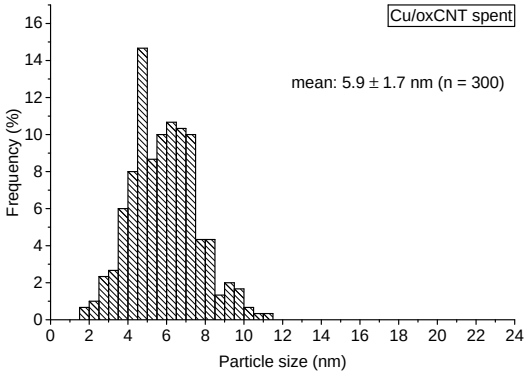
Cu/oxCNT spent
mean: 5.9 ± 1.7 nm (n = 300)
Frequency (%)
Particle size (nm)

(b)

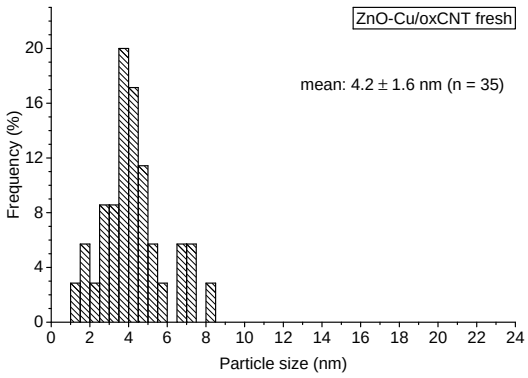
ZnO-Cu/oxCNT fresh
mean: 4.2 ± 1.6 nm (n = 35)
Frequency (%)
Particle size (nm)

(c)

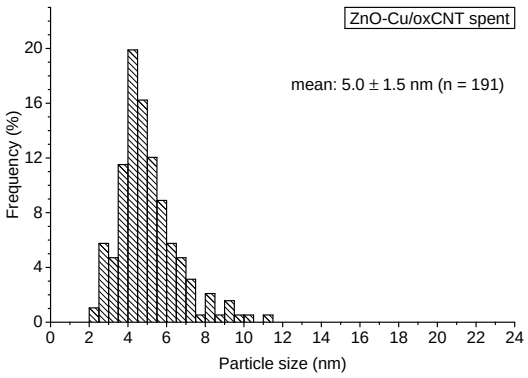
ZnO-Cu/oxCNT spent
mean: 5.0 ± 1.5 nm (n = 191)
Frequency (%)
Particle size (nm)

(d)

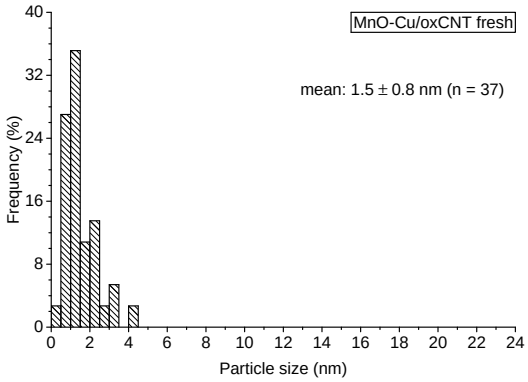
MnO-Cu/oxCNT fresh
mean: 1.5 ± 0.8 nm (n = 37)
Frequency (%)
Particle size (nm)

(e)

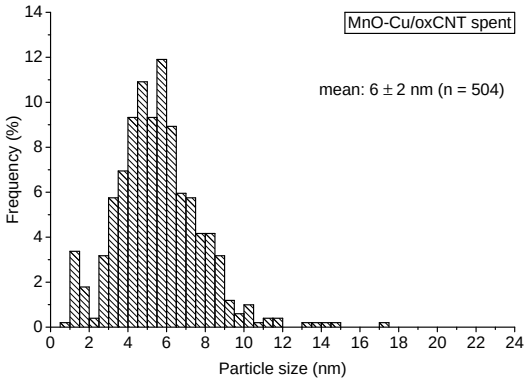
MnO-Cu/oxCNT spent
mean: 6 ± 2 nm (n = 504)
Frequency (%)
Particle size (nm)

(f)

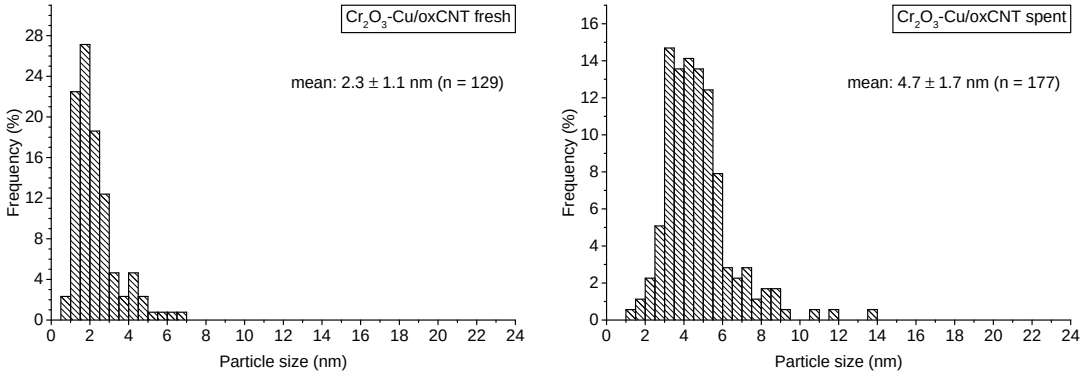

(g) **(h)**

Figure E.2 Histograms for the (**a**, **c**, **e**, **g**) as-synthesized or fresh and (**b**, **d**, **f**, **h**) corresponding spent, oxCNT-supported catalysts. In the histograms the number-averaged particle size with the corresponding standard deviation and number of counted particles was given.

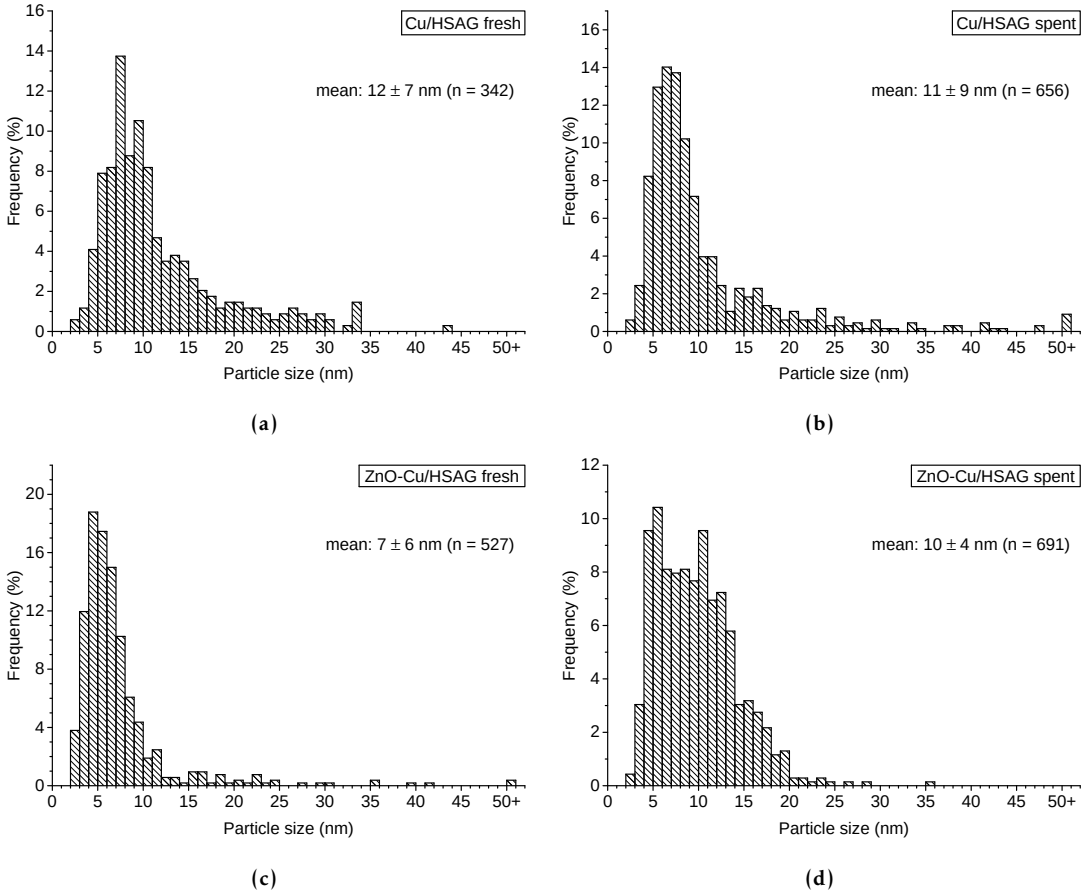

(a) **(b)**

(c) **(d)**

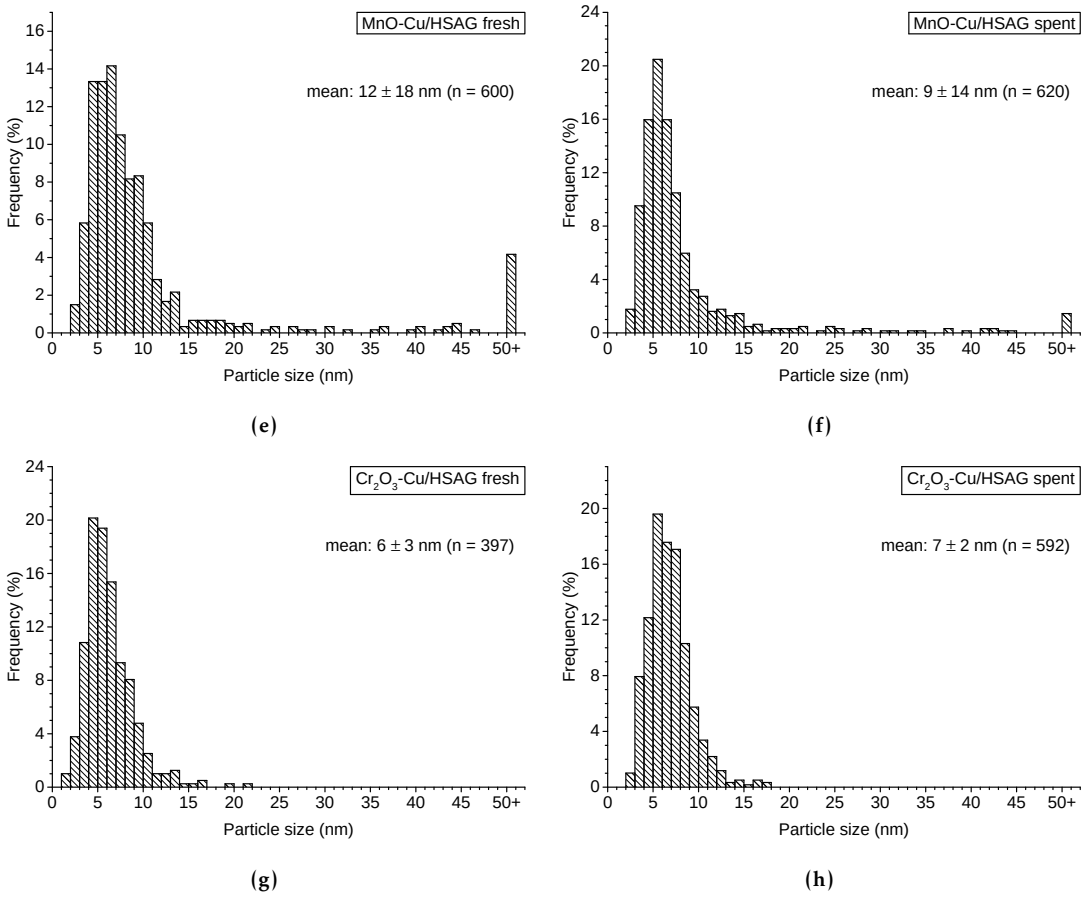

Figure E.3 Histograms for the (**a**, **c**, **e**, **g**) as-synthesized or fresh and (**b**, **d**, **f**, **h**) corresponding spent, HSAG-supported catalysts. In the histograms the number-averaged particle size with the corresponding standard deviation and number of counted particles was given.

F Copper Particle Size Comparisons

With transmission electron microscopy (TEM) the copper particle sizes of the as-synthesized and spent catalysts were calculated. Table F.1 shows the calculated number-averaged d_N, surface-averaged d_S, and volume-averaged d_V particle sizes with accompanying standard deviations. The calculations of these averaged particle sizes are described in section 2.2.3. From table F.1 is was apparent that the copper particles grew more significantly when supported on oxCNTs than on HSAG, probably induced by their smaller, initial particle sizes. The relative uncertainties for the HSAG-supported catalysts were considerably larger compared to their oxCNT-supported counterparts.

Table F.1 Mean copper particle sizes obtained from TEM. d_N, d_S, and d_V are number-averaged, surface-averaged, and volume-averaged particle size, respectively. From this table is was apparent that the general effect of carbon support on the copper particle size of the as-synthesized or fresh catalysts was as following: HSAG > CNT > oxCNT. Addition of promoters did not have any significant effect on the average copper particle size deposited on the tube-like supports. For HSAG-supported catalysts manganese promotion significantly increased the average copper particle size, whereas chromium promotion decreased this size. The copper particles grew more significantly after catalysis when supported on oxCNTs than on HSAG. The relative uncertainties for the HSAG-supported catalysts were considerably larger compared to their oxCNT-supported counterparts.

catalyst		**for fresh catalysts**						**for spent catalysts**					
support	metal	d_N (nm)		d_S (nm)		d_V (nm)		d_N (nm)		d_S (nm)		d_V (nm)	
CNT	Cu	6	± 4	7	± 4	9	± 5						
	ZnO-Cu	6	± 2	6	± 2	7	± 3						
	MnO-Cu	5.4	± 1.9	6	± 2	6	± 2						
	Cr_2O_3-Cu	5	± 3	6	± 3	6	± 4						
oxCNT	Cu	2.1	± 1.0	2.3	± 1.0	2.6	± 1.2	5.9	± 1.7	6.1	± 1.8	6.3	± 1.9
	ZnO-Cu	4.2	± 1.6	4.5	± 1.7	4.8	± 1.8	5.0	± 1.5	5.2	± 1.6	5.5	± 1.7
	MnO-Cu	1.5	± 0.8	1.7	± 1.0	1.9	± 1.1	6	± 2	6	± 2	6	± 3
	Cr_2O_3-Cu	2.3	± 1.1	2.5	± 1.2	2.8	± 1.4	4.7	± 1.7	5.0	± 1.8	5	± 2
HSAG	Cu	12	± 7	13	± 8	15	± 9	11	± 9	14	± 11	18	± 14
	ZnO-Cu	7	± 6	9	± 7	12	± 10	10	± 4	11	± 5	12	± 5
	MnO-Cu	12	± 18	21	± 31	34	± 50	9	± 14	17	± 25	30	± 45
	Cr_2O_3-Cu	6	± 3	7	± 3	7	± 3	7	± 2	7	± 3	8	± 3

G Response Factors

In this appendix the response factors (RFs) of the tracked linear alkanes and alcohols during catalysis for the flame ionization detector (FID) are presented in table G.1. These RFs were needed to calculate product selectivities, as described in section 2.3.1. In appendix C the resulting product selectivity plots are depicted.

Table G.1 Response factors (RFs) of linear alkanes and alcohols and dimethyl ether for the flame ionization detector (FID). **a** Dimethyl ether.

carbon number	**response factor**		
	n-alkane	*n*-alcohol	DME[a]
C1	0.98	0.32	0.37
C2	0.97	0.48	
C3	0.98	0.61	
C4	1.09	0.69	
C5	1.04	0.78	
C6	1.03	0.81	
C7	1.00	0.84	
C8	0.97	1.00	
C9	0.98		
C10-C16	1.00		